universität wien

DISSERTATION

Titel der Disseration

Numerical simulation of double-diffusive convection

Verfasser
Mag. rer. nat. Florian Zaussinger

angestrebter akademischer Grad
Doktor der Naturwissenschaften (Dr. rer. nat.)

Pressbaum, am 6. Dezember 2010

Studienkennzahl lt. Studienblatt: A 091 405
Dissertationsgebiet lt. Studienblatt: Mathematik
Betreuer: Univ. Prof. Dr. Herbert J. Muthsam

Abstract

Semi-convective mixing, as an example of double-diffusive convection, is of general importance in multi-component fluid mixing processes. In astrophysics it occurs when the mean molecular weight gradient caused by a mixture of light material on top of heavier one counteracts the convective instability caused by a temperature gradient. Direct numerical simulations of double-diffusive fluid flows in a realistic stellar parameter space are currently not feasible. Hence, a model describing compressible and incompressible semi-convection was developed, which allows to extrapolate in terms of a power law into this parameter range. Previous theoretical work has disagreed on the presence or absence of layer formation. To investigate properties of pre-assigned layers high resolution numerical simulations of such multi-layers have been performed for the 2D case. The simulation code has been parallelised with MPI© and OpenMP© to gain maximal performance. This thesis covers two topics. The first part presents the modelling of double-diffusive flows and introduces how to compare compressible and incompressible fluids in a mathematical and physical way. The compressible binary mixture equations have been solved with a weighted essentially non-oscillatory (WENO) scheme of 5th order. The inviscid parts of this set of equations are solved along characteristics in the eigensystem, which guarantees physically correct solutions. The incompressible set of equations is solved on an appropriate staggered grid. Especially the combination of this staggered grid with the WENO scheme is new and provides high numerical stability. The second part gives results for various double-diffusive experiments and compares them with theoretical considerations. A detailed parameter study with varying Prandtl-, Lewis-, Rayleigh-number and stability parameter R_ρ has been done. Theoretical estimations for the thermal- and mass fluxes through semi-convective layers could be validated and extended. Even single semi-convective layers can be stabilised under realistic conditions in a multi-layer environment. An extension in terms of a power law to a parameter regime relevant to stellar astrophysics has been done. Based on this power law it could be shown that semi-convective layers in stars of our interest are temporarily stable and provide only a small contribution to convective mixing processes.

Zusammenfassung

Doppel-diffusive Konvektionsvorgänge, insbesondere Semikonvektion, sind von grosser Bedeutung in mehrkomponentigen fluiddynamischen Mischungsprozessen. Im astrophysikalischen Zusammenhang kann Semikonvektion ganau dann auftreten, wenn ein stabiler Molekulargewichtsgradient einem instabilen Temperaturgradient entgegenwirkt. Direkte numerische Simulationen von doppel-diffusiven Mischungsvorgängen sind mit den derzeitigen numerischen Methoden nur unter grösstem Rechenaufwand durchführbar. Aus diesem Grund wurde ein Model entwickelt, welches kompressible und inkompressible semi-konvektive Strömungen beschreibt und zeitgleich eine Extrapolation mit Potenzgesetzen in einen realistischen Parameterbereich erlaubt. Um die physikalischen Vorgänge der einzelnen Schichten besser verstehen zu können, wurde eine genaue Analyse mit hochaufgelösten numerischen Simulationen durchgeführt. Das Simulationsprogramm wurde mit MPI© und OpenMP© hybrid parallelisiert. Dies erst ermöglicht den Einsatz von Höchstleistungsrechnern. Der erste Teil der vorliegenden Arbeit beschäftigt sich mit der Modellbildung und mit dem mathematischen und physikalischen Vergleich kompressibler und inkompressibler doppel-diffusiver Fluide. Die zweikomponenten-Gleichungen, welche diese kompressiblen Strömungen beschreiben, wurden mit der Charakteristikenmethode im Eigenraum gelöst. Dies garantiert physikalisch korrektere Lösungen. Die numerische Lösung der advektiven Gleichungsterme wurde mit einem gewichteten nicht-oszillierenden Schema approximiert. Die inkompressiblen Strömungsgleichungen wurden auf einem gestaffelten numerischen Gitter mit einem semi-impliziten Schema gelöst. Die Kombination dieses speziellen numerischen Gitters mit dem nicht-oszillierend Advektionslösers stellt eine numerisch sehr stabile Struktur dar. Der zweite Teil der Arbeit präsentiert die zugehörigen numerischen Experimente und vergleicht diese Resultate mit theoretischen Vorhersagen. Es wurde eine detailierte Parameterstudie mit variierender Prandtl,- Lewis,- Rayleighzahl und dem Stabilitätsparameter R_ρ durchgeführt. Theoretische Potenzgesetze, welche Massen- und Wärmeflüsse in rein konvektiven Strömungen beschrieben, konnten auch für den semikonvektiven Fall in gewissen Parameterbereichen verifiziert werden. Darüber hinaus gelang die Stabilisierung einzelner semikonvektiver Schichten in Multischichtumgebungen. Die gewonnenen Resultate wurden verwendet um eine Extrapolation unter Zuhilfenahme eines Potenzgesetzes in den realistischen stellaren Parameterbereich vorzunehmen. Es konnte gezeigt werden, dass die semikonvektive Schichtung temporal stabil ist und nur wenig Einfluss auf die konvektiven Mischungsprozesse in Sternen hat.

Contents

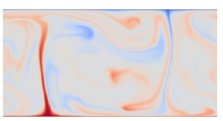

Introduction

Latte Macchiato (ital.: "spotted milk") is one of the most popular variations of coffee-drinks in Europe. The typical layered structure does not occur with the help of the server's coffee brewing skills alone, no, it forms under certain circumstances by 'itself'. Indeed, it is tasteful, but this Italian coffee shows the effects of a fluid-mechanics process called *double-diffusive convection*.

In this thesis the mathematical and physical properties of double-diffusive convection are analyzed to get deeper insight into these mixing processes. Usually, double-diffusive convection is analyzed in liquids or plasmas. This thesis presents numerical simulations for the two fluids and compares their outcomes.

It is important to take into account the different degree of compressibility when modelling double-diffusive fluid flows in water and plasma. Because of this physical difference, the mathematical and numerical treatment of both fluids changes dramatically. The incompressibility constraint alters the type of the underlying partial differential equations, hence the method to solve these equations has to be changed. Compressible fluid flows can be solved explicitly eg. in a conserved formulation and and with an essentially non-oscillatory finite difference method. Due to the fact that this direct ansatz covers resolves sound waves, the computational effort is very high. Incompressible fluid equations in conserved variables usually need a (semi)-implicit numerical treatment, because a resulting Poisson equation has to be solved. Physical modelling constraints lead to bigger numerical time steps, but also to a shift into a physically different regime. A valid comparison of the outcome of numerical simulations is not possible anymore with standard methods, because the incompressible fluid models have these 'physical deficiencies'. Dimensionless numbers can help understanding fluid flows. A couple of these numbers is introduced in this thesis. In addition, some modified numbers are presented to guarantee a valid comparison of liquid and gaseous fluids.

In order to model double-diffusive convection we use two classical approaches. We combine two numerical high order methods in the treatment of the hydrodynamical dynamic equations. The incompressible water equations are solved in the Boussinesq approximation, where the fluxes are reconstructed by a weighted MachENO [12] scheme in 5th order. For the compressible gas/plasma equations respectively we use a Riemann solver. This solver is based on a weighted ENO 5th order scheme on a collocated grid.

The printed version of this thesis has a movie included. To activate this feature just use your thumb.

'Hot air tends to rise.' This effect is known from the air above a radiator or from clouds in the atmosphere. The physical process behind this phenomenon is called

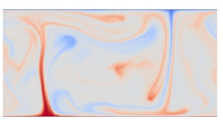

convection. Atmospheric convection can form clouds, when warm humid air rises and condenses on microscopic particles. Consequently cloud towers form, which might lead to thunderstorms. An extended Cumulonimbus cloud [9] over Munich (Germany) is shown in figure 1. Another convective regime is the mantle of our earth, where hot magma, heated by the earth core, forms convective rolls, which is the motor for continental drift. Figure 2 depicts the convection roles in the earth mantle, [45]. In principle thermal convection occurs, when the temperature field is unstable due to the 'natural' background stratification. But what happens, if the unstable temperature field is stabilised by an additional physical quantity, e.g. a concentration field like salt? The answer to this question is the topic of this thesis.

Figure 1: Cumulonimbus cloud over Munich

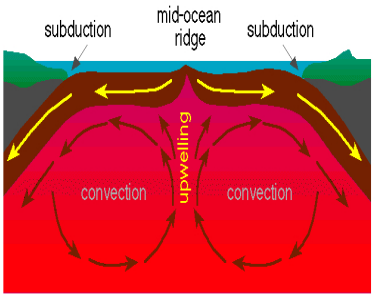

Figure 2: Sketch of the earth mantle convection

When the convective transport does not depend on the temperature gradient only, but on an additional scalar field like salt- or helium concentration, then double-diffusive convection can occur. The name 'double-diffusive convection' implies that two diffusion coefficients influence the motion. In the oceans double-diffusive convection can form *salt-fingers* (see figure 4), while the well-known Latte Macchiato layers (see figure 3) are a result of another double-diffusive phenomenon, which in astrophysics is called *semi-convection*. In the evolution of stars semi-convection plays an important role. When cold hydrogen-rich matter is stratified above hot helium-rich matter, double-diffusive processes can lead to layered structures. The main question which arises concerns the influence of the double-diffusive mixing processes on the evolution of high mass stars ($M > 15M_{\odot}$). Due to the fact that numerical simulations cannot cover the realistic parameter space, it is necessary to extrapolate into this range. Experiment-based and theoretical power laws give the possibility to do this. Hence, it is important to verify existing power laws with numerical experiments in a feasible parameter space to allow a valid extrapolation into the realistic range. Semi-convective layering and salt-fingers can be reproduced experimentally by 'indoor' experiments. The following experiments (figures 3, 4) illustrate both phenomena. Double-diffusive layers are known from Latte Macchiato, while saltfingers can be formed with ink and water.

In oceans semi-convection takes place when cold fresh water of melting icebergs

Figure 3: Latte Macchiato, indoor experiment supported by WMF bistro© done by the author at the Max-Planck institute for astrophysics

Figure 4: Saltfingers, [4] (priv. comm.), indoor experiment done with warm water and ink. The 'first generation fingers' can be observed.

stratifies above the warmer salty water. In salt lakes, where salty water and fresh water mix, semi-convection leads also to its typical layered structure (Kivu lake figure 5, see [41]). The layers can be observed with probes in salinity and temperature. A horizontal mean of these quantities shows a step like structure.

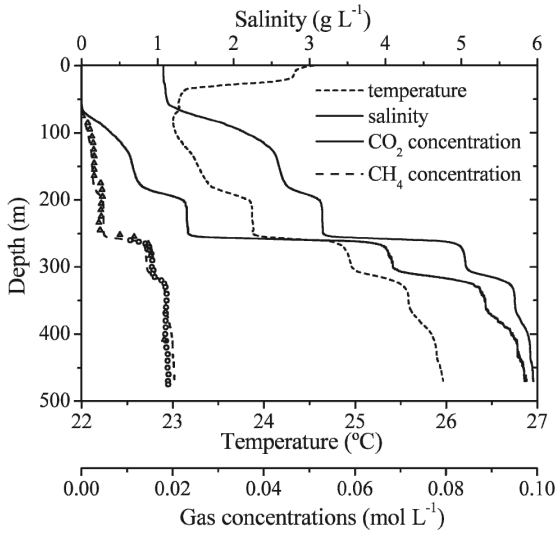

Figure 5: Temperature and salinity stratification in Lake Kivu. Schmid et al [41]

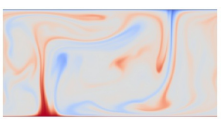

Overview of this thesis

1 Double-diffusive convection

A simple model for convection and double-diffusive convection is presented. A major problem is the determination of the vertical extension of a single semi-convective layer. This can be answered by introducing the dimensionless number Ra_*. The input model is based on only four dimensionless numbers, which will be presented.

2 Governing equations for binary mixtures

Compressible and incompressible fluid dynamical equations for double-diffusive convection are derived. Some basic thermodynamical relations (ideal gas) close the set of equations.

3 Numerical methods

The numerical algorithms to solve the fluid mechanical equations are presented here. The treatment of both sets of equations is quite different. While compressible fluids can be solved directly with explicit methods, incompressible fluids need more adapted numerical methods. A parallel numerical algorithm for solving the Poisson equation and the presentation of the ANTARES code complete this section. The compressibility is an important physical property of a fluid. Even though it is not obvious, one cannot compare two fluids with different degree of compressibility directly. The interpretation of mass and heat fluxes has to be changed. An overview about this topic can be looked up in this chapter.

4 Numerical simulations

The equations governed in chapter 2 are solved on rectangular grids in 2D with finite differences. A wide parameter space was used to verify and extend existing theories about double-diffusive mixing. A comparison between compressible and incompressible fluids is done on the same spatial scales.

Chapter 1

Double-diffusive convection

In this section a dimensionless model for convection and for double-diffusive convection is presented. It will be shown that only four dimensionless numbers and a couple of additional model constrains are necessary to describe the fluid flow of our interest. The main advantage of this ansatz is the independence of physical constraints and fixed physical parameters. Hence, the model is independent of underlying thermodynamic relations.

1.1 Convection

Assume that a fluid column is layered hydrostatically[1]. Although this system is in mechanical equilibrium, because of the hydrostatic assumption, it must not be in thermal equilibrium. The hydrostatic equilibrium is described by[2],

$$\frac{\partial P}{\partial z} + \rho g_z = 0 \tag{1.1.1}$$

the thermal equilibrium gives the adiabatic lapse rate[3],

$$\frac{\partial T}{\partial z} + \frac{g_z}{c_P} = 0 \tag{1.1.2}$$

If $\frac{g_z}{c_P} < 0$, then the first term $\frac{\partial T}{\partial z}$ needs to be positive in order to fulfill the equation. This can only be realised by an increase of the temperature in positive vertical direction, e.g. higher temperature on the top of the fluid column. Figure 1.1 depicts a fluid column, which is in mechanical and in thermal equilibrium.

[1] This can be realized by setting the fluid velocity $\vec{u} = 0$ in equation (2.3.12).
[2] [27]§3
[3] [35]

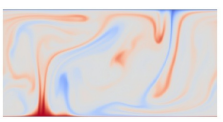

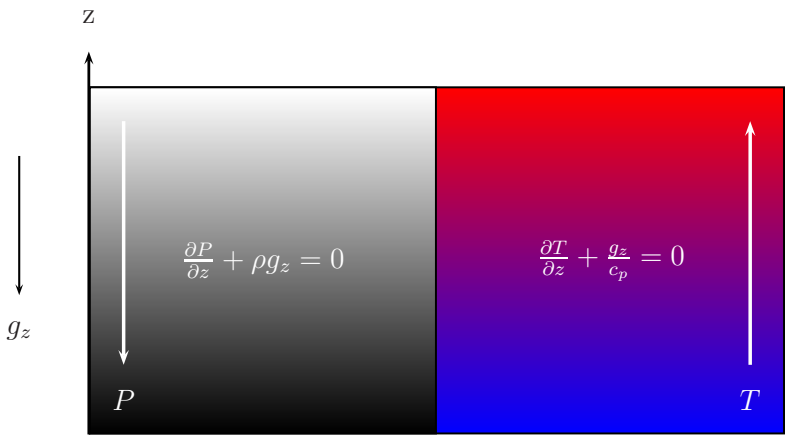

Figure 1.1: Fluid column in mechanical and thermal equilibrium.

There are three physical processes which are able to balance an unstable thermal disequilibrium.

- thermal conduction
- thermal convection
- radiation (not assumed for this model)

Thermal conduction is based on thermal diffusion and dominates regimes, where the temperature gradient is flatter than the adiabatic lapse rate. Convection is a buoyancy driven process and sets in, when the temperature gradient (for later considerations also the mean molecular weight gradient) is comparatively steep. This phenomenon can be described with one single dimensionless number, the thermal Rayleigh number, Ra_T. It describes the behavior of convective motion. Convection occurs, when a critical value of the thermal Rayleigh number is exceeded (eg. $(Ra_T)_{crit} > 1708$ for water[4]). The critical thermal Rayleigh number is a fluid dependent quantity. This dimensional less number depends on the thermodynamical quantities (Temperature, thermal diffusivity, viscosity) as well as on external parameters, like the boundary conditions, gravitational acceleration or the height of the fluid column. The thermal conduction dominates in water when eg. $(Ra_T)_{\text{crit}} < 1708$. See Turner et al [48] for a more detailed view on the critical Rayleigh number. Convection becomes efficient in mixing fluids if,

$$(Ra_T)_{\text{crit}} << Ra_T, \tag{1.1.3}$$

where the symbols are explained in the appendix B.2. The thermal Rayleigh number

[4] [27]§57

is defined as,

$$Ra_T = \frac{g\alpha_T \Delta T H^3}{\kappa_T \nu} = \frac{g(\nabla - \nabla_{\rm ad}) H^4}{H_P \kappa_T \nu} \tag{1.1.4}$$

For incompressible fluids, the first formulation is used, while in the compressible astrophysical context, the second formulation is preferred. The Rayleigh number looks more familiar when we split the fraction and analyze each part in terms of dimensional analysis,

$$Ra_T = \frac{g(\nabla - \nabla_{\rm ad})}{H_P} \frac{H^2}{\kappa_T} \frac{H^2}{\nu} \tag{1.1.5}$$

$$Ra_T[1] = \frac{g[cm/s^2](\nabla - \nabla_{\rm ad})[1]}{H_P[cm]} \frac{H^2[cm^2]}{\kappa_T[cm^2/s]} \frac{H^2[cm^2]}{\nu[cm^2/s]} \tag{1.1.6}$$

The Rayleigh number couples the buoyancy time scale with the thermal and the viscous diffusion time scales, while the diffusion time scale is definded as, $\tau_{\rm diff} = \frac{H^2}{\kappa_{\rm diff}}$. Typical values for the Rayleigh number in stars are $Ra_T = 10^{12} - 10^{14}$. The parameter space for Ra_T of the numerical experiments is limited by the resolution of the corresponding diffusive boundary layer, see section B.1. This leads to values of about $Ra_T = 10^5 - 10^7$. It is not so far off to define a negative Rayleigh number, in case of a negative temperature gradient. In this situation, the system is stable against convection. Finally, the following four cases are distinguished:

- $0 < (Ra_T)_{crit} < Ra_T$: unstable, convective
- $0 < Ra_T < (Ra_T)_{\rm crit}$: stable, conductive
- $Ra_T = 0$: stable, isothermal ($T = const.$) or $\nabla = \nabla_{\rm ad}$
- $Ra_T < 0$: stable, no convection

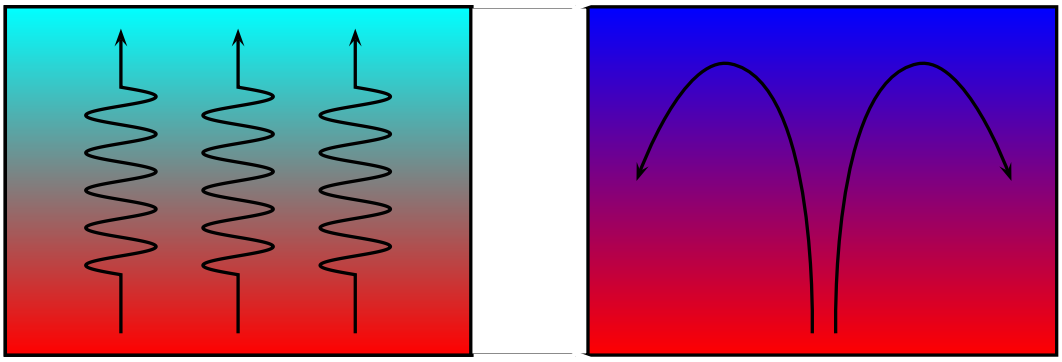

Figure 1.2: conductive ($Ra_T < (Ra_T)_{\rm crit}$) and convective regime ($Ra_T > (Ra_T)_{\rm crit}$)

1.2 Double-diffusive convection

As mentioned before convection depends mainly on the temperature gradient. Double-diffusive convection depends on a second scalar field, e.g. salt- or Helium

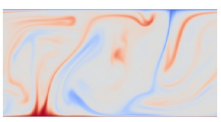

concentration. A mixture of two fluids is assumed to be stratified, such that a thermal gradient as well as a concentration gradient exists. Two important cases of double-diffusive convection are distinguished.

- *Semi-convection* occurs, when the temperature gradient destabilizes, while the concentration gradient stabilizes the system. This happens for instance, when cold fresh water is stratified above hot salty water. The name 'semi-convection' suggests that convection is in a certain meaning damped or inhibited. This leads to interesting effects, like oscillatory instabilities and/or layering of the fluid. The layers in Latte Macchiato are an outcome of semi-convective mixing. In the stellar core of a main sequence star, hydrogen is converted to helium in the proton-proton chain. As a result the helium content in regions next to the core is higher than in outer regions of the star. A stable stratification in the mean molecular weight (here helium concentration) and a layering of the plasma results.

- The second important double-diffusive process is the formation of salt-fingers. This happens, when saline warm water is stratified above cold fresh water. This phenomenon can be observed in oceans (Street of Gibraltar, beneath the Mediterranean outflow cf. Magnell [30]) or in indoor experiments (see figure 4) and in stars (helium-fingers). In this case the temperature field is convectively stable and the concentration gradient destabilises the equilibrium.

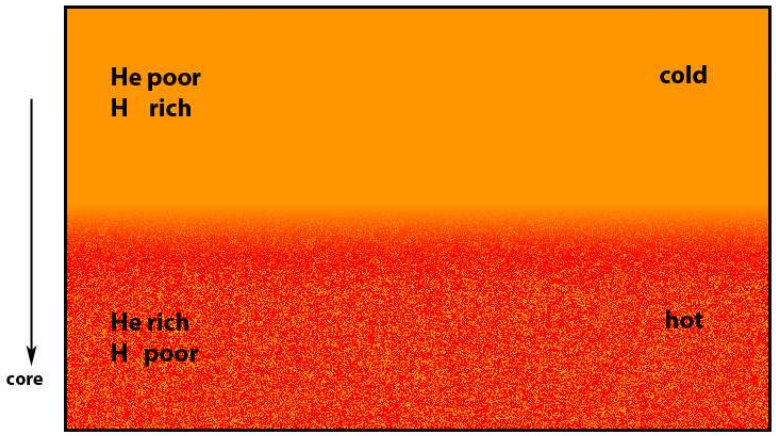

Figure 1.3: Stellar semi-convective stratification

This thesis concentrates on semi-convection in an idealized astrophysical framework. Semi-convection plays an important role in the evolution of stars. The mixing of helium into deeper layers of stars leads to shorter evolution time scales. And this affects the lifetime of a star. Due to the 'natural' stratification of a star (low temperatures at the surface, high temperatures in the centre), semi-convection occurs more often than the salt-finger instability.

1.3 Semi-convection

We follow the same ansatz as for convection. Semi-convection can be introduced with the thermal Rayleigh number and an additional dimensionless number, the saline Rayleigh number,

$$Ra_S = \frac{g\alpha_S \Delta S H^3}{\kappa_T \nu} = \frac{g\nabla_\mu H^4}{H_P \kappa_T \nu} \tag{1.3.1}$$

For incompressible fluids the first formulation is used, while in the compressible astrophysical context, the second formulation is preferred. The saline Rayleigh number is similar to the thermal Rayleigh number, except for the numerator, where the mean molecular weight gradient occurs. A critical saline Rayleigh number can also be defined, but is not used for our experiments. Like the thermal Rayleigh number the saline Rayleigh number becomes negative, when the saline gradient is inverted. Similar to the thermal Rayleigh number, the following cases can be distinguished:

- $Ra_S > 0$: stable stratification
- $Ra_S < 0$: unstable stratification

Forming the fraction of the thermal and the saline Rayleigh number, leads to a stability parameter, which will be of major interest.

$$R_\rho = \frac{Ra_S}{Ra_T} = \frac{\alpha_S \Delta S}{\alpha_T \Delta T} = \frac{\nabla_\mu}{\nabla - \nabla_{\mathrm{ad}}} \tag{1.3.2}$$

This dimensionless number characterises the stability due to double-diffusive convection and is typically in the range of $0.1 < R_\rho < 10$. The bifurcation point between the stable and the unstable concentration field is $R_\rho = 1$. In case of salt-fingers the stability parameter is inverted and becomes,

$$(R_\rho)_{\mathrm{salt-finger}} = R_\rho^{-1} = \frac{Ra_T}{Ra_S} \tag{1.3.3}$$

This allows a comparison between semi-convection and salt-fingers. Sometimes the designation R_μ can be found, which is identical to R_ρ, but underlines the astrophysical context. When both numbers, Ra_T and Ra_S, are plotted in a grid the stability map (figure 1.4) results.

The two semi-convective scenarios can be described as follows: An unstable temperature field ($Ra_T > 0$) is stabilised by an stable saline field, ($Ra_S > 0$). As long as $R_\rho < 1$ 'natural' convection sets in. If $R_\rho > 1$ the concentration field stabilises the thermal temperature field in such a way that natural convection cannot fully develop. This 'inhibited' convection leads to oscillations and/or to layering of the fluid. A lot of theoretical work has been done on this field. The reader is invited to work through Huppert and Moore [23] and the comprehensive thesis of J. Bascoul [2]. Salt-fingers

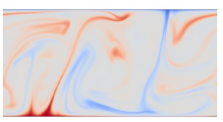

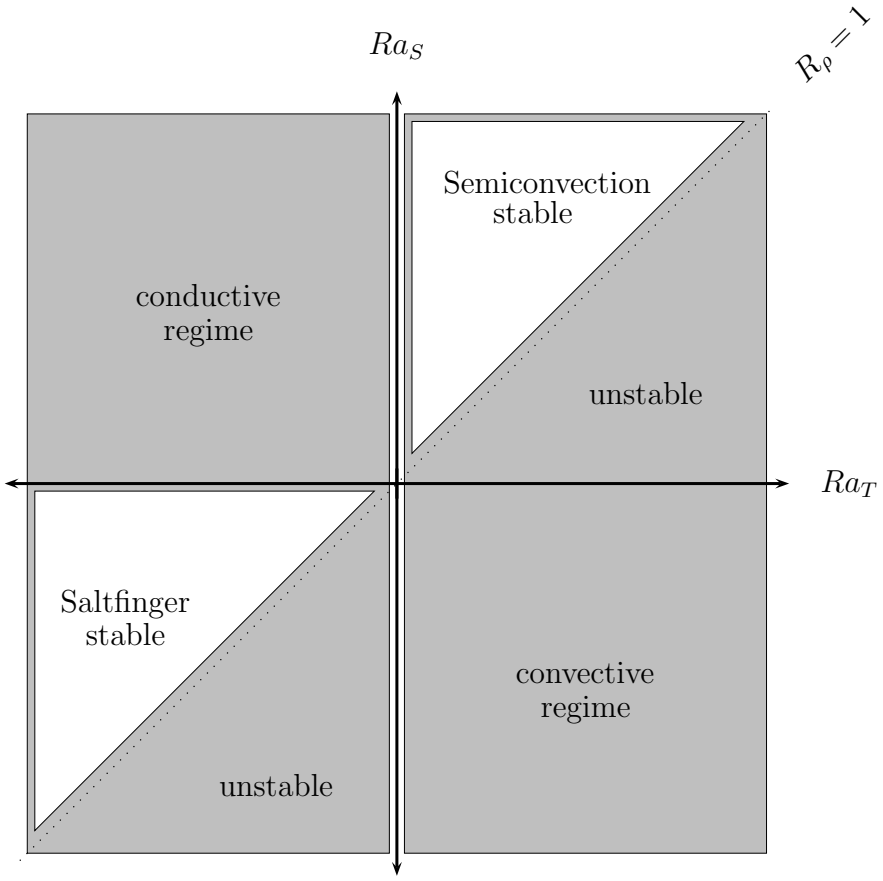

Figure 1.4: Double-diffusive regimes depending on the Rayleigh numbers.

are in a sense the inverted regime of semi-convection. A stable temperature field ($Ra_T < 0$) is de-stabilised by a concentration field ($Ra_S < 0$). An instability develops, which has a similar optical appearance to the Rayleigh-Taylor instability, but it is physically different. The RT-instability is advection driven, salt-fingers are an outcome of a diffusive process.

We collect all considerations and form the set of inequalities which describe (Ledoux) stable semi-convection in the astrophysical context. The real temperature gradient ∇, the mean molecular weight gradient ∇_μ and the adiabatic gradient ∇ad are defined in Appendix A.

$$\nabla - \nabla_{\text{ad}} > 0 \tag{1.3.4}$$

$$\nabla_\mu > 0 \tag{1.3.5}$$

$$\nabla_\mu > \nabla - \nabla_{\text{ad}} \tag{1.3.6}$$

The (Ledoux) unstable semi-convection in the astrophysical context fulfills,

$$\nabla - \nabla_{\text{ad}} > 0 \tag{1.3.7}$$

$$\nabla_\mu > 0 \tag{1.3.8}$$

$$\nabla_\mu < \nabla - \nabla_{\text{ad}} \tag{1.3.9}$$

1.4 Dimensionless fluid dynamical numbers

The Rayleigh numbers depend on diffusive time scales, which implies that the diffusion coefficients need to be known. The diffusion coefficients are parameterised in form of dimensionless numbers. These numbers are now introduced:

Prandtl number: Pr / σ

The Prandtl number Pr (or σ) is defined as: $Pr = \frac{\nu}{\kappa_T}$. It characterises the amount of heat 'produced' by internal friction (momentum diffusion coefficient ν) over heat dissipation through flow (thermal diffusion coefficient κ_T). For instance, cooling nuclear reactors can lead to severe problems. The heat flux of the nuclear reaction is so high that it is very difficult to transport it efficiently and fast. Fluids which are viscous *and* are able to conduct heat very fast are needed. Therefore, metals like liquid sodium are used, which has $\sigma = 10^{-2}$. Oil ($\sigma = 10^4$), which has a similar viscosity as liquid metal, would not be able to conduct heat as fast as liquid sodium.

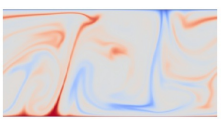

Typical values for σ are[5]:

- approx. 0.7 for air
- 7 for water at $20°C$
- $10^2 - 10^4$ for engine oil
- 4.4×10^{-3} liquid mercury
- $10^{-6} - 10^{-7}$ stellar plasma

Modified Rayleigh number: Ra_*

Multiplying the thermal Rayleigh number with the Prandtl number leads to a viscosity free, modified formulation of Ra_T,

$$Ra_* = Ra_T \cdot \sigma = \Big(\frac{g\alpha_T \Delta T H^3}{\kappa_T \nu}\Big)\Big(\frac{\nu}{\kappa_T}\Big) = \frac{g\alpha_T \Delta T H^3}{\kappa_T^2} = \frac{g(\nabla - \nabla_{ad})H^4}{H_P \kappa_T^2} \qquad (1.4.1)$$

It can be shown with the mixing length theory[6] that Ra_* gives a technical help to estimate the thickness of diffusive boundary layers in semi-convection zones. In numerical simulations it helps to find the minimum resolution which is needed to resolve the thermal- and concentration boundary layers sufficiently. See appendix B.1 for the derivation of the boundary layer thickness and an example for our numerical simulations. The main advantage of choosing Ra_* instead of Ra_T is the independence of the viscosity ν. Therefore, we set Ra_* as an input parameter for the numerical simulations.

Lewis number: Le / τ

The Lewis number Le (or τ)[7] is defined as: $Le = \frac{\kappa_S}{\kappa_T}$. It is the fraction of the concentration diffusion coefficient κ_S over the thermal diffusion coefficient κ_T. Concentration diffusion is known from our lungs, where oxygen diffuses trough a membrane into the blood. Another mass concentration diffusion phenomenon can be observed in helium balloons for children, when helium diffuses through the membrane into the surrounding air of a balloon after some days. As a result, the balloon shrinks. Typical values for τ are[8] :

- 10^{-2} for water
- 10^{-8} plasma in the semi-convection zone of a star

Especially the oceanographic community uses the inverted Lewis number $\tau_{\mathrm{OG}} = \frac{\kappa_T}{\kappa_S}$.

[5] [27] §53
[6] eg. Kippenhahn [24]§7
[7] In this thesis the letter τ is used for the Lewis number and for time scales, which are always denoted with an index. It should be clear from the context which quantity is meant.
[8] [39]

Schmidt number: *Sc*

The Schmidt number Sc is defined as: $Sc = \frac{Pr}{Le} = \frac{\nu}{\kappa_S}$. This number characterizes the fraction of the momentum diffusion coefficient over the concentration diffusion coefficient and plays a common role in fluids with both, momentum and mass diffusion convection processes. It physically relates the relative thickness of the hydrodynamic layer and mass-transfer boundary layer, [50]. Typical values for Sc are :

- 10^2 for water
- 10^2 plasma in the semi-convection zone of a star

On the first sight stars and oceans seems not comparable. But the same value of the Schmidt number gives a link to compare both regimes. Water and plasma currents are usually described with the same fluid dynamical equations. Only the material parameters are different. The dimensionless ratio of the viscosity to the saline (Helium) diffusion coefficient indicates that both fluids behave in a certain sense equal. For instance, salt-fingers and semi-convective layering is assumed in stars as well as in oceans, although the temperature scales and other thermodynamical quantities are in completely different ranges.

1.5 The initial value problem for the double-diffusive convection theory

In the following the initial model setup for the incompressible solver (see section 3.5) is discussed. We choose a rectilinear box geometry, where the box height is set to $H = 1$ and the spacing Δx according to the resolution (typically 400 points). The width $a \cdot H$ depends on an aspect ratio relative to the box height and is usually set to $a = 2$. Because the code is based on a program for solar atmosphere calculations the origin of the co-ordinates is set to the upper left corner. The x-axis is left, vertically downwards aligned, the y-axis and the z-axis are horizontally positively aligned (see the figure 1.5 for details). The upper boundary is always denoted with an 'a' in the index, while the lower boundary is denoted with an 'b'. The four input parameters are: σ, τ, Ra_* and R_ρ. Additionally, several fixed parameters and quantities have to be set, which take the following values for the incompressible case.

- gravitational acceleration $g_z = 1$
- temperature difference $\Delta T = 0.05$
- height $H_{\mathrm{BA}} = 1$, width $a \cdot H_{\mathrm{BA}} = 2$
- $T_a = 1.0$, $S_a = 1.0$, $\rho \equiv 1.0$

To complete the initial model set, an appropriate initial stratification for temperature, salinity, and density is needed. There are different possibilities to stratify these variables:

- linear vertical stratification (convection, semi-convection)
- step, double-step and multi-step layering (convection, semi-convection)
- sharp middle diffusive layer (salt-fingers, Rayleigh-Taylor instability)

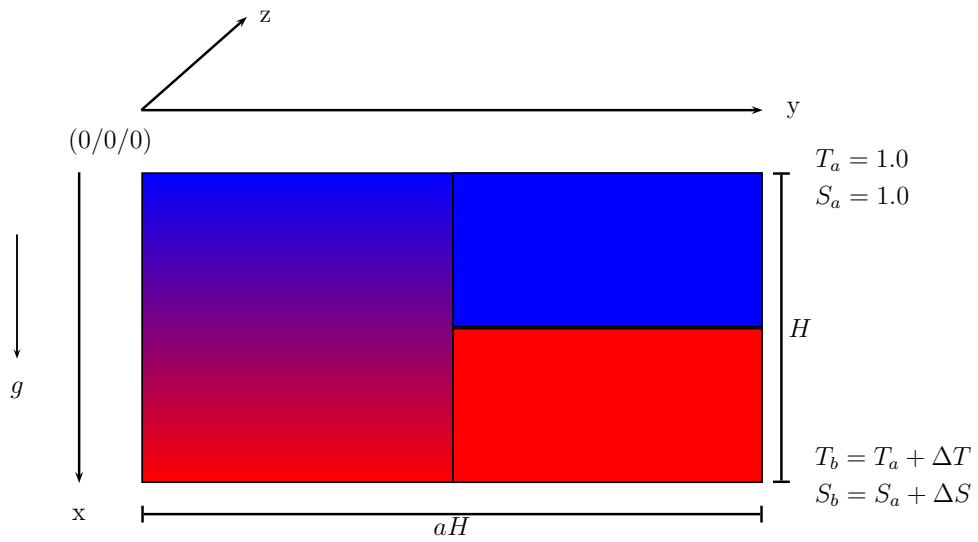

Figure 1.5: Sketch of the initial simulation box with different initial stratifications.

After the initial layering process a perturbation is applied to the salinity field. The amplitude of this perturbation is of the order of 10^{-4} when compared with the background reference stratification. Other fields should not be perturbed, because for instance the velocity vector field has to be solenoidal (see equation (2.4.1)). If the initial stratification is perturbed with a random perturbation in an arbitrary velocity direction, a Poisson equation remains to be solved. Since the temperature field is coupled with a too high diffusion term (see equation (2.4.49)), small perturbations would not 'survive' long enough.

Chapter 2

Governing equations for binary mixtures

2.1 Motivation

The four commonly known states of matter are: solid, liquid, gas and plasma. Convective and semi-convective processes can only occur when particles are able to move freely. In a thermodynamical sense an idealised gas and high temperature plasma can be treated in the same way. Hence, only liquids and gaseous states are interesting for the following discussion.

Differences in these states of matter can be described in terms of thermodynamics. The thermodynamics of gas and plasma follows the ideal gas equation (2.2.1) which is a commonly used simplification to describe both states as long as the densities are low enough. This equation of state (in the following EOS) is usually a model constraint for the fluid motion equations, because the internal energy is coupled to the pressure with an algebraic equation. Due to this physical pressure constraint effects like compressibility and therefore sound waves can be described. In contrast to gas or plasma, the thermodynamic pressure in liquids is (nearly) independent of the density. This results in the most obvious difference between gas/plasma and liquids - its volume expansion coefficient.

There are several approaches for modelling double-diffusive convection with numerical algorithms. Depending on the regime of interest (water, gas, plasma) the following methods for different degrees of compressibility have been established:

- *fully compressible approach - (compr)*

  Especially in stars, where the semi-convection zones are very extended (some pressure scale heights), the full compressible Navier-Stokes equations have to be used, because pressure differences are high. The numerical time step is limited

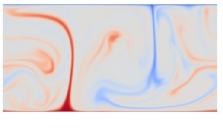

by the sound speed. The computational effort for simulations of compressible fluids is usually very high. Massively parallel supercomputers are used for these kind of simulations. The advantage of this set of equations is the fact that all physically relevant processes can be covered. Furthermore, the simulated domain can 'easily' be parallelised with decomposition methods (MPI) as long as the equations 'allow' this.

- *anelastic approximation - (AA)*

  Variations in the background stratification of thermodynamic variables are assumed to be small, which leads to small fluid velocities. Additionally, the anelastic approximation suppresses sound waves and therefore larger time steps are possible in numerical schemes. The anelastic approximation is mainly used in meteorology, where convectively unstable zones (e.g. troposphere) are not extended much, $H_P < 1$. The computational cost depends strongly on the Poisson solver used. Good parallel solvers are always welcome.

- *Boussinesq approximation - (BA)*

  The Boussinesq approximation is a more restricted method than the anelastic approximation. This approximation is used to simulate fluids with extremely small fluctuations in thermodynamic quantities. Even density fluctuations are ignored, except in the buoyancy term of the Navier-Stokes equation. This leads to a very 'strict' incompressibility and can lead to very large numerical time steps. The Boussinesq approximation is nearly independent from the underlying thermodynamics. This results in similar equations for water and gas, as long as the pressure scale height is large enough compared to the height of the simulated fluid column.

There are several ways to distinguish between compressible and incompressible flows. One of them uses the Mach number as a criterion. A fluid is assumed to be incompressible, if the Mach number $Ma < 0.3$ (see Lesieur [28] p33). A windstorm on earth has an average speed of $100km/h = 2777cm/s$. The sound speed of air at sea level is $c_s = 1188km/h = 33000cm/s$.

$Ma(\text{wind storm}) = 2777/33000 = 0.08$

This example shows that apparently compressible fluid flows can be simulated with the anelastic- or the Boussinesq approximation even when the velocities appear to be high.

Fluid dynamical equations

The Navier-Stokes equations are a system of nonlinear partial differential equations. This system describes the motion of viscous fluids like liquid, gas or plasma. One basic physical property of a fluid is its compressibility. Neglecting the fluid veloc-

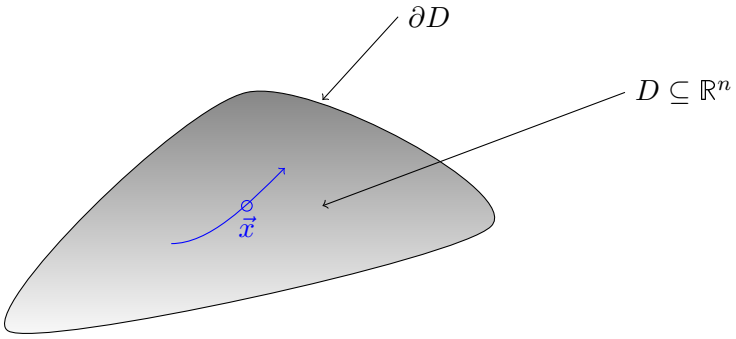

Figure 2.1: Idealised fluid parcel.

ity limitation ($Ma < 0.3$), liquids, like water, are usually treated as incompressible fluids, while gas or plasma are compressible. This fact has to be taken into account when analysing and modelling fluids. From a mathematical point of view the (salt)-water equations are incompressible because the incompressibility constraint is fulfilled. But, the density is coupled to an equation of state, which means that from a physical point of view is is not incompressible. Hence, the 'type' of incompressibility underlays modeling constraints. The mathematical incompressibility constraint $\nabla \cdot \vec{u}$ is a property of the flow, while the eg. volume expansion coefficients are an property of the fluid. One of the most common approaches to obtain the Navier-Stokes equations for both, compressible and incompressible fluids is the derivation of the equations for an unspecific compressible fluid, and then using model constraints to derive the incompressible equations. In our case the water equations are solved in the Boussinesq approximation, while the gas and plasma equations are treated as fully compressible.

Let $D \subseteq \mathbb{R}^n$ be a region filled with a fluid. $\vec{x} \in D \subseteq \mathbb{R}^n$ is an arbitrary point in D. A fluid particle moves through $\vec{x}$ at time t along a trajectory. We are using the following physical quantities to describe this fluid particle:

- $\rho(\vec{x}, t)$ density
- $\vec{c}(\vec{x}, t)$ concentration
- $\vec{u}(\vec{x}, t)$ velocity
- $\vec{p}(\vec{x}, t)$ momentum
- $T(\vec{x}, t)$ temperature
- $e(\vec{x}, t)$ internal energy
- $P(\vec{x}, t)$ pressure

Other (mostly thermodynamical) quantities are introduced later. Without loss of generality the latter quantities are rewritten without spatial and temporal co-

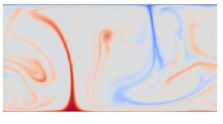

ordinates (e.g. $\vec{u} := \vec{u}(\vec{x}, t)$), just to allow a fluent reading. A list of all used symbols can be found in the appendix B.2.

2.2 Thermodynamic relations

The following thermodynamic relations describe the monoatomic ideal gas, which is the basic physical state of all our considerations,

$$P = \frac{\mathcal{R}\rho T}{\mu} \tag{2.2.1}$$

$$\gamma = 5/3 \tag{2.2.2}$$

$$c_P - c_V = \frac{\mathcal{R}}{\mu} \tag{2.2.3}$$

$$\gamma - 1 = \frac{\mathcal{R}}{\mu\, c_V} \tag{2.2.4}$$

$$\nabla_{\text{ad}} = \frac{\gamma - 1}{\gamma} \tag{2.2.5}$$

$$\mu = \mu(\vec{c}) \tag{2.2.6}$$

The notation of the latter quantities follows [49]. The ideal gas is a simple, but very useful idealised fluid, which approximates real gas well for our purpose. An extension to a stellar parameter space ($T \approx 2.0 \times 10^7 K$ and ionization) can be done with an additional radiation pressure term in (2.2.1), but is not considered in this thesis.

In contrast to compressible fluids, the thermodynamics used for the Boussinesq approximation is surprisingly simple. Pressure and density are not coupled anymore, which leads to a 'EOS'-free formulation. The pressure is calculated implicitly with a constraint, which is explained in details in section 2.4.1. Only the buoyancy term is affected by temperature and concentration variations.

2.3 The fully compressible approach

2.3.1 Conservation of mass

There are several ways to derive the law of mass conservation. A mathematical introduction is presented in Chorin [7] §1. For our purpose the following equation in conservation form is used.

$$\frac{\partial \rho}{\partial t} = -\nabla \cdot (\rho \vec{u}) \tag{2.3.1}$$

2.3.2 Partial mass conservation

Two equations are needed to derive the partial mass conservation. Firstly, the conservation of mass (2.3.1), secondly an equation for chemical concentration. The latter equation is a typical convection-diffusion equation. A comprehensive work on (irreversible) thermodynamic processes is De Groot and Mazur [16], which is highly recommended in this context. We begin with the concentration equation, which describes the temporal and spatial behavior a fluid parcel of species c. Here, the concentration c represents on specific, but arbitrary component of the vector $\vec{c} = (c_1, ..., c_n)^T$. We notice that,

$$\sum_i c_i = 1 \tag{2.3.2}$$

and obtain,

$$\frac{\partial c}{\partial t} = -\vec{u} \cdot \nabla c + \nabla \cdot (\kappa_c \nabla c), \tag{2.3.3}$$

where $\nabla^2 = \nabla \cdot \nabla$, κ_c is the mass diffusion coefficient for species c. In general κ_c depends on the thermodynamic and does not have to be constant. To reduce the complexity of our problem,

$$\kappa_c = \text{const.} \tag{2.3.4}$$

in the whole domain. An equation for the partial mass density $c\rho$ is then obtained in conservative form:

$$\frac{\partial (c\rho)}{\partial t} = \rho \cdot \frac{\partial c}{\partial t} + c \cdot \frac{\partial \rho}{\partial t} \tag{2.3.5}$$

$$\frac{\partial (c\rho)}{\partial t} = \rho \cdot (-\vec{u} \cdot \nabla c + \kappa_c \nabla^2 c) + c \cdot (-\nabla \cdot (\rho \vec{u})) \tag{2.3.6}$$

Using the identity, $\nabla \cdot (c\rho\vec{u}) = \rho\vec{u} \cdot \nabla c + c\nabla \cdot (\rho\vec{u})$, we obtain

$$\frac{\partial (c\rho)}{\partial t} = -\nabla \cdot (\rho c\, \vec{u}) + \rho \kappa_c \nabla^2 c \tag{2.3.7}$$

An alternative way to derive this equation can be realised by using two concentration evolution equations,

$$\frac{\partial (c_1\rho)}{\partial t} = -\nabla \cdot (\rho\vec{u} \cdot c_1 - \rho\kappa_{c1} \nabla c_1) \tag{2.3.8}$$

$$\frac{\partial (c_2\rho)}{\partial t} = -\nabla \cdot (\rho\vec{u} \cdot c_2 - \rho\kappa_{c2} \nabla c_2) \tag{2.3.9}$$

where $c_1 + c_2 = 1$. In binary mixtures the diffusion coefficients have to be equal[1], $\kappa_{c1} = \kappa_{c2}$. Additionally, $\nabla c_1 + \nabla c_2 = 0$. Summarizing both equations leads directly to (2.3.1). For our purpose the partial density equation and the concentration

[1] Both concentration fluxes must annihilate to gain conservation.

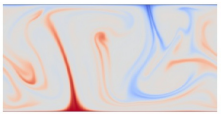

equation, respectively, are rewritten to,

$$\frac{\partial(S\rho)}{\partial t} = -\nabla \cdot (\rho\vec{u} \cdot S - \rho\kappa_S \nabla S) \tag{2.3.10}$$

The incompressible formulation of (2.3.10) becomes

$$\frac{\partial S}{\partial t} = -\nabla \cdot (\vec{u} \cdot S - \kappa_S \nabla S) \tag{2.3.11}$$

Equation (2.3.11) requires the incompressibility constraint $\frac{D\rho}{Dt} = 0$ and a constant density to be valid.

2.3.3 Navier-Stokes equation – momentum conservation

The momentum conservation equation is represented by the well-known Navier-Stokes equation[2],

$$\frac{\partial(\rho\vec{u})}{\partial t} + \nabla \cdot [\rho(\vec{u} \otimes \vec{u})] + \nabla \cdot \Pi = -\rho\, \nabla\phi \tag{2.3.12}$$

With $\Pi = P\,\mathbb{1} - \pi$ being the pressure tensor, $grad\,\phi$ an external force (eg. gravitational acceleration g) and π the viscosity tensor with its components,

$$\pi_{ik} = \eta \left(\frac{\partial u_i}{\partial x_k} + \frac{\partial u_k}{\partial x_i} - \frac{2}{3}\delta_{ik} \nabla \cdot \vec{u} \right) + \zeta \delta_{ik} \nabla \cdot \vec{u} \tag{2.3.13}$$

In equation (2.3.13) the Kronecker delta is denoted with δ_{ik}, the dynamic viscosity with η and the bulk or second viscosity with ζ. Using the incompressibility constraint $\frac{D\rho}{Dt}$ and $\rho \equiv \rho_0$ leads to the very simple form,

$$\pi_{ik} = \eta \left(\frac{\partial u_i}{\partial x_k} + \frac{\partial u_k}{\partial x_i} \right) = \nu\rho_0 \left(\frac{\partial u_i}{\partial x_k} + \frac{\partial u_k}{\partial x_i} \right) \tag{2.3.14}$$

The kinematic viscosity,

$$\nu = \frac{\eta}{\rho}$$

is now introduced, because of the assumed constant density ρ_0 in the incompressible regime of the Boussinesq approximation.

2.3.4 Energy conservation

The following derivation follows in some parts the lecture notes of Dullemond [11]. An overview about modelling the energy conservation equation in a star can be looked up in Hillebrandt, Kupka [22].

[2] here in the notation of Hillebrandt, Kupka [22]

A general formulation of an energy equation is presented. We start defining the total energy (per unit mass) as the sum of the internal energy and the kinetic energy

$$E = e + \frac{1}{2}|\vec{u}|^2. \tag{2.3.15}$$

An equation for the total energy density would take the form[3]:

$$\frac{\partial(\rho E)}{\partial t} + \nabla \cdot \mathbf{J}_e = -\vec{p}\nabla\,\phi + S \tag{2.3.16}$$

where $\mathbf{J}_e$ is the total energy flux and $\phi = g_z$ is an external source term. The quantity $S = Q_{\text{nuc}} = \nabla \cdot F_{\text{nuc}}$ gives the nuclear energy generation rate and will be discussed subsequently. $\mathbf{J}_e$ can be extended according to the physical environment. Several energy sources have to be taken into account in a star. Some of them are relevant, others will be dropped.

$$\mathbf{J}_e = (\rho E + P)\vec{u} - F_{\text{rad}} - F_{\text{cond}} - F_{\text{chem}} - \pi\vec{u} \tag{2.3.17}$$

- $(\rho E + P)\vec{u}$ ... energy term due to the potential and kinetic force
- F_{rad} ... radiative energy flux
- F_{cond} ... conductive heating flux
- F_{chem} ... chemical energy flux by diffusion
- $\pi\vec{u}$ ... energy release due to viscous forces

radiative energy flux F_{rad} and conductive heat flux F_{cond}

The diffusion approximation is valid as a solution for the radiative transfer equation, because of electron scattering[4] the regime is optically thick. This fact reduces the problem significantly,

$$F_{\text{rad}} = 0 \tag{2.3.18}$$

The heat flux takes the form,

$$F_{\text{cond}} = -K_h \cdot \nabla T \tag{2.3.19}$$

with K_h being the thermal conduction. In a realistic stellar model the heat flux can be formulated in terms of the Rosseland opacity κ_R,

$$F_{\text{cond}} = -\frac{4ac}{3\kappa_R\rho}T^3\nabla T \tag{2.3.20}$$

where a is the *radiation-density constant* and c the speed of light. Thompson- or

[3] In the ANTARES Code the quantity $\rho E \equiv Et$.

[4] In semi-convective zones of high mass stars of our interest. This is assumption is not valid for arbitrary double-diffusive zones.

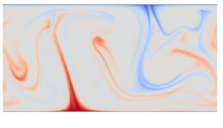

electron scattering dominates in the region of interest, so $\kappa_R \approx 0.2(1+X)$ (see [49]§16.6a), where X is the mass fraction of hydrogen. Consequently,

$$K_h = \frac{4ac}{3 \cdot 0.2(1+X)\rho} T^3 \tag{2.3.21}$$

and finally,

$$F_{\text{cond}} = -K_h \nabla T = -\frac{4ac}{3 \cdot 0.2(1+X)\rho} T^3 \nabla T \tag{2.3.22}$$

The depicted model should be independent from any specific physical regime. This means that the introduced thermal conductivity, which is only valid under the assumption of Thompson scattering, is replaced by an unspecified approach. In general,

$$K_h = \rho c_P \kappa_T \tag{2.3.23}$$

For our purpose the thermal diffusion coefficient κ_T is parameterized is terms of the modified Rayleigh number Ra_*, which is an elegant form for this value.

$$\kappa_T = \sqrt{\frac{g_z \nabla_\Theta H^4}{H_P \, Ra_*}} \tag{2.3.24}$$

$$F_{\text{cond}} = -\sqrt{\frac{g_z \nabla_\Theta H^4}{H_P \, Ra_*}} \rho c_P \nabla T \tag{2.3.25}$$

chemical flux F_{chem}

The following discussion of the derivative of the chemical flux is based on a private communication with Prof. Dirk Olbers, AWI Bremerhaven.

This is the energy flux caused by diffusion of partial masses. Under the assumption that we have a binary mixture (hydrogen/helium or fresh water/salt), the chemical flux can be derived as follows. A diffusive change of the volume element dq, where q could be a gas or salt concentration element causes an energy change of,

$$\frac{\partial H}{\partial q} dq \tag{2.3.26}$$

where H is the enthalpy. The diffusive flux transports the amount $\mathbf{F}_{\text{diff}} \cdot d\,A$ and hence the energy,

$$\frac{\partial H}{\partial q} \mathbf{F}_{\text{diff}} \, dA \tag{2.3.27}$$

through a surface element dA. The total energy transported out of the volume is thus,

$$\int_A \frac{\partial H}{\partial q} \mathbf{F}_{\text{diff}} \cdot dA = \int_A \mathbf{F}_{\text{chem}} \cdot dA \tag{2.3.28}$$

where the flux of the chemical energy is given by

$$\mathbf{F}_{\text{chem}} = \frac{\partial H}{\partial q}\mathbf{F}_{\text{diff}} \tag{2.3.29}$$

'The contribution of the chemical flux to the heat flux is so small that it can be neglected.'[5] . The basis of this consideration is the fact that the fluids are homogeneous mixtures and the simulated time scales are too short.

$$\mathbf{F}_{\text{chem}} = 0 \tag{2.3.30}$$

nuclear energy flux F_{nuc}

The simulated time scales are too short. Hence, the contribution of the nuclear reactions can be neglected.

$$\mathbf{F}_{\text{nuc}} = 0 \tag{2.3.31}$$

Energy equation for binary mixture

We collect all results and write down the total energy equation for a binary mixture,

$$\frac{\partial(\rho E)}{\partial t} + \nabla \cdot [\vec{u}(\rho E + P)] + \nabla \cdot (-\kappa_T \, \rho \, c_P \, \nabla T) + \nabla \cdot (-\pi \vec{u}) = -\vec{p} \, g_z \tag{2.3.32}$$

2.3.5 Set of compressible binary mixture equations

$$\frac{\partial \rho}{\partial t} = -\nabla \cdot (\rho \vec{u}) \tag{2.3.33}$$

$$\frac{\partial(c\rho)}{\partial t} = -\nabla \cdot (\rho \vec{u} \cdot c - \rho \kappa_c \nabla c) \tag{2.3.34}$$

$$\frac{\partial(\rho \vec{u})}{\partial t} = -\nabla \cdot (\rho(\vec{u} \otimes \vec{u}) + \Pi) - \rho \, g_z \tag{2.3.35}$$

$$\frac{\partial(\rho E)}{\partial t} = -\nabla \cdot (\vec{u}(\rho E + P) - \kappa_T \, \rho \, c_P \, \nabla T - \nabla(\pi \vec{u})) - \rho \vec{u} \, g_z \tag{2.3.36}$$

$$P = \frac{\mathcal{R} \rho T}{\mu(c_i)} \tag{2.3.37}$$

[5] priv. comm. Dirk Olbers

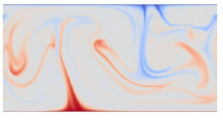

2.4 Boussinesq approximation

This section follows the derivation presented in Lesieur [28]. A classical and excellent work on the Boussinesq approximation is by Spiegel & Veronis [43].

The Boussinesq approximation is an abridgment of the compressible Navier-Stokes equations. As long as density and pressure variations are small compared to the background hydrostatic state the low Mach limit assumption can be applied. Starting from a general approach with density stratification ($\rho = \rho(\vec{x}, t)$), we will end up in one of the most restrictive forms of the incompressible fluid equations with constant density ($\rho = \rho_0$). The main advantage in modelling incompressible fluids compared to compressible fluids is the 'loss' of sound waves. Density fluctuations produce sound waves, which have to be resolved numerically. In consequence the time steps are limited by these waves and therefore the computational effort rises. Simulation codes which use incompressible fluid equations are usually restricted by the fluid velocity only and can therefore use bigger time steps than compressible codes. Unfortunately, the loss of the explicit density equation leads typically to a Poisson equation for the pressure as a constraint, which thwarts the efficiency dramatically.

The main concept behind the Boussinesq approximation is that density variations are only taken into account in the buoyancy term of the vertical velocity equation. The second assumption is the well known incompressibility constraint, which represents a solenoidal velocity field,

$$\frac{D\,\rho}{D\,t} = 0 \tag{2.4.1}$$

where the substantial derivative[6] for a scalar field $\xi = \xi(\vec{x}, t)$ is defined as,

$$\frac{D\xi}{Dt} = \frac{\partial \xi}{\partial t} + \vec{u} \cdot (\nabla \xi) \tag{2.4.2}$$

We assume the density to be constant, $\rho(\vec{x}, t) = \rho_0$. A more restrictive formulation of the incompressibility equation (2.4.1) becomes,

$$\nabla \cdot \vec{u} = 0 \tag{2.4.3}$$

We start splitting the basic variables (resp. f) into the hydrostatic background state $\bar{f}$ and the variation f' around this value. The primary assumption of the Boussinesq approximation is the roughly vanishing variation in density, pressure, and temperature around the background state.

$$|f'| \ll \bar{f} \tag{2.4.4}$$

[6] this derivative is identical to following expressions: convective derivative, advective derivative, substantive derivative, substantial derivative, Lagrangian derivative, Stokes derivative, particle derivative, hydrodynamic derivative, derivative following the motion, total derivative

$$\rho(\vec{x},t) = \bar{\rho}(\vec{x}) + \rho'(\vec{x},t) \tag{2.4.5}$$
$$P(\vec{x},t) = \bar{P}(\vec{x}) + P'(\vec{x},t) \tag{2.4.6}$$
$$T(\vec{x},t) = \bar{T}(\vec{x}) + T'(\vec{x},t) \tag{2.4.7}$$
$$S(\vec{x},t) = \bar{S}(\vec{x}) + S'(\vec{x},t) \tag{2.4.8}$$
$$\Theta(\vec{x},t) = \bar{\Theta}(\vec{x}) + \Theta'(\vec{x},t) \tag{2.4.9}$$

The potential temperature can be calculated via,

$$\Theta = T(\frac{P_0}{P})^{\frac{\gamma-1}{\gamma}} \tag{2.4.10}$$

and represents an 'adiabatically'-filtered temperature. See section 2.5.1 for a detailed description of the potential temperature.

2.4.1 Velocity equation in Boussinesq approximation

The fluid velocity equation in Boussinesq approximation is derived directly from the compressible Navier-Stokes equations.

$$\frac{\partial(\rho\vec{u})}{\partial t} + \nabla\cdot[\rho(\vec{u}\otimes\vec{u})] + \nabla\cdot\Pi = -\rho\, g_z \tag{2.4.11}$$

Applying (2.4.1) leads to the incompressible velocity equation. The stress tensor changes accordingly (2.3.14).

$$\frac{D\vec{u}}{Dt} = -\frac{1}{\rho}\nabla P + g_z + \nabla\cdot(\nu\nabla\vec{u}) \tag{2.4.12}$$

In the following ν is considered to be constant, $\nu = const.$ Furthermore the equation for the hydrostatic equilibrium and its first order expansion is needed

$$-\nabla P = \rho g_z \tag{2.4.13}$$
$$-\nabla\bar{P} - \nabla P' = \bar{\rho}g_z + \rho' g_z \qquad \Big/ : \bar{\rho} \tag{2.4.14}$$
$$-\frac{1}{\bar{\rho}}\nabla\bar{P} - \frac{1}{\bar{\rho}}\nabla P' = g_z + \frac{\rho'}{\bar{\rho}}g_z \tag{2.4.15}$$

In case of a fluid at rest, the density and pressure fluctuations are vanishing, and therefore:

$$-\frac{1}{\bar{\rho}}\nabla\bar{P} = g_z \tag{2.4.16}$$

Using these relations for the background distribution, the fluctuations (in case of motion) can be expressed as:

$$-\frac{1}{\bar{\rho}}\nabla P' = \frac{\rho'}{\bar{\rho}}g_z \tag{2.4.17}$$

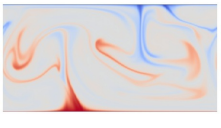

consequently

$$\frac{D\vec{u}}{Dt} = -\frac{1}{\bar{\rho}}\nabla P' + \nu\nabla^2\vec{u} + \frac{\rho'}{\bar{\rho}}g_z \tag{2.4.18}$$

In the case of small scale heights, H (thickness of layer) << D (total depth of fluid), we can set

$$\bar{\rho} \approx \rho_0 \tag{2.4.19}$$

while $\rho_0 = const.$ In the following ρ_0, P_0, T_0, S_0 are reference values at on fixed, but arbitrary position in the domain. Equation (2.4.18) can be rewritten as,

$$\frac{D\vec{u}}{Dt} = -\frac{1}{\rho_0}\nabla P' + \nu\nabla^2\vec{u} + \frac{\rho'}{\rho_0}g_z \tag{2.4.20}$$

An incompressible ideal gas (in contrast to liquids) follows the approximation[7]. This is based in the assumption that the first order expansion of the equation of state leads to $\mathcal{O}(P') \approx \mathcal{O}(T')$ and $\mathcal{O}(P') \approx \mathcal{O}(\rho')$. The second order of this expansion is assumed to be vanishing. Hence, we can use latter expansion approximations to obtain,

$$\frac{T'}{\bar{T}} = \frac{\Theta'}{\bar{\Theta}} = -\frac{\rho'}{\bar{\rho}} \tag{2.4.21}$$

and finally,

$$\frac{D\vec{u}}{Dt} = -\frac{1}{\rho_0}\nabla P' + \nu\nabla^2\vec{u} - \frac{\Theta'}{\Theta_0}\vec{g} \tag{2.4.22}$$

$$\frac{\partial\vec{u}}{\partial t} = -\nabla\cdot(\vec{u}\otimes\vec{u} + \frac{1}{\rho_0}\mathbb{1}P' - \nu\nabla\vec{u}) - \frac{\Theta'}{\Theta_0}g_z \tag{2.4.23}$$

The extension for an additional salinity field takes the form, [43]

$$\frac{\partial\vec{u}}{\partial t} = -\nabla\cdot(\vec{u}\otimes\vec{u} + \frac{1}{\rho_0}\mathbb{1}P' - \nu\nabla\vec{u}) - (\frac{\Theta'}{\Theta_0} - \frac{S'}{S_0})g_z \tag{2.4.24}$$

2.4.2 Energy equation in Boussinesq approximation

We start with the conserved total energy equation (2.3.32),

$$\frac{\partial(\rho E)}{\partial t} + \nabla\cdot[\vec{u}(\rho E + P)] + \nabla\cdot(-K_h\nabla T) - \nabla\cdot(\pi\vec{u}) = -\vec{p}\,g_z \tag{2.4.25}$$

A couple of assumptions has to be applied when changing from the compressible regime to the incompressible one. Firstly, the viscous forces can be ignored by assuming that the fluid velocities are small ($Ma^2 \to 0$).[8] Thus, $\nabla\cdot(\pi\vec{u}) \approx 0$ and $\rho E \approx \rho e$. The pressure term vanishes by applying the incompressibility constraint

[7] cf. [28] §2.9
[8] cf. [28] p15 (2.42)

and the hydrostatic equilibrium equation.

$$-\nabla \cdot (\vec{u}P) + \vec{u}\rho g_z = 0 \Leftrightarrow \tag{2.4.26}$$

$$-P\nabla \cdot \vec{u} - \vec{u}\nabla P = \rho \vec{u} g_z \Leftrightarrow \tag{2.4.27}$$

$$-\nabla P = \rho g_z \tag{2.4.28}$$

Equation (2.4.25) takes the form,

$$\frac{\partial \rho e}{\partial t} + \nabla \cdot (\rho \vec{u} e) + P\nabla \cdot \vec{u} = K_h \nabla^2 T, \tag{2.4.29}$$

where is set constant here and in all subsequent equations, $K_h = const.$ Again we apply the incompressibility constraint (2.4.1). Equation (2.4.29) reduces to an internal energy equation,

$$\frac{\partial \rho e}{\partial t} + \underbrace{\rho e \nabla \cdot \vec{u}}_{=0} + \vec{u} \cdot \nabla(\rho e) + \underbrace{P\nabla \cdot \vec{u}}_{=0} = K_h \nabla^2 T \tag{2.4.30}$$

and consequently,

$$\frac{\partial \rho e}{\partial t} + \vec{u} \cdot \nabla(\rho e) = K_h \nabla^2 T \tag{2.4.31}$$

The thermodynamic transition from a compressible to an incompressible fluid is not trivial. In case of an ideal gas the internal energy e is set to,

$$e = c_V T \tag{2.4.32}$$

But the 'classical' temperature equation has c_P as coefficient,

$$\rho c_P \frac{DT}{Dt} = K_h \nabla^2 T, \tag{2.4.33}$$

and this formulation can not be derived directly from assumption (2.4.32), which has c_V as coefficient. One might set c_P and c_V equal, but this is in contradiction to the ideal gas relation $c_P - c_V = \mathcal{R}$. Consequently, we have a paradox, which is named 'energy equation paradox'.

'The paradox is explained by noting that when temperature differences are vanishing, the convection and conduction terms are just as small as the term containing $\nabla \cdot \vec{u}$. Thus all three terms are important. A slight rearrangement of the $\nabla \cdot \vec{u}$ term using the continuity and state relations allows that term to be combined with the c_V term to produce the correct term, where c_P is the coefficient of the substantial derivative.'[9] This rearrangement is based on a non-dimensional formulation of the general energy equation. Under the assumption that $Ma^2 \to 0$ the dissipation term is removed. The second limit process is that for small temperature differences the temperature

[9] private communication Prof. Ron Panton.

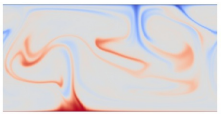

fluctuations vanish, $\Delta T/T_0 \to 0$. We combine these limitations and the coefficient becomes,

$$c_V + \frac{T}{\rho}\frac{\beta^2}{\alpha} \tag{2.4.34}$$

where,

$$\frac{\beta}{\alpha} = \Big(\frac{\partial p}{\partial T}\Big)_\rho \tag{2.4.35}$$

From thermodynamic theory we have the relation (see [14] p127)

$$c_P = c_V + \frac{T}{\rho}\frac{\beta^2}{\alpha} \tag{2.4.36}$$

Hence the temperature equation takes the form

$$\rho c_P \frac{\partial T}{\partial t} + \rho c_P \vec{u}\cdot\nabla T = K_h \nabla^2 T \tag{2.4.37}$$

or the better known form

$$\frac{DT}{Dt} = \kappa_T \nabla^2 T \tag{2.4.38}$$

and $\kappa_T = \frac{K_h}{c_p \rho}$ is the thermal diffusivity. With the definition for the potential temperature (2.4.10) the latter equation becomes,

$$\frac{T}{\Theta}\frac{D\Theta}{Dt} = \kappa_T \nabla^2 T, \tag{2.4.39}$$

where the thermal diffusion coefficient κ_T is constant due to constant density. The previous equation is the starting point for the actual Boussinesq approximation.Again,

$$P(\vec{x},t) = \bar{P}(\vec{x}) + P'(\vec{x},t) \tag{2.4.40}$$

$$T(\vec{x},t) = \bar{T}(\vec{x}) + T'(\vec{x},t) \tag{2.4.41}$$

$$\Theta(\vec{x},t) = \bar{\Theta}(\vec{x}) + \Theta'(\vec{x},t) \tag{2.4.42}$$

$$\frac{D\Theta}{Dt} = \frac{\Theta}{T}\kappa_T \nabla^2 T = \frac{\Theta}{T}\kappa_T(\nabla^2 \bar{T} + \nabla^2 T') \tag{2.4.43}$$

Two assumptions are made: $\mathcal{O}(\Theta) = \mathcal{O}(T)$ and $\nabla^2 \bar{T} \approx 0$

$$\frac{D\Theta}{Dt} = \kappa_T \nabla^2 T' \tag{2.4.44}$$

Furthermore an ideal gas (in contrast to a liquid) fulfills, $\frac{T'}{\bar{T}} = \frac{\Theta'}{\bar{\Theta}} = -\frac{\rho'}{\bar{\rho}}$. We assume that $\Theta' = T'$ since $\Theta_0 = T_0$

$$\frac{D\Theta}{Dt} = \kappa_T \nabla^2 \Theta' \tag{2.4.45}$$

$$\frac{D\Theta}{Dt} = \frac{D\bar{\Theta}}{Dt} + \frac{D\Theta'}{Dt} = \frac{\partial\bar{\Theta}}{\partial t} + \vec{u}\cdot\nabla\bar{\Theta} + \frac{D\Theta'}{Dt} \tag{2.4.46}$$

The approximation $\frac{\partial\bar{\Theta}}{\partial t} = 0$ is applied, which means that the potential temperature background distribution is temporal constant.

$$\frac{D\Theta'}{Dt} + \vec{u}\cdot\nabla\bar{\Theta} = \kappa_T\nabla^2\Theta' \tag{2.4.47}$$

$$\frac{\partial\Theta'}{\partial t} + \vec{u}\cdot\nabla\Theta' + \vec{u}\cdot\nabla\bar{\Theta} = \kappa_T\nabla^2\Theta' \tag{2.4.48}$$

using $\nabla\cdot(\vec{u}(\bar{\Theta}+\Theta')) = (\bar{\Theta}+\Theta')\nabla\cdot\vec{u} + \vec{u}\cdot\nabla(\bar{\Theta}+\Theta')$ and the incompressibility constraint leads to the final equation

$$\frac{\partial\Theta'}{\partial t} = -\nabla\cdot(\vec{u}(\bar{\Theta}+\Theta') - \kappa_T\nabla\Theta') \tag{2.4.49}$$

2.4.3 Salinity concentration equation in Boussinesq approximation

The salinity concentration equation has already been derived (cf. (2.3.11)). We apply the incompressibility constraint and become,

$$\frac{DS}{Dt} = \kappa_S\nabla^2 S \tag{2.4.50}$$

where κ_S is the saline concentration diffusion coefficient. Furthermore the Boussinesq assumption (2.4.4) has to be valid. Now we use the same arguments as for the temperature equation and the saline equation obtain,

$$\frac{\partial S'}{\partial t} = -\nabla\cdot(\vec{u}(\bar{S}+S') - \kappa_S\nabla S'), \tag{2.4.51}$$

where the saline diffusion coefficient κ_S is constant.

2.4.4 Set of incompressible binary mixture equations

$$\nabla\cdot\vec{u} = 0 \tag{2.4.52}$$

$$\frac{\partial\vec{u}}{\partial t} = -\nabla\cdot(\vec{u}\otimes\vec{u} + \frac{1}{\rho_0}\mathbb{1}P' - \nu\nabla\vec{u}) - (\frac{\Theta'}{\Theta_0} - \frac{S'}{S_0})g_z \tag{2.4.53}$$

$$\frac{\partial\Theta'}{\partial t} = -\nabla\cdot(\vec{u}(\bar{\Theta}+\Theta') - \kappa_T\nabla\Theta') \tag{2.4.54}$$

$$\frac{\partial S'}{\partial t} = -\nabla\cdot(\vec{u}(\bar{S}+S') - \kappa_S\nabla S') \tag{2.4.55}$$

The incompressibility constraint gets realised by a replaced pressure evolution equation in terms of a Poisson equation. This Poisson equation is derived in the next

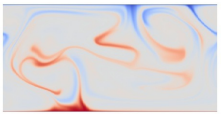

chapter.

Equation of state for saltwater

The realistic water equations differ in that way that the density ρ is not constant and depends on the salinity, the temperature and the pressure. The equation for $\rho = \rho(S, T(°\mathrm{C}), P(atm))$, which is used for saltwater, is obtained stepwise. In the first step a polynomial in the temperature T and vanishing salinity $S = 0$ is assumed,

$$\begin{aligned} \rho_W = 999.842594 + 6.793952 \times 10^{-2} T - \\ -9.095290 \times 10^{-3} T^2 + 1.001685 \times 10^{-4} T^3 - \\ -1.120083 \times 10^{-6} T^4 + 6.536332 \times 10^{-9} T^5 \end{aligned} \tag{2.4.56}$$

The dependency on the pressure (one standard atmosphere $P = 0$) is given by,

$$\begin{aligned} \rho(S, T, 0) = \rho_W + S(0.824493 - \\ -4.0899 \times 10^{-3} T + 7.6438 \times 10^{-5} T^2 - \\ -8.2467 \times 10^{-7} T^3 + 5.3875 \times 10^{-9} T^4) + \\ +S^{3/2}(-5.72466 \times 10^{-3} + 1.0227 \times 10^{-4} T - \\ -1.6546 \times 10^{-6} T^2) + 4.8314 \times 10^{-4} S^2 \end{aligned} \tag{2.4.57}$$

The density at pressure P is given by,

$$\rho(S, T, P) = \rho(S, T, 0)\Big(1 - \frac{P}{K(S, T, P)}\Big)^{-1} \tag{2.4.58}$$

where K is the secant bulk modulus which can be expressed in terms of a polynomial of S, T and P. Examples: $\rho(0, 5, 0) = 999.96675 kg/m^3$, $\rho(35, 5, 0) = 1027,67547 kg/m^3$ and $\rho(35, 25, 1000) = 1062,53817 kg/m^3$.

2.5 Methods to compare compressible and incompressible models

The quantities of compressible fluids, e.g. ideal gas, are determined by the laws of thermodynamics and in the following the ideal gas law (2.2.1). The mathematical handling of incompressible fluids is typically based on constraints, which are not directly conforming to an equation of state. This means that it is not obvious how to compare both regimes. For instance, the quantity 'temperature' of an ideal gas is proportional to the mean kinetic energy, but independent of the potential energy. This potential energy contrast has to be taken into account, when comparing both regimes. Later considerations result in using the *potential temperature*.

2.5.1 Temperature T and potential temperature Θ

The potential temperature Θ is the temperature T_0 of an fluid particle when this particle is moved only by an adiabatic process ($dS = 0$) to a reference pressure P_0. It is used to compare temperature parcels of different heights. To derive a translation between the 'real' temperature T and the potential temperature Θ it is important that the fluid (ideal gas) is in hydrostatic equilibrium. There are several approaches to derive the potential temperature. But, in principle, the fluid particle movement is done by integration over a thermally and hydrostatically layered ideal gas column to a reference temperature T_0 and to a reference pressure P_0.

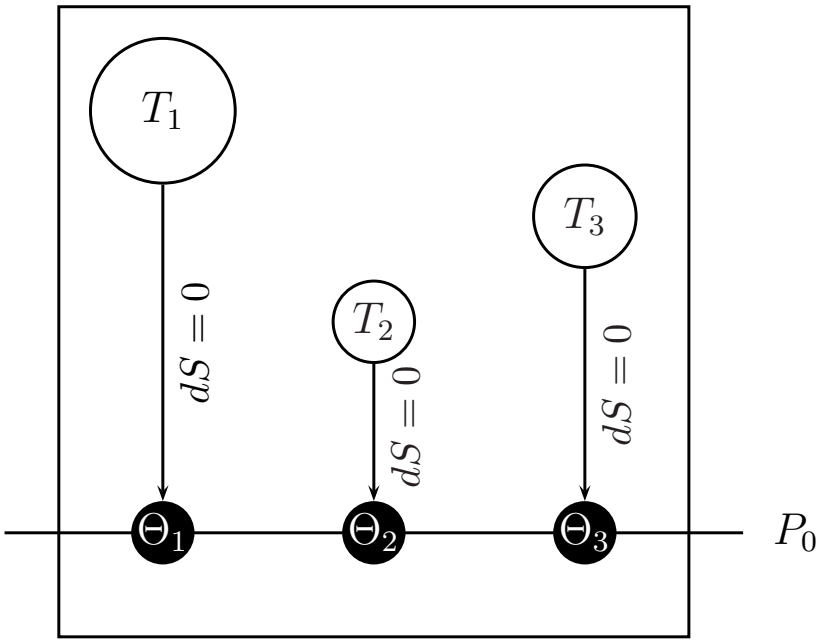

Figure 2.2: Potential temperature for three different fluid parcels

We have,

$$\frac{\partial T}{\partial z} = -\frac{g_z}{c_P} \tag{2.5.1}$$

$$\frac{\partial P}{\partial z} = -\rho \vec{g}_z \tag{2.5.2}$$

It follows,

$$\frac{\partial P}{\partial z} = \frac{P\mu}{\mathcal{R}T} \cdot \frac{\partial T}{\partial z} c_P \tag{2.5.3}$$

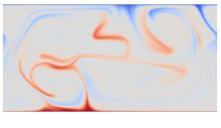

Rearranging leads to,

$$\frac{1}{T}\frac{\partial T}{\partial z} = \frac{\mathcal{R}}{c_P \mu} \cdot \frac{1}{P}\frac{\partial P}{\partial z} \qquad \Big/ \int_T^{T_0}\int_P^{P_0} dz \tag{2.5.4}$$

$$\ln \frac{T_0}{T} = \frac{\mathcal{R}}{c_P \mu} \ln\left(\frac{P_0}{P}\right) \qquad \Big/ e \tag{2.5.5}$$

$$\frac{T_0}{T} = \left(\frac{P_0}{P}\right)^{\frac{\mathcal{R}}{c_P \mu}} \tag{2.5.6}$$

The reference temperature T_0 can be chosen arbitrarily, $T_0 = \Theta$, which leads to,

$$\Theta = T\left(\frac{P_0}{P}\right)^{\frac{\mathcal{R}}{c_P \mu}} \tag{2.5.7}$$

using relations (2.2.2)-(2.2.5) gives,

$$\Theta = T\left(\frac{P_0}{P}\right)^{\nabla_{\mathrm{ad}}} \tag{2.5.8}$$

Corollary 2.5.1. *Suppose the fluid is an ideal gas. Then the superadiabatic gradient is equal to the logarithmic potential temperature gradient.*

$$\nabla_\Theta = \nabla - \nabla_{\mathrm{ad}} \tag{2.5.9}$$

Proof. Using (2.5.8) leads to,

$$\ln \Theta = \ln T + \nabla_{\mathrm{ad}} \ln(\frac{P_0}{P}) = \ln T - \nabla_{\mathrm{ad}} \ln P + \underbrace{\nabla_{\mathrm{ad}} \ln P_0}_{\text{const}} \tag{2.5.10}$$

Differentiating both sides,

$$\partial \ln \Theta = \partial \ln T - \nabla_{\mathrm{ad}} \partial \ln P \tag{2.5.11}$$

$$\frac{\partial \ln \Theta}{\partial \ln P} = \frac{\partial \ln T}{\partial \ln P} - \nabla_{\mathrm{ad}} \tag{2.5.12}$$

$$\frac{\partial \ln \Theta}{\partial \ln P} = \nabla - \nabla_{\mathrm{ad}} \tag{2.5.13}$$

$$\nabla_\Theta = \nabla - \nabla_{\mathrm{ad}} \tag{2.5.14}$$

□

It makes sense to define Θ and ∇_Θ, because the potential temperature and its gradient are one of the few thermodynamic quantities which can be used to compare compressible and incompressible fluids.

2.5.2 Thermal Nusselt number

The thermal Nusselt number compares the *total heat flux* with the *conductive heat flux* and gives therefore information about the efficiency of convective mixing. It is defined as,

$$Nu_T = \frac{F_{\text{tot}} - F_{\text{ad}}}{F_{\text{cT}} - F_{\text{ad}}} \tag{2.5.15}$$

where F_{tot} is the total heat flux, F_{ad} the heat flux which would be transported by conduction (and radiation) if the temperature profile would be adiabatic throughout and F_{cT} the flux that would be transported if the temperature profile were linear between the bottom and the top[10]. The diffusive heat flux is defined as: $F_T = -K_h \nabla T$. We obtain K_h from: $K_h = c_P \rho \kappa_T$. The adiabatic heat flux F_{ad} has to be separated from the total heat flux F_{tot}, to measure its contribution. We use the thermodynamic relations (2.2.1)-(2.2.5):

$$\nabla T = \frac{\partial T}{\partial z} = \frac{T}{H_P} \nabla \tag{2.5.16}$$

and it follows

$$F_{\text{tot}} = c_P \rho \kappa_T \nabla T = \frac{P}{H_P} \frac{\nabla}{\nabla_{\text{ad}}} \kappa_T \tag{2.5.17}$$

where the total heat flux is considered to be $F_{\text{tot}} = F_T$. We assume constant entropy, which is equivalent to $\nabla = \nabla_{ad}$. The adiabatic heat flux takes the form

$$F_{\text{ad}} = \frac{P}{H_P} \kappa_T \tag{2.5.18}$$

The fixed thermal boundary conditions, $\Delta T = T_0 - T_1$, lead to[11],

$$Nu_T = \frac{K_h \nabla T - \frac{P}{H_P} \kappa_T}{K_h \frac{\Delta T}{D} - \frac{P}{H_P} \kappa_T} \tag{2.5.19}$$

The thermal Nusselt number takes a different formulation for incompressible fluids. Under the assumption that the pressure scale height becomes very large $H_P \gg 1$, which is valid in incompressible fluids, the adiabatic flux decreases rapidly. This leads to,

$$Nu_T = \frac{\nabla T}{\frac{\Delta T}{H}} \tag{2.5.20}$$

where H is the height of the fluid column. Example: If $Nu_T = 1$ the system is fully conductive and diffusion processes dominate. On the other side, if $Nu_T = 5$, then $F_{\text{conv}} : F_{\text{cond}} \approx 5$, which means, that the total heat flux F_{tot} splits into 80% F_{conv} and 20% F_{cond}.

[10] cf. [31], p323
[11] see [31] for a detailed discussion

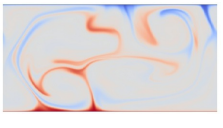

2.5.3 Saline Nusselt number

The saline Nusselt number Nu_S compares the measured saline flux F_S to the saline flux (F_{cS}) that would be transported if the concentration profile were linear between the bottom and the top.

$$Nu_S = \frac{F_S}{F_{cS}} = \frac{\kappa_S \nabla S}{\kappa_S \frac{\Delta S}{H}} = \frac{\nabla S}{\frac{\Delta S}{H}} \tag{2.5.21}$$

where $\Delta S = S_0 - S_1$. This formulation is valid in compressible and incompressible fluids, because the saline flux is not affected by the adiabatic layering.

2.5.4 Effective diffusion coefficients

There exists a strong correlation between these two dimensionless numbers (see [23] eq. 5.2).

$$Nu_S = \frac{Nu_T}{\sqrt{Le}} \tag{2.5.22}$$

With the knowledge of Nu_T and Nu_S it is possible to calculate the effective diffusion coefficients $(\kappa_T)_{eff}$ and $(\kappa_S)_{eff}$ and hence the effective transported heat and salt/helium. The resulting diffusive time scales τ_T and τ_S can now be compared to eg. the lifetime of the star or the ocean. This gives information about the salt/helium transport efficiency for global mixing processes. The stellar case was discussed in details by Spruit [44].

$$(\kappa_T)_{\text{eff}} = \kappa_T \, Nu_T \tag{2.5.23}$$

$$(\tau_T)_{\text{eff}} = \frac{H^2}{(\kappa_T)_{\text{eff}}} \tag{2.5.24}$$

$$(\kappa_S)_{\text{eff}} = \kappa_S \, Nu_S \tag{2.5.25}$$

$$(\tau_S)_{\text{eff}} = \frac{H^2}{(\kappa_S)_{\text{eff}}} \tag{2.5.26}$$

Chapter 3

Numerical Methods

3.1 Introduction

In this section the numerical methods for solving the governing equations are presented. All these methods have been implemented into the ANTARES (Advanced Numerical Tool for Astrophysical RESearch) software package, which was developed at the faculty of mathematics at the University of Vienna under the direction of Univ. Prof. H. Muthsam. The differences in solving compressible and incompressible fluid dynamical equations are studied. The reader will see that the numerical treatment of both regimes is not comparable. Especially incompressible fluids need special mathematical handling. While the initial setup is described in details in the first section, we now concentrate on the spatial time derivatives and the time integration, respectively.

3.2 Preliminary

We start defining the type of equation to be solved. Let $D \subseteq \mathbb{R}^d$ and $m \geqslant 1$.

$$\mathbf{U} = \begin{pmatrix} U_1(\vec{x},t) \\ \vdots \\ U_m(\vec{x},t) \end{pmatrix} : [0,\infty) \times D \to \mathbb{R}^m \subseteq \mathbb{R}^d \tag{3.2.1}$$

The components of the vector $\mathbf{U}$ represent densities of conserved variables like density ρ, partial density $c\rho$, momentum $\vec{p}$ or total energy density ρE. More precisely, the components are density functions with the property,

$$\int_D U_i(\vec{x},t) = const. \tag{3.2.2}$$

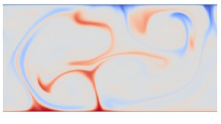

(except for possible boundary terms). A so called *flux function* f is introduced,

$$f_i : \mathbb{R}^m \to \mathbb{R}^m \quad , i = 1, ..., d \tag{3.2.3}$$

$$f_i = \begin{pmatrix} (f_i)_1 \\ \vdots \\ (f_i)_m \end{pmatrix} \tag{3.2.4}$$

A time-dependent system of partial differential equations with the structure,

$$\mathbf{U}_t + \sum_i \partial_i f_i(\mathbf{U}) = 0 \tag{3.2.5}$$

is called *law of conservation*. An imprecise, but more readable form of (3.2.5) is,

$$\mathbf{U}_t + \nabla \cdot f(\mathbf{U}) = 0 \tag{3.2.6}$$

Without loss of generality equation (3.2.5) is reduced to three dimensions and linearized,

$$\mathbf{U}_t + \mathbf{J}_1 \frac{\partial \mathbf{U}}{\partial x} + \mathbf{J}_2 \frac{\partial \mathbf{U}}{\partial y} + \mathbf{J}_3 \frac{\partial \mathbf{U}}{\partial z} = 0 \tag{3.2.7}$$

The matrix $\mathbf{J}_i = \frac{\partial f_i(k)}{\partial k}$ $(i = 1, 2, 3)$ is called Jacobian or functional matrix. In case of a compressible fluid the conserved variables are: $\mathbf{U} = (\rho, \rho c, \rho \vec{u}, \rho E)^T$. The variables $\rho, \rho c, \rho \vec{u}, \rho E$ represent real physically conserved quantities. The variables used for the incompressible formulation of the problem are only conserved under the incompressibility assumption. Hence, the vector $\mathbf{U}$ takes the form $\mathbf{U} = (S, \Theta, \vec{u})^T$. The velocity vector $\vec{u}$ takes the form $\vec{u} = (u, v, w)^T$

Definition 3.2.1. *'A system* $\mathbf{U}_t + \sum_{i=1}^m \partial_i f_i(\mathbf{U}) = 0$ *is said to be* ***hyperbolic*** *at a point* $(\vec{x}, t)$ *if the Jacobian matrix has m real eigenvalues and a corresponding set of m linearly independent right eigenvectors. The system is said to be strictly hyperbolic, if the eigenvalues are all distinct.'* [1]

Depending on the rank of the Jacobian matrices, the system can be solved with the characteristics method or with classical direct approaches.

Advantage of using characteristic variables:

The advantage of solving hyperbolic equations (one might think about the Euler equations) in characteristic variables is the fact that the real physical behavior of an equation can be captured more precisely. Transforming the equations into their corresponding uncoupled eigensystem gives the possibility to solve them along their characteristics. Additional information like the eigenvalues of the system help to

[1] cf. [46] p45

implement up-winding schemes, which capture shocks and discontinuities along the characteristics in a much better way, than classical numerical approaches. This makes sense, if shocks or other discontinuities are expected. Here, the eigenvalues represent the speed of information along characteristics. In low Mach number flows, which are modelled in the anelastic approximation or the Boussinesq approximation, the transformation to characteristic variables is mostly not possible due to its non-strict hyperbolic or even parabolic character. This leads to different numerical algorithms. The underlying (W)ENO scheme is independent of the equation and can be used as long as fluid velocities are high enough. Upwind schemes fail in the low Mach number limit. See section 4.3.3 for more details.

Initial conditions as well as boundary conditions need to be augmented to the system (3.2.5) to formulate a well defined problem on a specified bounded spatial domain D. From a mathematical point of view, the boundary is not part of the domain. This seems to be obvious, but there are several pitfalls in this context. For instance, the incompressibility constraint, which has to be fulfilled in the domain, can hardly be combined with realistic physical boundary conditions, as eg. 'slip conditions'. Therefore the constraint is usually not valid at the boundary.

(W)ENO and the Boussinesq approximation

The two dimensional Boussinesq equations have multiple eigenvalues $(u, u, u, u)^T$ which does not allow to transform them into the eigenspace, because of identical eigenvectors and hence a singular eigenvector matrix. This means that the characteristic fields contributing the characteristic subspace have the same upwind direction, since their characteristic speeds are identical. 'Since the characteristic subspace has a well-defined upwind direction, upwind differencing is possible without decomposition of the characteristic subspace further into the individual scalar fluxes. Instead we can directly apply upwind interpolation to the cell center values of the flux vector.' [2]

3.3 ANTARES code

A requested physical state $\mathbf{U}^{n+1}$ at time level $n+1$ is calculated with a Runge-Kutta scheme from $\mathbf{U}^n$ at time level n. The initial state is denoted with $\mathbf{U}^0$. In the following the calculation from n to $n+1$ is called *step*, while each intermediate Runge-Kutta level is called *stage*. The ANTARES code performs the following algorithm to calculate each stage and repeats it according to the Runge-Kutta order. Two cases have to be distinguished:

Compressible fluid equations:

[2] [13] p24

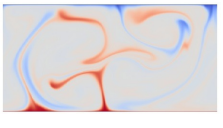

time	inviscid	viscous	source
$\partial_t \rho =$	$-\nabla \cdot (\rho \vec{u})$		
$\partial_t (\rho c) =$	$-\nabla \cdot (c \rho \vec{u})$	$+\nabla \cdot (\rho \kappa_c \nabla c)$	
$\partial_t (\rho \vec{u}) =$	$-\nabla \cdot (\rho \vec{u} \otimes \vec{u} + P)$	$+\nabla \cdot \pi$	$-\rho \vec{g}_z$
$\partial_t (\rho E) =$	$-\nabla \cdot (\vec{u}(\rho E + P))$	$+\nabla \cdot (\pi \vec{u}) + \nabla \cdot (K_h \nabla T)$	$-\rho \vec{u} \vec{g}_z$

These equations are solved with the following algorithm:

1. $\mathbf{U}^n$ is given as cell average values.
2. Calculation of inviscid cell boundary fluxes using a 5th order WENO-scheme.
3. Calculation of viscid cell boundary fluxes by a 4th order interpolation.
4. Summation of the inviscid and the viscid boundary fluxes.
5. Determination of the physical state values $\mathbf{U}^{n+1}$ (in case of Runge-Kutta first order) or $\mathbf{U}^{n+1/2}$ (in case of Runge-Kutta second order).
6. Application of boundary conditions.
7. Determination of other physical quantities with an equation of state .
8. stage = stage + 1(in case of Runge-Kutta second order).
9. goto 1 (in case of Runge-Kutta second order).
10. step = step + 1

Incompressible fluid equations:

time	inviscid	viscous	source
$0 =$	$-\nabla \cdot \vec{u}$		
$\partial_t (S) =$	$-\nabla \cdot (S \vec{u})$	$+\nabla \cdot (\kappa_S \nabla S)$	
$\partial_t (\vec{u}) =$	$-\nabla \cdot (\vec{u} \otimes \vec{u})$	$+\nabla \cdot \pi$	$-(\frac{\Theta'}{\Theta_0} - \frac{S'}{S_0}) \vec{g}_z$
$\partial_t (\Theta) =$	$-\nabla \cdot (\Theta \vec{u})$	$+\nabla \cdot (\kappa_T \nabla \Theta)$	

These equations are solved with the following algorithm.

1. $\mathbf{U}^n$ is given as cell average values.
2. Calculation of inviscid cell boundary fluxes using a 5th order MachENO-scheme.
3. Calculation of viscid cell boundary fluxes by a 4th order interpolation.
4. Summation of the inviscid and the viscid boundary fluxes.
5. Determination of the intermediate physical state values $\mathbf{U}^*$.
6. Application of intermediate boundary conditions.

7. Form a pressure Poisson equation according to the incompressibility constraint, which updated the intermediate velocity values.
8. Update of the intermediate physical state quantities to $\mathbf{U}^{n+1}$ (in case of Runge-Kutta first order) or $\mathbf{U}^{n+1/2}$ (in case of Runge-Kutta second order).
9. Application of boundary conditions.
10. Determination of other physical quantities with an equation of state.
11. stage = stage + 1 (in case of Runge-Kutta second order).
12. goto 1 (in case of Runge-Kutta second order).
13. step = step + 1

MPI© and OpenMP©

A comprehensive discussion of the ANTARES code can be found in Muthsam et al [36]. In addition to MPI©, an OpenMP© parallelisation was applied, to ensure maximum utilisation of the available computational environment. The OpenMP© framework works efficiently with multicore CPU's (Core2Duo©, BlueGene©,...) and gears to use their shared memory. Due to the fact that most supercomputing facilities tend to shared memory architectures, hybrid implemented hydro-codes become more and more attractive. All calculations have been done at the RZG (Rechenzentrum der Max-Planck Gesellschaft Garching) on an IBM Power6 system called 'VIP' and an IBM Power5 system. Performance tests up to 1024 PE's have been done, but usually the 2D simulations are calculated on 1–32 PE's. The hybrid OpenMP© extension was implemented for the radiative transfer equation, (W)ENO and EOS. In case of the radiative transfer equation, which consumes up to 80% of the computational time of e.g. solar surface flow simulations the hybrid parallelisation was very efficient. As the semiconvection simulations doe not solve the radiative transfer equation, this aspect is not relevant for the presented work. The (W)ENO and EOS could not benefit from OpenMP©.

3.4 Numerical method for solving the compressible fluid equations

Transformation of inviscid terms into eigensystem We now present the algorithm to calculate the inviscid fluxes at the new time step $n+1$ for the binary mixture equations. In contrast to the Euler equations the additional concentration equation and the different EOS lead to a more complicated eigensystem. However, the base change matrices can be calculated explicitly, which is an enormous advantage. For reasons of simplicity the following derivations are done in 1D. An extension

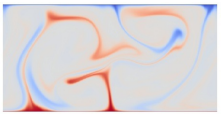

to higher dimensions is done similarly. The transformation of equation (2.3.37) into the eigensystem requires the knowledge of the corresponding linearized system,

$$\mathbf{U}_t + \mathbf{J}\frac{\partial \mathbf{U}}{\partial x} = 0 \tag{3.4.1}$$

Under the assumption that the system is hyperbolic there exists a decomposition in the form,

$$\mathbf{J} = R\Lambda L \tag{3.4.2}$$

where Λ is a diagonal matrix filled with the eigenvalues of $\mathbf{J}$, R is the right eigenvector matrix of $\mathbf{J}$ and $L = R^{-1}$ is the left eigenvector matrix. In our case the inviscid 1D terms of equation (2.3.37) take the form,

$$\begin{pmatrix} \rho \\ \rho c \\ \rho u \\ \rho E \end{pmatrix}_t = - \begin{pmatrix} \rho u \\ c\rho u \\ \rho u \cdot u + P \\ u(\rho E + P) \end{pmatrix}_x \tag{3.4.3}$$

We mention that u is the first component of $\vec{u}$. With this transformation,

$$\mathbf{U}^T = \begin{pmatrix} \rho & \rho c & \rho u & \rho E \end{pmatrix}^T \rightarrow \mathbf{W}^T = \begin{pmatrix} \rho_1 & \rho_2 & p_x & Et \end{pmatrix}^T \tag{3.4.4}$$

where p_x is the first component of $\vec{p}$. Hence, the system takes the form,

$$\begin{pmatrix} \rho_1 \\ \rho_2 \\ p_x \\ Et \end{pmatrix}_t = - \begin{pmatrix} p_x \\ \rho_2 \rho_1^{-1} p_x \\ p_x^2 \rho_1^{-1} + P \\ p_x \rho_1^{-1}(Et + P) \end{pmatrix}_x \tag{3.4.5}$$

where the pressure $P = P(\mathbf{W})$. The Jacobian matrix takes the form,

$$J = \begin{pmatrix} 0 & 0 & 1 & 0 \\ -\frac{\rho_2}{\rho_1^2} p_x & \frac{p_x}{\rho_1} & \frac{\rho_2}{\rho_1} & 0 \\ -\frac{p_x^2}{\rho_1^2} + \frac{\partial P}{\partial \rho_1} & \frac{\partial P}{\partial \rho_2} & \frac{2p_x}{\rho_1} + \frac{\partial P}{\partial p_x} & \frac{\partial P}{\partial Et} \\ -\frac{p_x}{\rho_1^2}(Et + P) + \frac{p_x}{\rho_1}(Et + \frac{\partial P}{\partial \rho_1}) & \frac{p_x}{\rho_1}\frac{\partial P}{\partial \rho_2} & \frac{1}{\rho_1}(Et + P) + \frac{p_x}{\rho_1}(Et + \frac{\partial P}{\partial p_x}) & \frac{p_x}{\rho_1}(1 + \frac{\partial P}{\partial Et}) \end{pmatrix} \tag{3.4.6}$$

The corresponding eigenvalues for the matrix Λ are,

$$\begin{pmatrix} \frac{p_x}{\rho_1} + \sqrt{\frac{\partial P}{\partial \rho_1}}, & \frac{p_x}{\rho_1}, & \frac{p_x}{\rho_1}, & \frac{p_x}{\rho_1} - \sqrt{\frac{\partial P}{\partial \rho_1}} \end{pmatrix}^T \tag{3.4.7}$$

or in the more pleasant form,

$$\begin{pmatrix} u + c_s, & u, & u, & u - c_s \end{pmatrix}^T \tag{3.4.8}$$

with the speed of sound c_s (see equation (3.4.16)). The equation of state takes the mean molecular weight into account, which is a function of the concentration (here Helium concentration Y).

$$P = \frac{R\rho_1 T(\mathbf{W})}{\mu(\mathbf{W})} \tag{3.4.9}$$

The base change matrices R and $L = R^{-1}$ take the form,

$$R = \begin{pmatrix} 1 & 0 & 1 & 1 \\ Y & 1 & 0 & 1 \\ u - c_s & 0 & u & u + c_s \\ (Et + P)\rho_1^{-1} - u\,c_s & -\Phi_1 & \Phi_3 + u^2 & (Et + P)\rho_1^{-1} + c_s u \end{pmatrix} \tag{3.4.10}$$

$$L = \begin{pmatrix} \frac{1}{2}(uc_s^{-1} + \Phi_3\Phi_4) & -\frac{1}{2}\Phi_1\Phi_4 & & \frac{1}{2}(u\Phi_4 - c_s^{-1}) \\ -Y\Phi_3\Phi_4 & 1 + Y\Phi_1\Phi_4 & -Yu\Phi_4 & Y\Phi_4 \\ 1 - \Phi_3\Phi_4 & \Phi_3\Phi_4 & -u\Phi_4 & \Phi_4 \\ \frac{1}{2}(-uc_s^{-1} + \Phi_3\Phi_4) & -\frac{1}{2}\Phi_1\Phi_4 & \frac{1}{2}(u\Phi_4 + c_s^{-1}) & -\frac{1}{2}\Phi_4 \end{pmatrix} \tag{3.4.11}$$

where,

$$\Phi_1 = \frac{\partial P}{\partial Y}\frac{\partial e}{\partial T} - \frac{\partial e}{\partial Y} \tag{3.4.12}$$

$$\Phi_2 = \frac{\partial P}{\partial \rho_1}\frac{\partial e}{\partial T} - \frac{\partial e}{\partial Y} \tag{3.4.13}$$

$$\Phi_3 = Y\Phi_1 - \rho_1\Phi_2 + Et\rho_1^{-1} - u^2 \tag{3.4.14}$$

$$\Phi_4 = -\rho_1(P + \Phi_2\rho^2)^{-1} \tag{3.4.15}$$

$$c_s = \sqrt{\frac{\partial P}{\partial T}(\frac{\partial e}{\partial T})^{-1}(P\rho_1^{-2} + \Phi_2)} \tag{3.4.16}$$

Now it is possible to change into the eigensystem by

$$\mathbf{V} = R^{-1}\mathbf{W} \tag{3.4.17}$$

and solving the uncoupled equations with (W)ENO and an appropriate up-winding scheme.

Numerical treatment of the inviscid terms with (W)ENO

Classical numerical methods solving fluid dynamical equations fail to work when steep gradients, contact discontinuities or shocks occur. Standard discretisations usually lead to oscillations at these locations. Therefore a numerical method needs to be non-oscillatory and has to capture shocks. The ENO (essentially non-oscillatory) method meets both claims. It was developed in the 1980's by Harten [21] and advanced to weighted-ENO (WENO) by Shu & Osher [42]. 'Basically (W)ENO uses interpolation polynomials, which are constructed by using the adaptive stencil

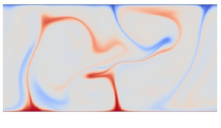

ENO procedure according to which points from the smoothest region of the stencil are chosen'[3]. The explanation of the scheme follows Drikakis [10]. The following algorithm aims to solve only the inviscid parts of the fluid dynamical equations. Viscous parts are calculated separately, which is explained subsequently. Using the 1-dimensional, hyperbolical equation of the form (3.2.5) or one single equation of the uncoupled eigensystem,

$$\mathbf{U}_t + \frac{\partial f(\mathbf{U})}{\partial x} = 0 \tag{3.4.18}$$

the numerical solution of the inviscid parts can be discretized as,

$$\bar{\mathbf{U}}^{n+1} = \bar{\mathbf{U}}^n - \frac{\Delta t}{\Delta x}(\bar{\mathbf{f}}_{i+\frac{1}{2}} - \bar{\mathbf{f}}_{i-\frac{1}{2}}) \tag{3.4.19}$$

where the numerical flux $\bar{\mathbf{f}}$ is constructed via

$$\bar{\mathbf{f}}_{i+\frac{1}{2}} = \bar{\mathbf{f}}_i^+ + \bar{\mathbf{f}}_{i+1}^- = \bar{\mathbf{f}}_{i+\frac{1}{2}}^+ + \bar{\mathbf{f}}_{i+\frac{1}{2}}^- \tag{3.4.20}$$

$$f(U_i) = f^+(U_i) + f^-(U_i) \tag{3.4.21}$$

and $\bar{\mathbf{f}}_i^+$ and $\bar{\mathbf{f}}_{i+1}^-$ correspond to the positive and negative eigenvalues,

$$\frac{\partial f^+}{\partial U_i} \geq 0 \tag{3.4.22}$$

$$\frac{\partial f^-}{\partial U_i} \leq 0 \tag{3.4.23}$$

The numerical fluxes are now developed in a Taylor series expansion,

$$\bar{\mathbf{f}}_{i+\frac{1}{2}} = f_{i+\frac{1}{2}} + \sum_{k=1}^{m-1} a_{2k}\Delta x^{2k}\left(\frac{\partial^{2k} f}{\partial x^{2k}}\right)_{i+\frac{1}{2}} + \mathcal{O}(\Delta x^{2m+1}) \tag{3.4.24}$$

$$\bar{\mathbf{f}}_{i+\frac{1}{2}}^{\pm} = f_{i+\frac{1}{2}}^{\pm} + \sum_{k=1}^{m-1} a_{2k}\Delta x^{2k}\left(\frac{\partial^{2k} f^{\pm}}{\partial x^{2k}}\right)_{i+\frac{1}{2}} + \mathcal{O}(\Delta x^{2m+1}) \tag{3.4.25}$$

Here, the index $2k$ is used instead of k, because of centering. Polynomial interpolants $p_{i+\frac{1}{2}}^{\pm}$ are used for $f^{\pm}$,

$$p_{i+\frac{1}{2}}^{\pm}(x) = f^{\pm}(\mathbf{U}) + \mathcal{O}(\Delta x^{2m+1}) \tag{3.4.26}$$

Finally, the numerical fluxes take the form,

$$\bar{\mathbf{f}}_{i+\frac{1}{2}}^{\pm} = p_{i+\frac{1}{2}}^{\pm} + \sum_{k=1}^{m-1} a_{2k}\Delta x^{2k}\left(\frac{\partial^{2k} p_{i+\frac{1}{2}}^{\pm}}{\partial x^{2k}}\right)_{i+\frac{1}{2}} \tag{3.4.27}$$

The ENO algorithm calculates $p_{i+\frac{1}{2}}^{\pm}$, which choose the points from the smoothest

[3] Drikakis [10] p437

region of the stencil. In contrast to ENO the weighted ENO scheme uses a convex combination of polynomials. A WENO scheme of fifth order was implemented for the simulations presented in this thesis. A brief introduction in calculating the polynomials can be found in the thesis of Obertscheider [38].

Numerical treatment of the viscous terms

Viscous terms are solved on cell centres. Afterwards they are interpolated to the cell faces. Both steps are done with fourth order schemes.

$$\left(\frac{\partial U_j}{\partial x}\right)_i = \frac{1}{12\Delta x}((U_j)_{i-2} - 8(U_j)_{i-1} + 8(U_j)_{i+1} - (U_j)_{i+2}) \tag{3.4.28}$$

where $j = 1, ..., n$. The interpolation from the cell centres to the cell faces is done with the subsequent scheme,

$$\bar{\mathbf{f}}_{i+1/2} = \frac{1}{16}(-\bar{\mathbf{f}}_{i-1} + 9\bar{\mathbf{f}}_i + 9\bar{\mathbf{f}}_i - \bar{\mathbf{f}}_{i+2}) \tag{3.4.29}$$

The viscous terms are calculated accordingly,

$$\frac{1}{\Delta x}(\bar{\mathbf{f}}_{i+1/2} - \bar{\mathbf{f}}_{i-1/2}) \tag{3.4.30}$$

3.5 Numerical method for solving the incompressible fluid equations

The compressible equations can be solved straightly as described in the latter section. Unfortunately, the incompressibility constraint does not allow the same techniques because the type of equation changes dramatically. The solution of the inviscid terms of the incompressible equations follow the (W)ENO scheme, but without solving them along their characteristics. The system is not hyperbolic anymore, thus the base change matrices do not have full rank. It is not obvious how the incompressibility constraint $\nabla \cdot \vec{u} = 0$ can be combined with the other equations. We will see, that the constraint results in a Poisson equation. The numerical method for solving the Boussinesq equations follows a fractional step method, based on a decomposition theorem.

Theorem 3.5.1. (Helmholtz-Hodge Decomposotion Theorem) *A vector field $\boldsymbol{w}$ on D can be uniquely decomposed in the form*

$$\boldsymbol{w} = \boldsymbol{q} + \nabla P, \tag{3.5.1}$$

where $\nabla \cdot \boldsymbol{q} = 0$, $\boldsymbol{q}$ is parallel to ∂D and thus $\boldsymbol{q} \cdot \boldsymbol{n} = 0$ on ∂D.

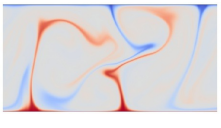

Proof. The proof can be looked up in [8] p37. □

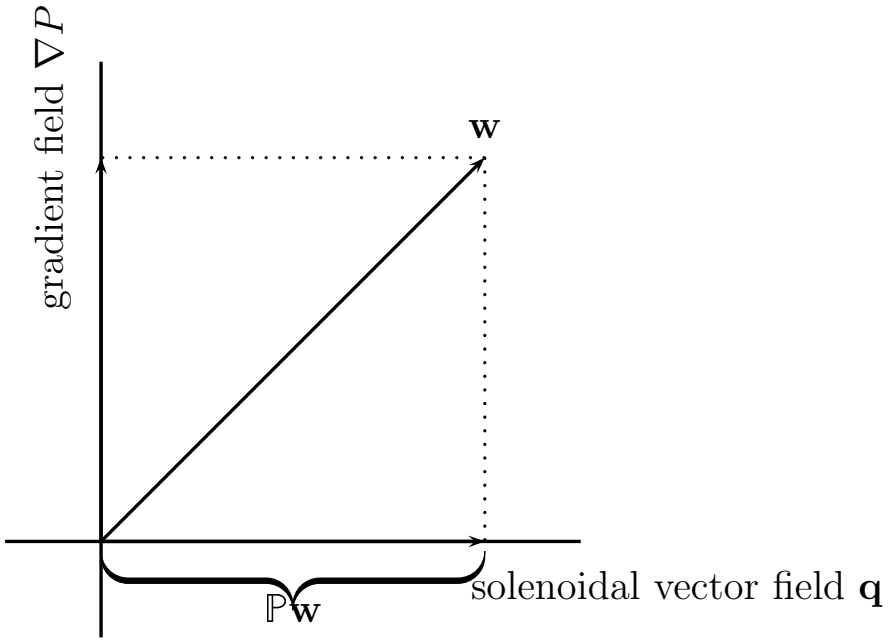

Figure 3.1: Vector field decomposition

A linear operator $\mathbb{P}$ is introduced, which maps $\mathbf{w}$ orthogonally onto its solenoidal part $\mathbf{q}$,

$$\mathbb{P}\mathbf{w} = \mathbb{P}\mathbf{q} + \mathbb{P}(\nabla P) \tag{3.5.2}$$

It follows by definition that

$$\mathbb{P}\mathbf{w} = \mathbf{q} \tag{3.5.3}$$

$$\mathbb{P}\mathbf{q} = \mathbf{q} \tag{3.5.4}$$

$$\mathbb{P}(\nabla P) = 0 \tag{3.5.5}$$

and, if $\mathbf{q}$ is smooth enough,

$$\mathbb{P}\partial_t \mathbf{q} = \partial_t \mathbf{q} \tag{3.5.6}$$

Applying the operator $\mathbb{P}$ to the velocity equation,

$$\mathbb{P}(\frac{\partial \vec{u}}{\partial t} + \frac{1}{\rho_0}\nabla P) = -\mathbb{P}(\nabla \cdot (\vec{u} \otimes \vec{u}) - \nabla \cdot \pi - \rho g_z) \tag{3.5.7}$$

and using relations (3.5.3)-(3.5.6) leads to,

$$\frac{\partial \vec{u}}{\partial t} = -\mathbb{P}(\nabla \cdot (\vec{u} \otimes \vec{u}) - \nabla \cdot \pi) \tag{3.5.8}$$

The pressure is now eliminated and the time derivative $\partial_t \vec{u}$ is expressed in $\vec{u}$ only. This allows us to solve the equation in two steps. Firstly, an intermediate solution $\vec{u}^*$ can be calculated with (3.5.8). The pressure is then recovered by the gradient part of the RHS of the velocity equation,

$$-\nabla \cdot (\vec{u} \otimes \vec{u}) + \nabla \cdot \pi \tag{3.5.9}$$

Usually, a Poisson equation is formed to calculate the pressure P with the intermediate velocity $\vec{u}^*$. Be aware that this 'incompressible pressure' is not a 'physical pressure'. While in a compressible fluid the name 'pressure' is associated with the thermodynamical pressure, the 'incompressible pressure' is independent of an equation of state.. The velocity equation is solved in two steps, which motivates the name 'fractional step approach'.

Numerical fractional step approach for the incompressible velocity equation:

Our starting point is equation (2.4.24), where $\rho^* = \frac{\Theta'}{\Theta_0} - \frac{S'}{S_0}$.

$$\frac{\partial \vec{u}}{\partial t} = -\nabla \cdot (\vec{u} \otimes \vec{u} + \frac{1}{\rho_0} P' - \nu \nabla \vec{u}) - \rho^* g_z \tag{3.5.10}$$

Without loss of generality the density is set constant, $\rho_0 = 1$, and we rewrite the stress tensor in a more familiar form.

$$\frac{\partial \vec{u}}{\partial t} + \nabla \cdot (\vec{u} \otimes \vec{u}) - \nabla \cdot \pi = -\nabla P' - \rho^* g_z \tag{3.5.11}$$

1. step: Advance the velocity to an intermediate solution $\vec{u}^*$ neglecting the contribution of the pressure. However, this does not satisfy the constraint of incompressibility. Solve the salinity and the potential temperature equation. The prediction $\vec{u}^*$ for $\vec{u}^{n+1}$ is obtained by,

$$\frac{\partial \vec{u}}{\partial t} + \nabla \cdot (\vec{u} \otimes \vec{u}) - \nabla \cdot \pi = 0 \tag{3.5.12}$$

2. step: The intermediate velocity $\vec{u}^*$ is split into a solenoidal velocity field $\vec{u}^{n+1}$ and the gradient of a scalar function proportional to the unknown pressure $\nabla P'^{n+1}$. See [40] p180 for a more detailed discussion.

$$\frac{\partial \vec{u}}{\partial t} = -\nabla P' \tag{3.5.13}$$

$$\nabla \cdot \vec{u} = 0 \tag{3.5.14}$$

$$\frac{\vec{u}^{n+1} - \vec{u}^*}{\Delta t} + \nabla P' = 0 \qquad \Big/ \quad \nabla\cdot \tag{3.5.15}$$

$$\nabla \cdot \vec{u}^{n+1} = 0 \tag{3.5.16}$$

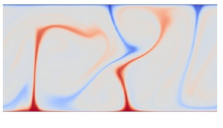

and finally,

$$\nabla \cdot \left(\frac{-\vec{u}^*}{\Delta t} \right) = -\Delta P' \tag{3.5.17}$$

$$\Delta P' = \frac{1}{\Delta t} \nabla \cdot \vec{u}^* \tag{3.5.18}$$

Equation (3.5.18) is solved with an adapted FISHPACK© solver [1] with respect to the pressure. A parallel version, based on a Schur-complement algorithm, was made available by Grimm-Strele [15]. The new variables of time step $\vec{u}^{n+1}$ can now be updated via,

$$\vec{u}^{n+1} = \vec{u}^* - \Delta t \nabla P' \tag{3.5.19}$$

3.6 Poisson solver

Discretising equation (3.5.18) and solving for P' leads to a matrix inversion, which is usually very expensive and difficult to parallelise with standard domain decomposition methods. Several methods have been established to avoid direct and expensive matrix operations. Especially the elliptic character of the Poisson equation calls for advanced algorithms. We need an efficient numerical scheme, which is able to solve the Poisson equation on parallel computers. Suitable methods include the combination of the Schur complement with the CG- (conjugate gradient) methods or with spectral methods. Both combinations are tested and used in ANTARES. We consider the Poison equation,

$$-\Delta u = f \text{ on } \Omega \tag{3.6.1}$$

$$u = 0 \text{ or } \frac{\partial u}{\partial x_i} = 0 \text{ on } (\Gamma)_{\text{vert}} \tag{3.6.2}$$

where $u \in L^2(\Omega)$, $f \in L^2(\Omega)$, $\Omega \subset \mathbb{R}^n$, $\partial\Omega = \Gamma$ and $i = 1, ..., n$. At first, equation (3.6.1) is discretised and rewritten as a linear system in the form,

$$Au = b, \tag{3.6.3}$$

but even for low resolution simulations the limited memory of the used PE (Processing Element eg. CPU or core) can prevent solving the entire system directly. It is necessary to transform the system $Au = b$ into smaller sub-systems, which are solved on several PE's, is needed. This can be done by the Schur complement method. The subsequent explanation follows in some parts the diploma thesis of Grimm-Strele [15].

Definition 3.6.1. *Let $A \in \mathbb{R}^{n \times n}$ and $n = n_1 + n_2$ be given in the form,*

$$A = \begin{pmatrix} A_{1,1} & A_{1,2} \\ A_{2,1} & A_{2,2} \end{pmatrix}$$

where $A_{1,1} \in \mathbb{R}^{n_1 \times n_1}$, $A_{1,2} \in \mathbb{R}^{n_1 \times n_2}$, $A_{2,1} \in \mathbb{R}^{n_2 \times n_1}$, $A_{2,2} \in \mathbb{R}^{n_2 \times n_2}$ *and* $A_{1,1}$ *is invertible. The* ***Schur Complement Matrix*** $S_A \in \mathbb{R}^{n_2 \times n_2}$ *is defined by,*

$$S_A = A_{2,2} - A_{2,1} A_{1,1}^{-1} A_{1,2} \tag{3.6.4}$$

We assume that $A_{1,1}$ has block structure,

$$\mathrm{A} = \begin{pmatrix} D_1 & & & 0 \\ & D_2 & & \\ & & \ddots & \\ 0 & & & D_p \end{pmatrix}$$

where $p \in \mathbb{N}$, $D_1 \in \mathbb{R}^{n_{11} \times n_{11}}, ..., D_p \in \mathbb{R}^{n_{1p} \times n_{1p}}$ and $n_{11} + ... + n_{1p} = n_1$. Analogously the other sub-matrices can be rewritten,

$$A_{1,2} = (B_1, ..., B_p)^T \tag{3.6.5}$$

$$A_{2,1} = (C_1, ..., C_p) \tag{3.6.6}$$

which leads to,

$$S_A = A_{2,2} - \sum_{j=1}^{p} C_j D_j^{-1} B_j \tag{3.6.7}$$

For $w = (w_1, ..., w_p)^T \in \mathbb{R}^{n_1}$ it follows,

$$A_{1,1} w = \begin{pmatrix} D_1 & & & 0 \\ & D_2 & & \\ & & \ddots & \\ 0 & & & D_p \end{pmatrix} \begin{pmatrix} w_1 \\ w_2 \\ \vdots \\ w_p \end{pmatrix} = \begin{pmatrix} D_1 w_1 \\ D_2 w_2 \\ \vdots \\ D_p w_p \end{pmatrix}$$

The original linear system can be solved on p PE's with the subsequent algorithm.

1. for $j = 1$ to p do
2. solve $D_j z_{1j} = b_{1j}$
3. determine $C_j z_{1j}$
4. end for
5. $v_2 = b_2 - \sum_{j=1}^{p} C_j z_{1j}$
6. solve the Schur complement equation $S_A u_2 = v_2$ in parallel
7. for $j = 1$ to p do
8. solve $D_j u_{1j} = b_{1j} - B_j u_2$

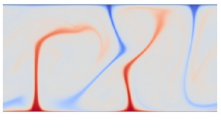

9. end for

The loops can be executed and handled independently on p PE's. Each sub-problem is solved with the conjugate gradient method or the FISHPACK© solver. The global solution is assembled in a subsequent step. A detailed description and further information can be looked up in the diploma thesis of H. Grimm-Strele [15].

3.7 The numerical grid

The quantities in ANTARES are stored on two different grids. In case of compressible fluids a pseudo-staggered grid is used. All variables are defined at the cell centres, except the fluxes. They are calculated on cell faces. The incompressible fluid equations are solved on a staggered grid, the well known MAC grid (marker and cell grid). The MAC grid stores all scalar variables (pressure, salinity, potential temperature) at the cell centres. The vector variables (velocity, momentum) are stored at the cell faces. The boundary (∂D) of the numerical domain is also cell centered, the fluxes are cell faced. 'Using a staggered grid is a simple way to avoid odd-even decoupling between the pressure and velocity. Odd-even decoupling is a discretization error that can occur on collocated grids. This leads to checkerboard patterns in the solutions.'[4] The MAC grid used in ANTARES is depicted in figure 3.2.

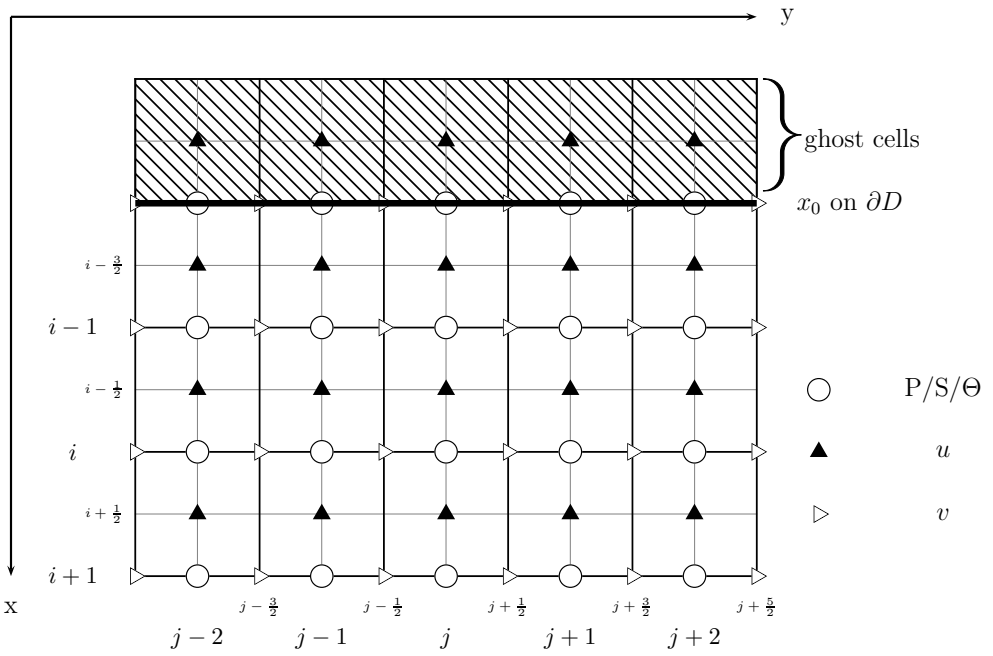

Figure 3.2: MAC grid used in ANTARES

[4] Harlow [20]

A new feature is the combination of the fractional step algorithm with the MacENO method. While (W)ENO calculates the convective velocity at the cell centres, MachENO shifts the advective velocity of the inviscid terms to the cell faces. This ensures more stability due to oscillations, because the MAC grid approach is considered. The method based on this concept was developed by Kwatra et al [26].

Therefore the fluxes, which are used for the ENO reconstruction, need to be modified in the following way.

- inviscid fluxes used with ENO (compressible): $\rho_i \vec{u}_i$, $\rho_i \vec{u}_i^2$, $\rho_i E_j$
- inviscid fluxes used with MachENO (incompressible): $\vec{u}_i \vec{u}_{i+\frac{1}{2}}$, $S_i \vec{u}_{i+\frac{1}{2}}$, $\Theta_i \vec{u}_{i+\frac{1}{2}}$

3.8 Boundary conditions

In semi-convection zones one expects a lot of thin layers, each of them separated by a sharp boundary (think about a horizontally non-bounded Latte Macciatto). Horizontally they are extended widely. This leads to the first assumption that horizontal periodic boundaries are valid for each variable. The vertical boundary conditions are more tricky. We assume that the horizontal boundaries between the layers are only diffusive and there are no fluctuations in the salinity and potential temperature. Therefore 'solid wall' boundary conditions are taken. This leads to fixed boundaries for salinity and potential temperature. Due to the Hodge decomposition theorem (3.5.1) the vertical velocity field has to fulfill $\vec{u} \cdot n = 0$ on ∂D, which coincide with the physical assumptions of a solid wall. Taking 'no-slip' boundary conditions would lead to viscous boundary layers, which are in contradiction to astrophysical assumptions. Therefore, the 'slip' condition is preferred. Additionally, Neumann boundary conditions for the Poisson equation are obvious, because they are a solution of the Navier-Stokes equation at rest. In the following the upper boundary is denoted with x_0, the lower boundary with x_H.

Vertical boundary conditions at x_0 and x_H for the compressible case:

- $c = c_0$, where c_0 is the values of the concentration at the boundary for the initial stratification.
- $T = T_0$, where T_0 is the values of the temperature at the boundary for the initial stratification.
- $\rho u = 0$, while a linear decrease of the values from x_5 to x_0 and x_{H-5} to x_H is calculated for the vertical velocity. This has no influence on the fluxes, because the fluid velocities are so small, that in principle diffusion dominates in these regions. Using very high Rayleigh numbers or steep temperature gradients could cause numerical problems at the vertical boundaries (due to high

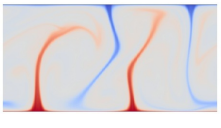

velocities), which are avoided with this settings.

- $\frac{\partial v}{\partial x} = 0$

Vertical boundary conditions at x_0 and x_H for the Boussinesq approximation:

- $S' = 0 \rightarrow S = \bar{S}_0$
- $T' = 0 \rightarrow T = \bar{T}_0$
- $u = 0$,
- $\frac{\partial v}{\partial x} = 0$
- $\frac{\partial P'}{\partial x} = 0$, the vertical pressure boundary condition (a Neumann boundary) is a solution of the Navier-Stokes equation, where the fluid velocity is zero and ρ' is set to zero.

To realise the vertical velocity boundary condition with the ANTARES MAC grid, a reflective stencil is used. Even the intermediate velocities u^* and v^* have to fulfill this condition.

$$u^{(*)}_{x_0+\frac{1}{2}} + u^{(*)}_{x_0-\frac{1}{2}} = 0 \tag{3.8.1}$$

$$u^{(*)}_{x_H+\frac{1}{2}} + u^{(*)}_{x_H-\frac{1}{2}} = 0 \tag{3.8.2}$$

The horizontal direction is continued periodically in all quantities.

3.9 Time stepping

The compressible as well as the incompressible equations were solved with an explicit Runge-Kutta scheme in second order. This second order accurate TVD (Total Variation Diminishing) Runge-Kutta scheme is identical to Heun's predictor-corrector method. An Euler step advances the solution. In the second averaging step a convex combination of the initial data and the intermediate solution is taken.

$$u_t = L(u) \tag{3.9.1}$$

$$u^{(1)} = u^n + \Delta t L(u^n) \tag{3.9.2}$$

$$u^{n+1} = \frac{1}{2}u^n + \frac{1}{2}u^{(1)} + \frac{1}{2}\Delta t L(u^{(1)}) \tag{3.9.3}$$

The total variation (in one dimension) is given by,

$$TV = \sum_j |u_{j+1} - uj| \tag{3.9.4}$$

A system fulfills TVD, if,

$$TV(u^{n+1}) \leq TV(u^n) \tag{3.9.5}$$

TVD schemes are monotonicity preserving, which means that new local extremes cannot be created in the spatial domain, and local minima/maxima are non-decreasing / non-increasing. The time step Δt of the discretised compressible equations is limited by sound waves and therefore takes the form,

$$(\Delta t)_{\text{compr}} = a \, \frac{\min(\Delta x, \Delta y)}{\max(v_c)} \tag{3.9.6}$$

where $a = 0.4$ is the CFL number and v_c the speed of sound. The internal simulation time of the compressible simulations is measured in multiples of the sound crossing time (scrt). Beside this, the thermal diffusion time scale τ_T, where $t_{\text{output}} = 1000 \mathrel{\hat{=}} 1\tau_T$ and the convective overturn time scale have been established for incompressible simulations.

The Boussinesq approximation 'filters' sound waves, which leads to a less restrictive limitation of the time stepping. Usually, the simulations are dominated by diffusion, which guarantees very big time steps.

$$(\Delta t)_{\text{BA}} = a \, \min(\tau_S, \tau_T, \tau_{\text{visc}}, \tau_{\text{fluid}}) \tag{3.9.7}$$

where

$$\tau_S = \frac{(\min(\Delta x, \Delta y))^2}{\kappa_S} \tag{3.9.8}$$

$$\tau_T = \frac{(\min(\Delta x, \Delta y))^2}{\kappa_T} \tag{3.9.9}$$

$$\tau_{\text{visc}} = \frac{(\min(\Delta x, \Delta y))^2}{\nu} \tag{3.9.10}$$

$$\tau_{\text{fluid}} = \frac{\min(\Delta x, \Delta y)}{\max(v)} \tag{3.9.11}$$

Chapter 4

Numerical simulations

A challenging problem is the evaluation and validation of existing theoretical models for semi-convection. Theoretical work has been done by Huppert et al [23] and in a stellar framework by H. Spruit [44], Grossman et al [18] and V. M. Canuto [5]. The first semi-convection simulations in 2D were performed by Merryfield in 1995 [33]. In the following years a couple of publications and theses were published by J. Bascoul [2], K. Kötter [25] or J. Biello [3]. A short summary about these works can be looked up in section 4.9. In this section the numerical results for the simulations for compressible and incompressible fluids are presented. A major question which arises is the amount of heat and Helium/salt transported through the diffusive boundary layers which separate the semi-convective zones. This influences the whole mixing process of the double-diffusive fluid column. Therefore, we have to measure the thermal- and the saline/Helium fluxes, which are parametised in terms of the Nusselt numbers Nu_T and Nu_S. Both numbers were introduced in the latter section. The method to measure them is presented subsequently. The reader will notice that the measurement is done on a single layer. One might think that the results are mainly affected by the boundary conditions. However we show that multi-layer have the same behavior as single layers. Embedded 'free' semi-convective layers without physical boundary contact are stable under certain conditions. The computational effort to measure the fluxes in a multi-layer environment is (currently) too high.

Measurement of the fluxes

The fluxes – in terms of the Nusselt numbers Nu_S and Nu_T – are measured at the vertical boundaries. The following example, which is based on the parameter set: $\sigma = 1.0$, $\tau = 0.01$, $Ra^* = 1.6 \times 10^5$, $R_\rho = 1.5$, shows the method to do the measurement.

The horizontal averages of salinity and temperature are calculated and the gradients are derived. Nu_S (2.5.21) and Nu_T (2.5.20) are calculated at every output time

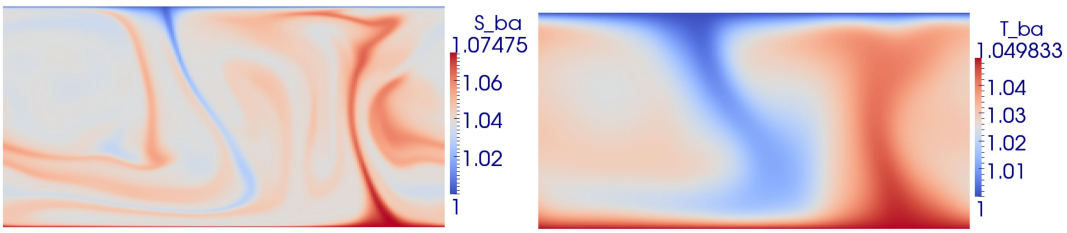

Figure 4.1: Salinity and potential temperature of a fully evolved semi-convection zone

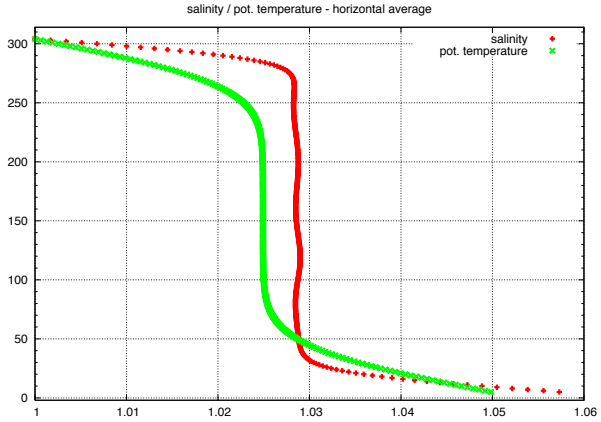

Figure 4.2: Horizontal average of salinity and temperature

step. The resulting plot as a function of time is depicted in figure 4.3. The resulting Nusselt numbers are averaged over the convective time (in our example from time stamp 5 to 9). Finally, the Nusselt numbers become $Nu_S \approx 58$ and $Nu_T \approx 8$. This particular example is insofar interesting, because it does not follow strictly a power law due to its high Prandtl number. See the thesis of J. Biello [3] for a more detailed discussion on high Prandtl number simulations.

4.1 Parameter space, limitations and external dependencies

Apparently fluid dynamical simulation codes are not only influenced by their model dependent input parameters. Especially, numerical algorithms and model constraints limit the feasible physical range of parameters. Some of these limitations and other external dependencies are discussed in this section.

Parameter space

There is a strong correlation between the numerical resolution and the parameter

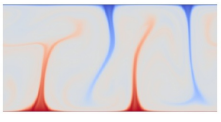

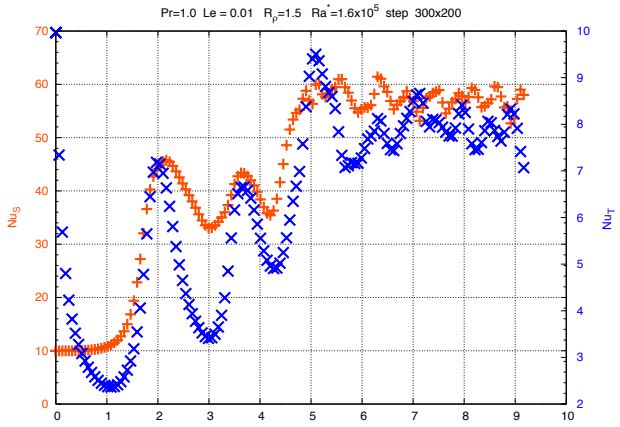

Figure 4.3: Temporal evolution of the Nusselt numbers

space. In appendix B.1 the correlation between boundary layer thickness and numerical resolution is derived. Based on this estimate resolutions of 200×300 or 400×400 for single layer simulations have been established. These resolutions cover a wide spectrum of the assumed parameters. Double layer experiments have been calculated with 300×600 points to ensure a comparable vertical resolution. In these cases the correct Ra_T needs to be representable. The parameter set used for the simulations is depicted in table 4.1.

Quantity	parameter set
σ	$\{10^{-2}, 10^{-1}, 1, 5\}$
τ	$\{10^{-2}, 10^{-1}\}$
Ra_*	$\{1.6 \times 10^4, 5 \times 10^4, 1 \times 10^5, 5 \times 10^5, 1.6 \times 10^6\}$
R_ρ	$\{1.15, 1.5, 2, 5\}$

Table 4.1: Parameter set used for the simulations.

A wider range of σ and τ seems to be important, but it is currently not feasible to enlarge the parameter space to values much smaller then $\tau = 10^{-2}$. A $\sigma = 10^{-3}$ would need a resolution of at least 2000 points in vertical direction. This is quite feasible with current computers. The problem is usually not the Prandtl number, but the Lewis number, which should be at least 2 magnitudes smaller than the Prandtl number. Therefore the Helium layers cannot be resolved correctly. Results with $\sigma < 10^{-4}$ are presently not achievable in the double-diffusive parameter space. Consider, for instance, the realistic stellar values for $\sigma = 10^{-6}$, $\tau = 10^{-8}$ and $Ra_* = 10^2$. An intended thermal boundary layer thickness δ_T of 10% would lead to values of $\delta_T = 5 \times 10^4$ points and $\delta_{He} = 5$ points. Consequently, the vertical resolution has to be 5×10^5 points. The output of the simulations is estimated to $1TB$ of one snapshot from a single precision scalar variable. Fortunately, it can be proved that

simulations in this range are not necessary. This is explained in details in section 4.3.

Limitations by numerical viscosity

The numerical viscosity, here denoted with the numerical Prandtl number σ_{num}, can be estimated with a series of simulations. A fixed Lewis number, eg. $\tau = 10^{-2}$, a semi-convective stable stratification $R_\rho = 1.15$ and a resolution of 200×300 is chosen. The Prandtl number is varied between $\sigma = 10^{-6}$ and $\sigma = 5$ in six steps. The thermal Nusselt number Nu_T as a function of the Schmidt number $Sc = \sigma/\tau$ is plotted. For $Sc < 1$ the thermal Nusselt number is constant, which leads to the conclusion that the numerical viscosity influences the flow significantly. For $Sc \geq 1$ the flow gets affected by the physical diffusion. Therefore, $\sigma_{\text{num}} > 10^{-2}$ represents a lower limit for a resolution of 200×300. This result complies with the boundary layer thickness estimation in appendix B.1. Figure 4.4 depicts the result.

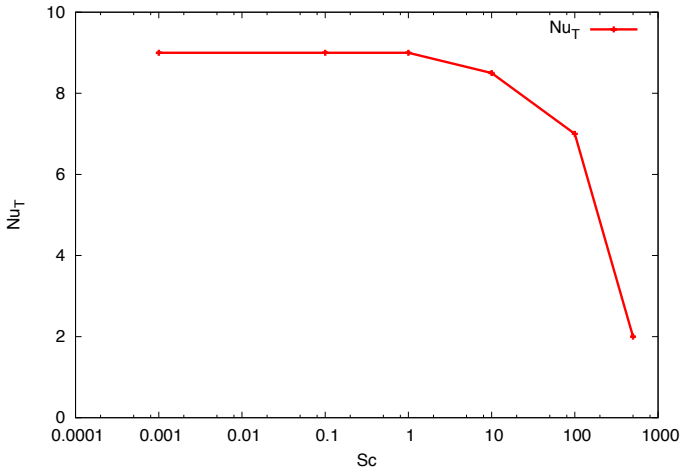

Figure 4.4: A method to estimate the numerical Prandtl number, σ_{num}. The thermal Nusselt number Nu_T is plotted as function of the Schmidt number Sc.

Dependence on aspect ratio

Due to the restricted initial parameter space only a few additional parameters can be considered for the simulations. One of them is the aspect ratio. The outcome of simulations with aspect ratio of $2:1$ was tested against $5:1$ and $10:1$. To gain a valid comparison the same spatial resolution is taken. The values of the Nusselt numbers of the extended boxes are the same compared to the reference aspect ratio of $2:1$. Consequently, the aspect ratio has no significant influence on the fluxes and the input parameters for our simulations. The reference simulation with the parameter set of $\sigma = 10^{-1}$, $\tau = 10^{-2}$, $Ra_* = 10^5$ and $R_\rho = 1.15$ leads to $Nu_S = 90$

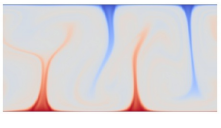

and $Nu_T = 8.5$. The simulation with $5:1$ results in $Nu_S = 90$ and $Nu_T = 9.0$. The most extended box with an aspect ratio of $10:1$ and a spatial resolution of 1500×300 has Nusselt numbers of $Nu_S = 80$ and $Nu_T = 8.75$. Variations in the results of about 10% are typical and hence not avoidable.

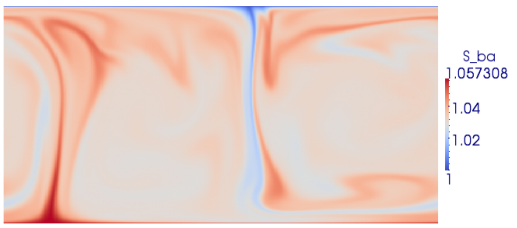

Figure 4.5: Salinity at aspect ratio 2:1

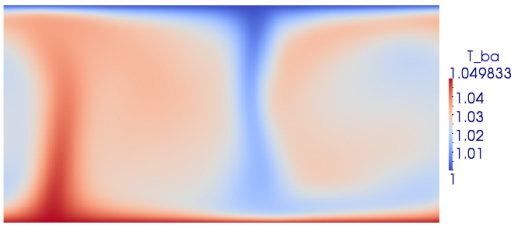

Figure 4.6: Temperature at aspect ratio 2:1

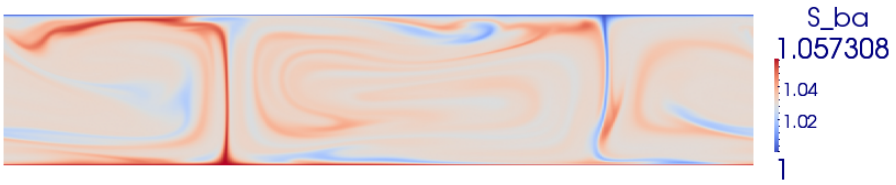

Figure 4.7: Salinity at aspect ratio 5:1

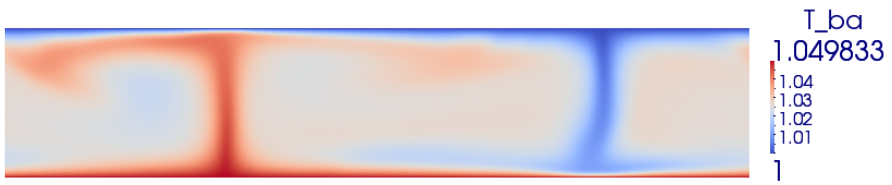

Figure 4.8: Temperature at aspect ratio 5:1

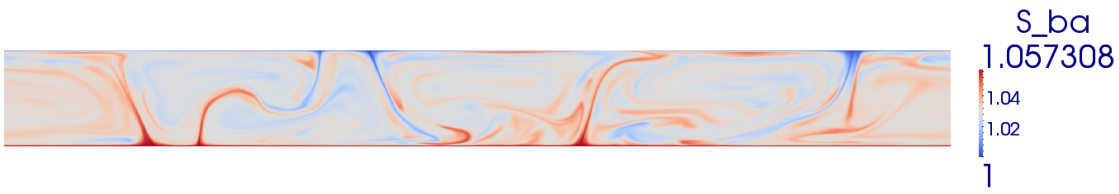

Figure 4.9: Salinity at aspect ratio 10:1

Dependence on initial stratification

Starting the simulations with a constant stratification leads to temporally stable (in the sense of semi-convection) Rayleigh-Bénard cells. The formation of these cells comes along with a diffusive initial era and an oscillatory phase. All three phases are depicted in figure 4.11. The duration of the initial formation process

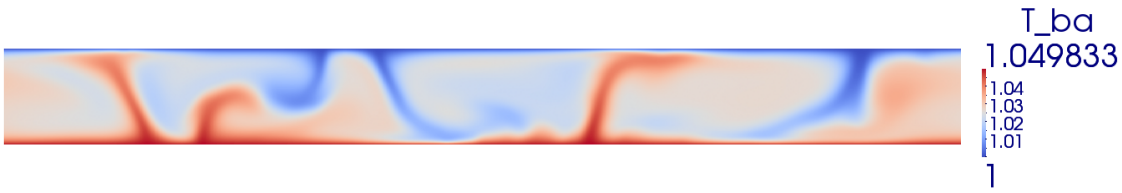

Figure 4.10: Temperature at aspect ratio 10:1

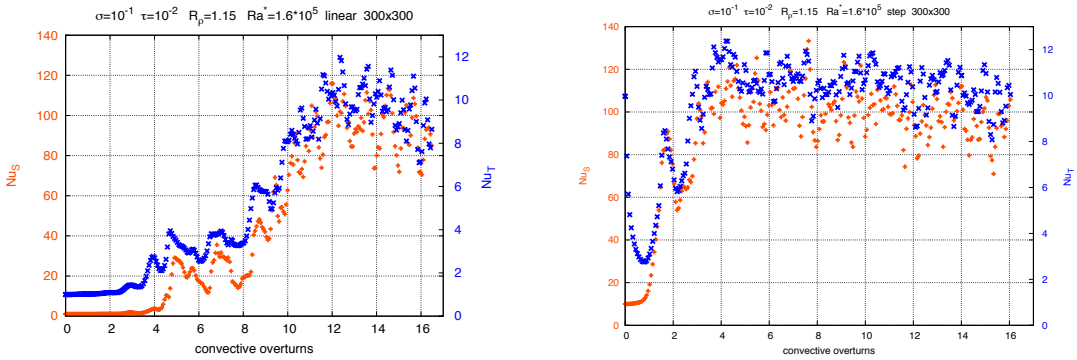

Figure 4.11: Nusselt numbers for linear (left figure) and direct step (right figure) initial stratification. Here, the time scale is measured in convective turnovers. The formation of a semi-convective zone ($t = 10$ to $t = 14$) starting from a linear stratification is the consequence of a diffusive phase ($t = 0$ to $t = 4$) and followed by an oscillatory phase ($t = 4$ to $t = 10$). For the specified parameter space the convective rolls are established within 12 turnover cycles. Starting the simulation from a step leads to the same result, but saves computational time. Differences in the Nusselt numbers of both simulations are within the statistical variations of 10%.

is mainly determined by R_ρ and Ra_*. To avoid the initial information-less stages, simulations with an initial step in salinity and temperature are chosen. This yields a computational cost of a factor of up to 100 for small values in Ra_* and high R_ρ. Whether the stratification is linear or a step, both initial conditions lead to the same results for the Nusselt numbers.

4.2 Semi-convection in incompressible fluids

The results presented here are based on about 100 numerical simulations in Boussinesq approximation. The thermal flux in terms of Nu_T and the saline flux in terms of Nu_S as function of the input parameters σ, τ, Ra_* and R_ρ are analyzed. This is insofar interesting as extrapolations to parameter spaces are possible which are not covered by numerical simulations.

4.2.1 Dependence on τ

The theory of Huppert and Moore [23], which describes double-diffusive mixing, suggests that the saline Nusselt number scales with the square root of the Lewis number and the thermal Nusselt number.

$$Nu_T = \tau^{1/2} Nu_S \tag{4.2.1}$$

A condition which is relevant for low Ra_* takes into account that the diffusive term ($Nu_T = 1$) is subtracted from (4.2.1).[1] In that case the convective heat flux vanishes for $Ra_* \downarrow 0$.

$$Nu_T - 1 = \tau^{1/2} Nu_S \tag{4.2.2}$$

Both relations are theoretically valid for $Ra_T \to \infty$, because the difference according to the diffusion correction vanishes. Except for the sub-critical region, where $Ra_T < Ra_{crit}$, the theoretical estimate (4.2.1) could be reproduced satisfactorily for the entire parameter space. There are two cases to distinguish, the high Prandtl number regime $\sigma = 1.0$ and the low Prandtl number regime $\sigma = 10^{-1}$.

Dependence on τ at $\sigma \geq 1.0$

The Nusselt number correlation (4.2.1) could be confirmed satisfactorily for the high Prandtl number case ($\sigma \geq 1.0$) as long as the stability parameter $R_\rho \leq 2$. The thick viscous boundary layer inhibits convection efficiently for values $R_\rho > 2$, which leads to a sub-critical behavior. These simulations are in the range $Ra_* \leq 5.0 \times 10^4$ and $R_\rho > 2$. The diffusion corrected equation (4.2.2) fits better than the original formulation. Figure 4.13 depicts the diffusion corrected formulation, figure 4.12 the original formulation. Hence, the diffusion corrected correlation between the thermal and the saline Nusselt number explains the behavior of the flow much better in the nearly sub-critical regime. Values of Nu_T far away from this limit ($Nu_T > 10$) are not effected. Here, the classical formulation dominates due to the small contribution of the correction term.

Dependence on τ at $\sigma < 1.0$

Figure 4.15 and 4.14 depict the low Prandtl number case ($\sigma < 1.0$) for different Ra_* and R_ρ, where the Lewis number is fixed to $\tau = 10^{-2}$. The difference in both figures is the 'diffusion correction factor' of equation (4.2.2). Simulations with $Ra_* \leq 1.6 \times 10^5$ benefit from the correction. Simulations with $Ra_* \geq 5.0 \times 10^5$ follow the original formulation. Due to the fact, that $Ra_* \approx 1 - 100$ in semi-convective zones of our interest, the corrected formulation is preferred for later extrapolations into the stellar parameter space.

[1] See section 4.4 for a detailed discussion about the stellar relevant parameter space, where $Ra_* < 10^3$

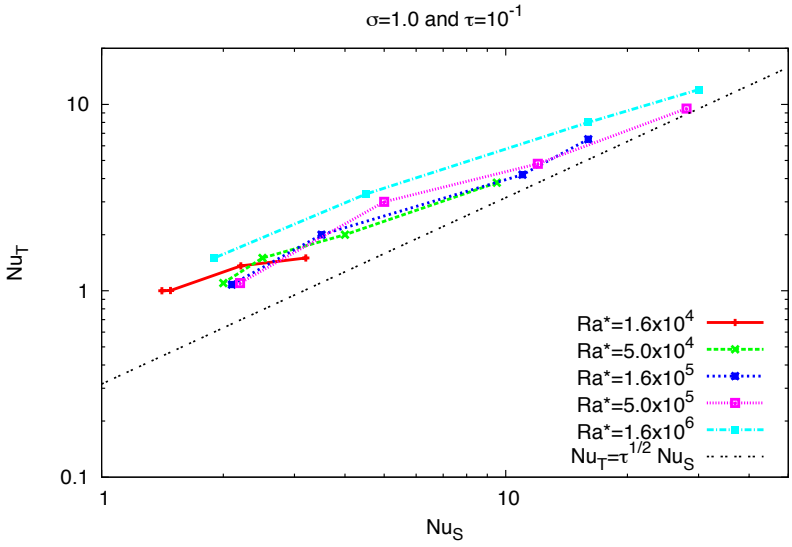

Figure 4.12: Nu_T as function of Nu_S for $\sigma = 1.0$ and $\tau = 10^{-1}$. In this figure the classical correlation (4.2.1) is used as reference line. Each line stands for a different Ra_*. Along each line the stability parameter R_ρ decreases in 4 steps (5, 2, 1.5, 1.15) or 3 steps (2, 1.5, 1.15). For high Prandtl numbers the classical correlation fails in the low Rayleigh number regime.

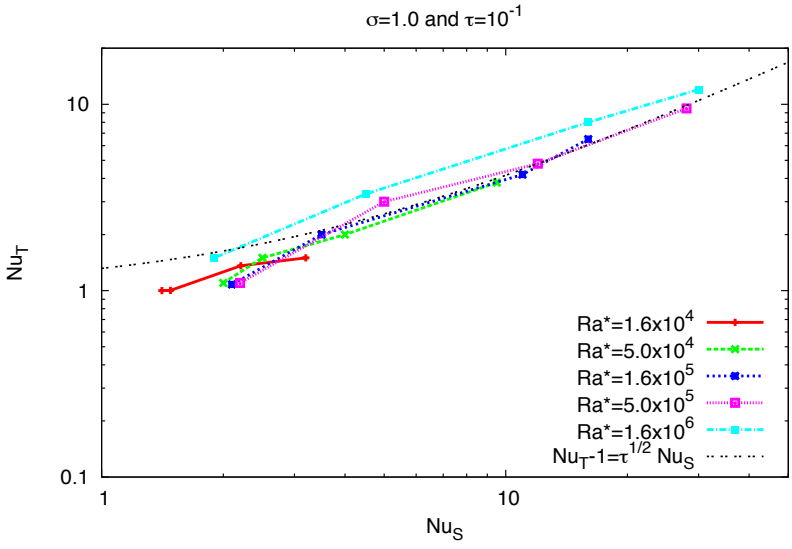

Figure 4.13: Nu_T as function of Nu_S for $\sigma = 1.0$ and $\tau = 10^{-1}$. In this figure the diffusion corrected correlation (4.2.2) is used. Each line stands for a different Ra_*. Along each line the stability parameter R_ρ decreases in 4 steps (5, 2, 1.5, 1.15) or 3 steps (2, 1.5, 1.15). The high Prandtl number regime profits from the correction in the low Rayleigh number regime.

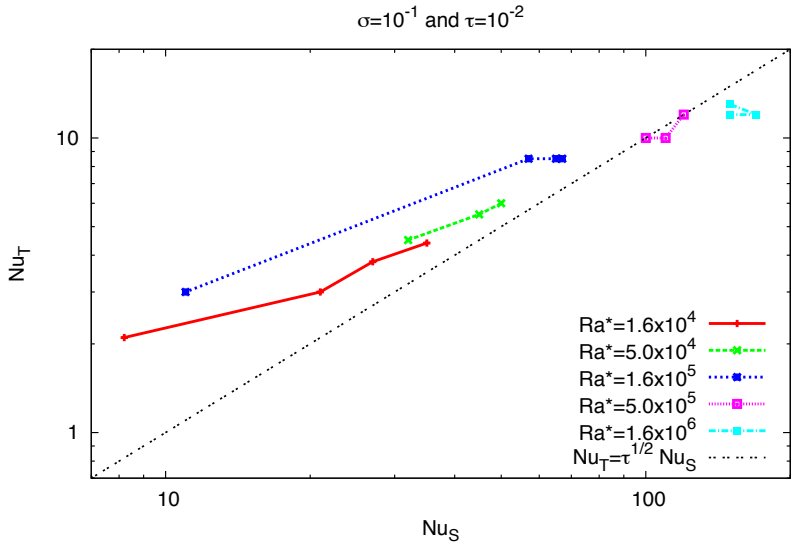

Figure 4.14: Nu_T as function of Nu_S for $\sigma = 10^{-1}$ and $\tau = 10^{-2}$. In this figure the classical correlation (4.2.1) is used as reference line. Each line stands for a different Ra_*. Along each line the stability parameter R_ρ decreases in 4 steps (5, 2, 1.5, 1.15) or 3 steps (2, 1.5, 1.15). Even for lower Prandtl numbers the classical correlation fails in the low Rayleigh number regime.

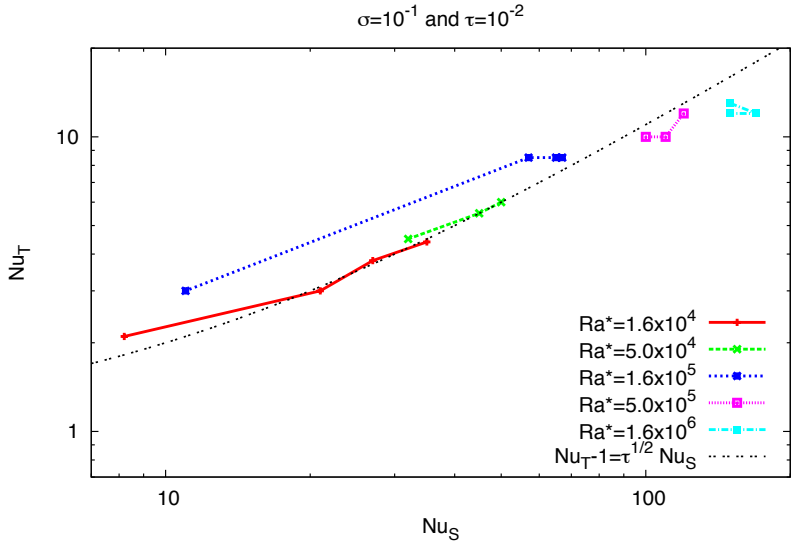

Figure 4.15: Nu_T as function of Nu_S for $\sigma = 10^{-1}$ and $\tau = 10^{-2}$. In this figure the diffusion corrected correlation (4.2.2) is used as reference line. Each line stands for a different Ra_*. Along each line the stability parameter R_ρ decreases in 4 steps (5, 2, 1.5, 1.15) or 3 steps (2, 1.5, 1.15). The lower Prandtl number regime profits also (in comparison to $\sigma = 1$) from the correction in the low Rayleigh number regime.

4.2.2 Dependence on Ra_T and Ra_*

A power law is defined as a polynomial scale invariant binary relationship in the form,

$$p(x) = ax^b + o(x^b) \tag{4.2.3}$$

where $a, b \in \mathbb{R}$. Experiments showed that the thermal flux can be described as a function of the Rayleigh number. This function follows the power law formulation (4.2.3).

$$Nu_T \propto \alpha Ra_T^{\beta} \tag{4.2.4}$$

where $0 < \alpha < 1$ and $0 < \beta \leq 0.5$. Experiments done by Castaing et al [6] lead to

$$Nu_T = 0.23 Ra_T^{0.282}. \tag{4.2.5}$$

A measurement over the remarkable range of eleven magnitudes ($10^6 \leq Ra_T \leq 10^{17}$) has been performed by Niemela et al [37] with the resulting power law,

$$Nu_T = 0.124 Ra_T^{0.309} \tag{4.2.6}$$

Spruit [44] estimated a viscosity independent formulation for the semi-convective case in a stellar parameter space of σ

$$Nu_T = 0.5(Ra \cdot \sigma)^{0.25} = 0.5 Ra_*^{0.25} \tag{4.2.7}$$

The 'diffusion corrected' formulation takes the form,

$$Nu_T - 1 = 0.5 Ra_*^{0.25} \tag{4.2.8}$$

The different power laws for $10^1 < Ra_T < 10^9$ are depicted in figure 4.16. Equation (4.2.5) and (4.2.6) do not differ much for $Ra_T > 10^6$. The power law (4.2.7) takes the Prandtl number into account. Therefore differences for decreasing σ are obvious. Figure 4.15 shows that the diffusion corrected formulation of the power law (4.2.8) is an upper limit for simulations with $\sigma < 1$. An asymptotic behavior of the numerical simulation data set, even for small Ra_* can be observed for all presented power laws. Figure 4.17 pictures the low Prandtl number regime, figure 4.18 shows the high Prandtl number outcome. The classical power laws fail for high Prandtl number semi-convection simulations due to the high viscosity. This follows from $\sigma \geq 1$, where $\delta_{\text{visc}} > \delta_T$. In this situation two solutions can occur, a thermal and a convective one. A detailed view on this point was done by Grossman et al [17] p294. The diffusion corrected equation (4.2.8) is a valid approximation for the stellar case, because the data set leads to a perfect fit with it.

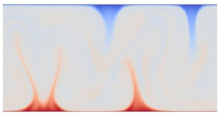

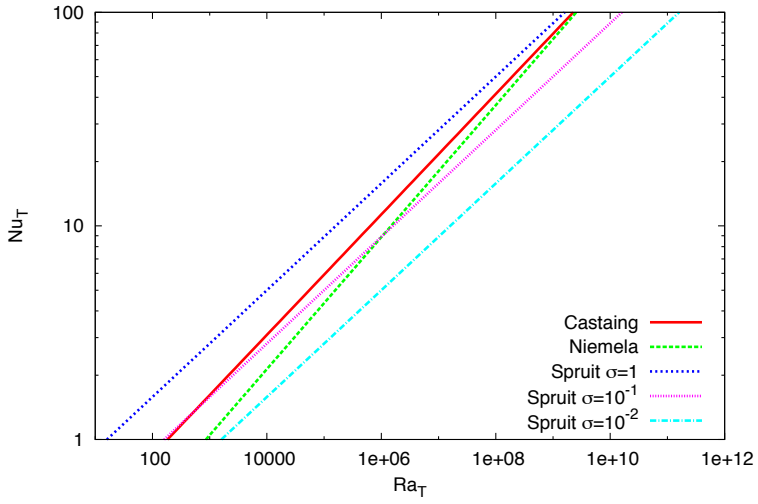

Figure 4.16: Several power laws in the form $Nu_T \propto \alpha Ra_T^{\beta}$.

4.2.3 Dependence on R_ρ

It remains still an open question how the thermal convection is affected by the counteracting stable concentration stratification. The figures 4.19-4.20 show the dependencies of Nu_T on R_ρ for various values of Ra_*. There are again two distinct σ regions, $\sigma \geq 1$ and $\sigma < 1$. The dependence of the thermal Nusselt number on $\sigma = 1$ is depicted in figures 4.19-4.20. For the low Prandtl number regime this dependence decreases and especially for $R_\rho \leq 2$ the fluxes are nearly constant. It seems that a small Lewis number $\tau < 10^{-2}$ has an influence on the thermal fluxes. Figure 4.19 shows that even for $\sigma = 1$ the thermal Nusselt number does not change significantly for $R_\rho < 5$. But this is just a suggestion based on 12 simulations and therefore by no means proven.

4.3 Comparison of compressible and incompressible simulations

Numerical simulations of compressible fluids lead to restrictions in time stepping (due to the need to resolve sound waves). Hence, the simulations performed with the explicit solver take up to 100 times[2] longer for the same resolution compared to the incompressible solver. For instance a comparable simulation with a vertical extent of $\epsilon = 0.1$ and a resolution of 400×400 needs 32 processors and $3 - 4$ days

[2]This depends mainly on the fluid velocity of the incompressible flow.

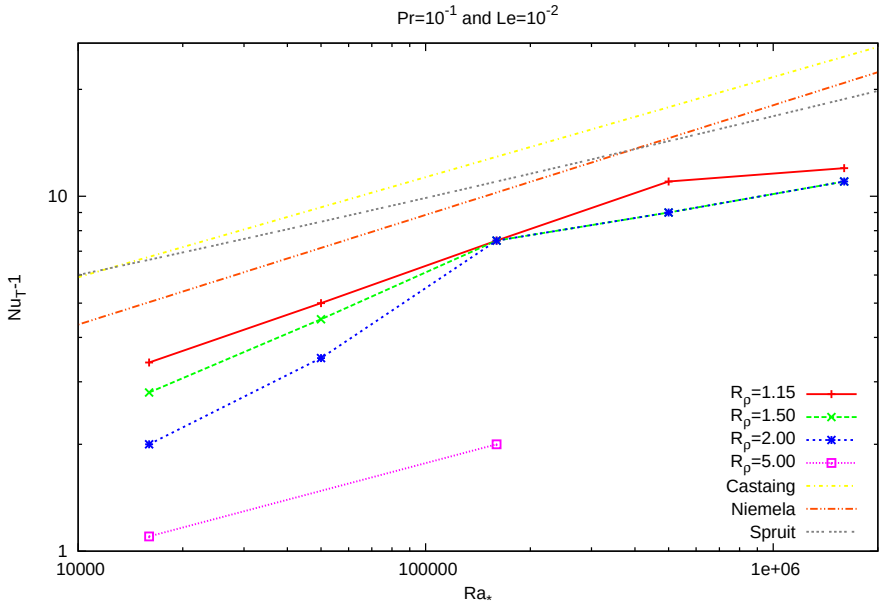

Figure 4.17: $Nu_T - 1$ as function of Ra_* for $\sigma = 10^{-1}$ and $\tau = 10^{-2}$. Simulation with different R_ρ where tested against theoretical convection power laws. The power laws fit better for small values of R_ρ.

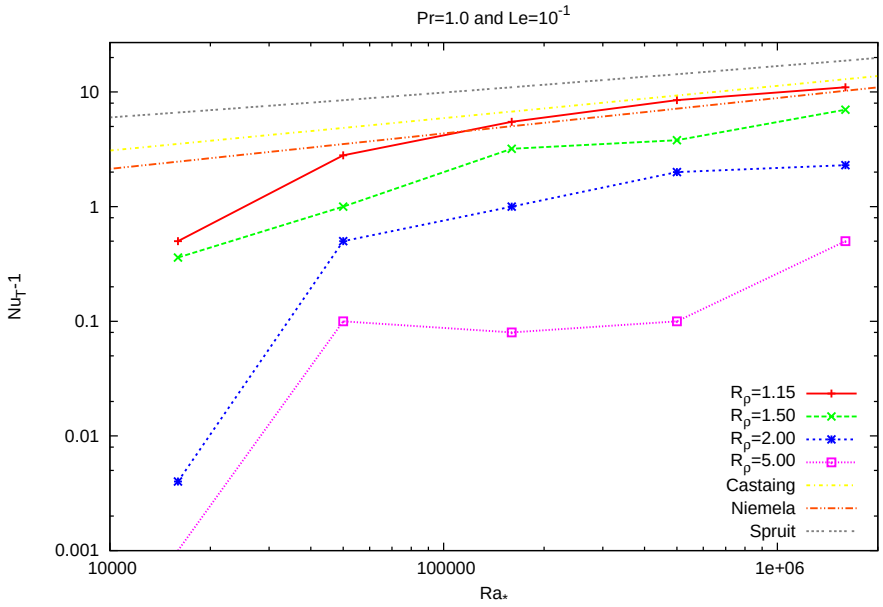

Figure 4.18: $Nu_T - 1$ as function of Ra_* for $\sigma = 1.0$ and $\tau = 10^{-2}$. Simulation with different R_ρ where tested against theoretical convection power laws. The power laws fit better for small values of R_ρ, but fail in case of small Ra_*.

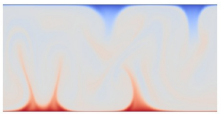

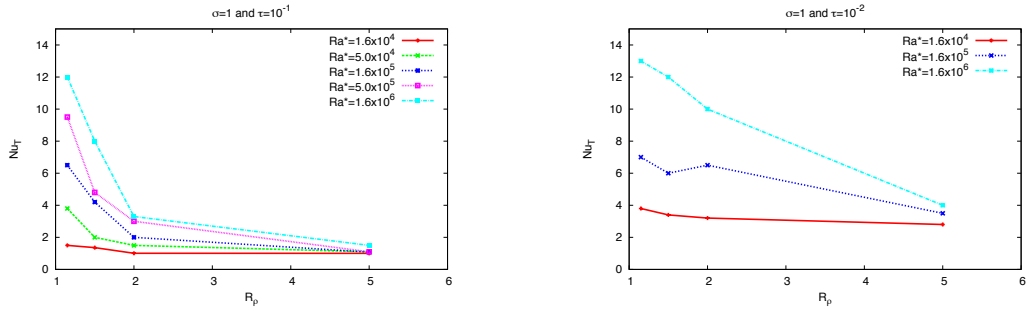

Figure 4.19: Thermal Nusselt number as function of R_ρ for $\sigma = 1.0$ and $\tau = 10^{-1}$ (left) and $\sigma = 1.0$ and $\tau = 10^{-2}$ (right).

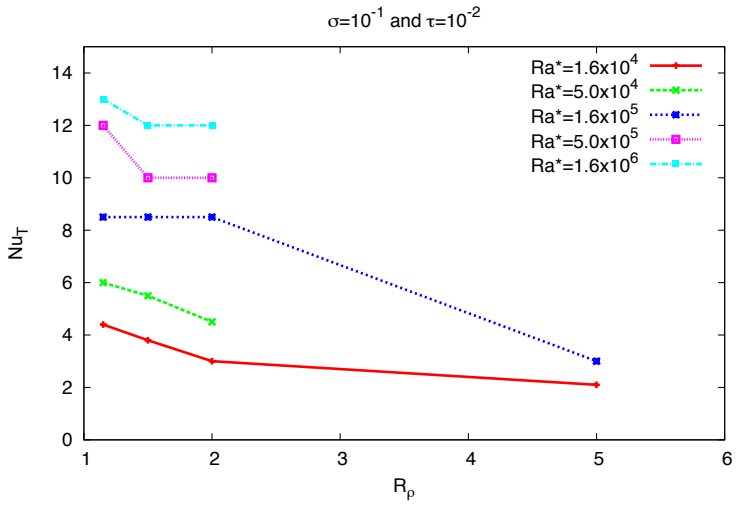

Figure 4.20: Nu_T as function of R_ρ for $\sigma = 10^{-1}$ and $\tau = 10^{-2}$. An influence can be observed for the high R_ρ regime.

for $R_\rho > 1.5$. Therefore, only a few tests with the explicit solver have been done. In principle two cases have to be distinguished, high boxes with $\epsilon = 1.0$ and small boxes with $\epsilon = 0.1$, since the fluid velocities differ significantly in these two cases. The height H of a compressible simulation box is defined by its pressure difference, which can easily expressed in pressure scale heights H_P and ϵ.

$$H_p = p\left(\frac{\partial p}{\partial z}\right)^{-1} \approx \frac{p}{\rho g} \tag{4.3.1}$$

$$\epsilon = H/H_p \tag{4.3.2}$$

The height in the Boussinesq case, H_{BA}, is chosen arbitrarily, but fixed. It cannot be compared with the height in the compressible case H. Hence, they have different denominations. It is assumed that for $\epsilon = 0.1$ the vertical differences of thermodynamic quantities are comparable to those of incompressible fluids. This leads to typical variations of $\Delta\Theta = 2\% - 5\%$ or $\nabla_\Theta = 0.05 - 0.2$. While the pressure difference is determined by ϵ, the temperature stratification can be adjusted with help of the super-adiabatic gradient ∇_Θ that is set initially. The incompressible simulations are all set up with $\Delta T = 5\%$. The choice of the vertical temperature difference is arbitrary, but $\Delta T = 5\%$ have also been used with in other codes, eg. MITgcm code [34]. The value for ∇_Θ seems to be very high, but otherwise the convection would not be efficient enough on short time scales for $R_\rho > 2$. The scalar field for concentration is the salinity S in the incompressible case and the mean molecular weight μ in the case of an ideal gas. The mean molecular weight can easily be expressed as a function of helium content (for idealised thermodynamics).

4.3.1 'Small box' simulation: $\epsilon = 0.1$

The comparison of both solvers has been done with slightly different parameter values (compared to the Nusselt number study). In principle, the fixed potential temperature contrast of the incompressible simulations changed here from $\Delta\Theta = 0.05$ to $\Delta\Theta = 0.019$. The real temperature gradient can directly be compared with the potential temperature Θ as long as the adiabatic temperature gradient is fixed to $\nabla_{\mathrm{ad}} = 0.4$.

Simulations with the following values have been compared directly. The results are shown in table 4.3.

Quantity	compressible	incompressible
temp. diff.	∇_Θ=0.2	$\Delta\Theta = 0.019$
height	$\epsilon = 0.1$	$H_{\mathrm{BA}} = 1.0$
resol.	400×400	400×400
asp. ratio	$2:1$	$2:1$

Table 4.2: Parameter set used for the comparison simulations with $\epsilon = 0.1$.

The differences in the simulations done in Boussinesq approximation and explicit approach are due to stabilising effects of high Prandtl- and Lewis number as well as low Rayleigh number. Especially, Ra_T has a strong influence on the conductive flux. This influence is shown in figure 4.21 and 4.22. For small values of Ra_T (not Ra_*) the thermal diffusion coefficient is larger. Hence, the conductive flux F_{cond} transports more energy (cf. figure 4.21). The convective energy transport in simulations with higher values for Ra_T and lower values for σ and τ dominates the mixing processes. Therefore, $F_{\mathrm{conv}} \gg F_{\mathrm{cond}}$, which is shown in figure 4.22.

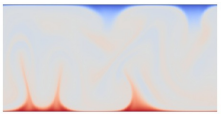

compressible fluid with $\epsilon = 0.1$								
σ	τ	R_ρ	Ra_*	$(Nu_S)_{\mathrm{BA}}$	$(Nu_T)_{\mathrm{BA}}$	$(Nu_S)_{\mathrm{ex}}$	$(Nu_T)_{\mathrm{ex}}$	Check
10^{-1}	10^{-2}	2.0	1.6×10^5	60	8	55	7	✓
10^{-1}	10^{-2}	1.2	1.6×10^5	110	12	110	11	✓
10^{-1}	10^{-2}	2.0	1.6×10^6	150	12	130	10	✓
10^{-1}	10^{-2}	1.2	1.6×10^6	200	16	200	14	✓
1.0	10^{-1}	2.0	1.6×10^5	3.5	2	11	1.5	×
1.0	10^{-1}	1.2	1.6×10^5	45	15	17	5	~
1.0	10^{-1}	2.0	1.6×10^6	4	3.5	26	10	×
1.0	10^{-1}	1.2	1.6×10^6	33	11	26	10	✓

Table 4.3: Nusselt numbers for the compressible and the incompressible simulation in the small box.

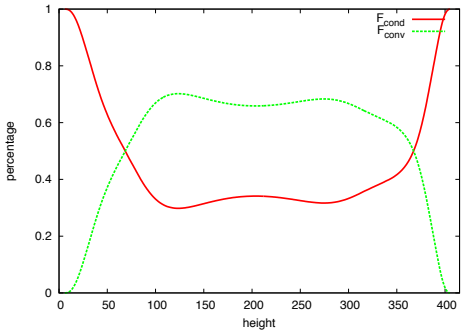

Figure 4.21: Simulation with $Ra_T = 1.6 \times 10^5$, $R_\rho = 2.0$, $\sigma = 1.0$, $\tau = 10^{-1}$ and $\epsilon = 0.1$. The conductive flux F_{cond} is very efficient in transporting energy.

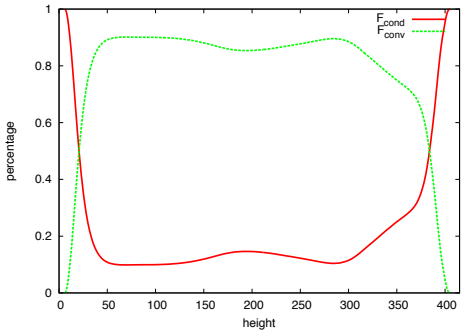

Figure 4.22: Simulation with $Ra_T = 1.6 \times 10^5$, $R_\rho = 1.2$, $\sigma = 10^{-1}$, $\tau = 10^{-2}$ and $\epsilon = 0.1$. The conductive flux F_{cond} is significantly lower compared to the adjoining simulation. The convective flux F_{conv} transports most of the energy.

4.3.2 'Big box' simulation: $\epsilon = 1.0$

Simulations done with $\epsilon = 1.0$ behave quite similarly to these done with $\epsilon = 0.1$. Even the fluxes of both regimes are comparable (see figure 4.23 and 4.24). This leads to the conclusion that double-diffusive convection simulations can be done in boxes with $0.1 \leq \epsilon \leq 1.0$ for comparison reasons with the Boussinesq approximation. The mixing processes do not significantly differ as long as the Rayleigh number is high enough, $Ra_T > 5.0 \times 10^5$. Differences due to compressibility could not be observed. The velocities are too small to see these effects in this setup.

Quantity	compressible	incompressible
temp. diff.	∇_Θ=0.2	$\Delta\Theta = 0.019$
height	$\epsilon = 1.0$	$H_{\mathrm{BA}} = 1.0$
resol.	400×400	400×400
asp. ratio	$2:1$	$2:1$

Table 4.4: Parameter set used for the comparison simulations with $\epsilon = 1.0$.

compressible fluid with $\epsilon = 1.0$								
σ	τ	R_ρ	Ra_*	$(Nu_S)_{\mathrm{BA}}$	$(Nu_T)_{\mathrm{BA}}$	$(Nu_S)_{\mathrm{ex}}$	$(Nu_T)_{\mathrm{ex}}$	Check
10^{-1}	10^{-2}	2.0	1.6×10^5	60	8	130	20	~
10^{-1}	10^{-2}	1.2	1.6×10^5	110	12	120	12	✓
10^{-1}	10^{-2}	2.0	1.6×10^6	150	12	140	12	✓
10^{-1}	10^{-2}	1.2	1.6×10^6	200	16	160	18	✓
1.0	10^{-1}	2.0	1.6×10^5	3.5	2	14	5	×
1.0	10^{-1}	1.2	1.6×10^5	45	15	24	8	~
1.0	10^{-1}	2.0	1.6×10^6	7	4.5	25	10	~
1.0	10^{-1}	1.2	1.6×10^6	33	11	30	9	✓

Table 4.5: Nusselt numbers for the compressible and the incompressible simulation in the big box

4.3.3 The low Mach number limit of the compressible solver

An asymptotic analysis ansatz in power of the Mach number Ma explains why the low Mach number limit fails for discretised compressible Euler equations. It was proven by Guillard et al [19] that the solution of the discrete system contains pressure fluctuations in the order of $\mathcal{O}(Ma)$. The pressure of the continuous equations scales with $\mathcal{O}(Ma^2)$. This explains why the numerical solution fails for subsonic flows ($Ma < 0.1$). Consequently on a fixed mesh the pressure scaling can not be recovered correctly for low Mach number flows. This behavior can be well observed in 'small box' simulations where the fluid velocities are in the order of $Ma = 10^{-2} - 10^{-3}$. High values of the stability parameter $R_\rho > 1.5$, the Prandtl- and Lewis number $\sigma > 10^{-1}$, $\tau > 10^{-2}$ lead typically to slower flows. Therefore a comparison with the Boussinesq approximation should not be valid any more in this parameter space.

Four simulations with height of $\epsilon = 0.1$ have been performed. Typical values for the speed of sound are $v_c = 9300$cm/s. Table 4.6 depicts the corresponding Mach number for each simulation. It is astonishing that even though the Mach numbers

R_ρ	τ	Ma
1.2	10^{-2}	3.2×10^{-3}
1.2	10^{-1}	1.9×10^{-3}
2.0	10^{-2}	1.6×10^{-3}
2.0	10^{-1}	3.2×10^{-4}

Table 4.6: Low mach number simulations

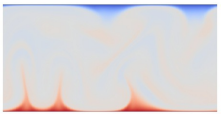

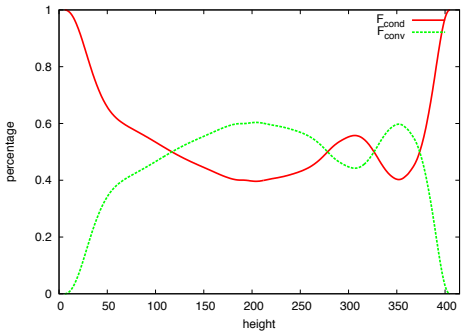

Figure 4.23: Simulation with $Ra_T = 1.6 \times 10^5$, $R_\rho = 2.0$, $\sigma = 1.0$, $\tau = 10^{-1}$ and $\epsilon = 1.0$. The conductive flux F_{cond} is very efficient in transporting energy.

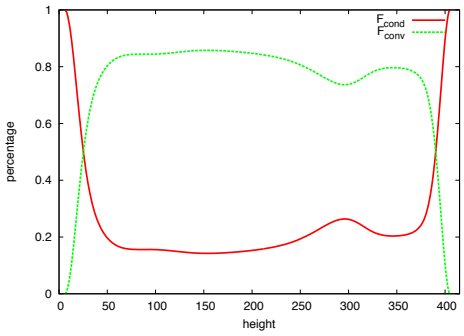

Figure 4.24: Simulation with $Ra_T = 1.6 \times 10^5$, $R_\rho = 1.2$, $\sigma = 10^{-1}$, $\tau = 10^{-2}$ and $\epsilon = 1.0$. The conductive flux F_{cond} is significantly lower compared to the adjoining simulation. The convective flux F_{conv} transports most of the energy.

are very small, the results are comparable with the Boussinesq approximation as long as $\sigma < 1$ and $\tau < 10^{-1}$. Boxes with $H = H_P$ and $Ra_T < 5.0 \times 10^5$ are sometimes affected by this phenomenon. In these cases the flux ratio of F_{conv} and F_{cond} decides about the validity of the resulting Nusselt numbers. The author highly recommends to choose a native low Mach number solver or the Boussinesq approximation in this parameter space, although some results fit perfectly. Problems with explicit solvers will and do occur in the low Mach number limit. Hence the results are inaccurate.

4.4 Extension to the stellar parameter space

In this section a formalism is presented, which allows to estimate the number of semi-convection layers, the super-adiabatic gradient and the fluxes in a semi-convective zone without knowing the exact convective behavior of such a region. An estimate based on numerical results leads to functions of the form: $(\nabla - \nabla_{\text{ad}})(\epsilon)$, $Ra_*(\epsilon)$, $\text{Flux}(\epsilon)$, where $\epsilon = H/H_p$. It is very important to know these relations, because the efficiency of semi-convective mixing in terms of the super-adiabatic gradient is still not very well known. The semi-convective zone in a stellar model is sufficiently limited in extent and consequences the assumptions that the overall structure of the star does not depend much on the way semiconvection are calculated. But the additional diffusion of helium by semiconvective mixing can be important for later evolutionary stages. During the semi-convective phase itself the thermal structure of the star is not affected much. The consequence of this is that in contrast with laboratory and geophysical situations, in a simple stellar model the molecular heat flux F_{cond} can be considered as known in the semiconvective zone to be studied,

rather than the temperature gradient ∇. Since the radiative contribution $F_{\rm rad}$ to the heat flux is known to good approximation from the thermal structure of the star, the convective heat flux $F_{\rm conv} = F_{\rm cond} - F_{\rm rad}$ transported by semi-convection is then also known. What is not yet known is the efficiency of convection: i.e. how close to the adiabatic gradient $\nabla_{\rm ad}$ the mean thermal gradient ∇ will turn out to be as a result of semiconvective transport. The ratio $f^{\rm BA}$ of the convective to the radiative heat flux in the Boussinesq approximation is to be identified with the ratio $f^{\rm S} = F^{\rm S}_{\rm conv}/F^{S}_{\rm sa}$ of the convective to the super adiabatic radiative gradient in the star. In the limit $H_p \to \infty$, both ratios can be identified,

$$f^{\rm BA}(Ra_*) = f^{S}(Ra_*, \epsilon \downarrow 0) \tag{4.4.1}$$

Suppose that the dependence of the thermal flux (eg. as Nu_T) on Ra_* is known from an approximate model or from numerical simulations. In the approximate model of Spruit [44] an asymptotic dependence $Nu_T - 1 = f^{\rm BA}$ was estimated for large Ra_* as,

$$(Nu_T) = f^{\rm BA} \approx 0.5\,{\rm Ra}_*^{1/4} \tag{4.4.2}$$

Since conditions at low Ra_* will also be relevant here, we modify the estimate in terms of the 'diffusion correction' as

$$(Nu_T)^{\rm BA} - 1 = f^{\rm BA} \approx 0.5\,{\rm Ra}_*^{1/4} \tag{4.4.3}$$

(so that the convective heat flux vanishes for $Ra_* \downarrow 0$). This is only an estimate based on the numerical results presented later on, but suffices for the estimate below. In terms of the logarithmic gradients:

$$f^{\rm S} = \frac{\nabla_{\rm rad} - \nabla}{\nabla - \nabla_{\rm ad}} = \frac{\nabla_{\rm rad} - \nabla}{\nabla_\Theta}. \tag{4.4.4}$$

In terms of astrophysical quantities, Ra_* can be rewritten as

$$Ra_* = \nabla_\Theta R \tag{4.4.5}$$

where

$$R = \frac{gH^4}{\kappa_T^2 H_P} = \frac{gH_P^3}{\kappa_T^2}\left(\frac{H}{H_P}\right)^4 = \frac{gH^3}{\kappa_T^2}\epsilon^4 \tag{4.4.6}$$

is a function of the double diffusive layer thickness H and the local thermodynamic state, but not of the (still unknown) temperature gradient ∇. Collecting all assumptions lead to,

$$0.5\,{\rm Ra}_*^{1/4} = (\nabla_{\rm rad} - \nabla_{\rm ad})\frac{R}{{\rm Ra}_*} - 1. \tag{4.4.7}$$

This defines a relation between R and Ra_*, or equivalently between Ra_* and the semiconvective layer thickness H. We are now in the position to estimate the range

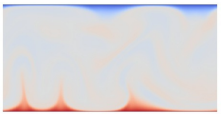

of parameter values for semiconvection in a star. Further, we can derive which part of this range can be covered directly by numerical simulations.

Example

A typical semi-convection zone[3] of a massive star ($M \approx 15M_{\odot}$) around main sequence turnoff is depicted in figure 4.25. The realistic stability parameter is typically in the range of $10 < R_{\rho} < 500$. Characteristic values for the physical quantities in the

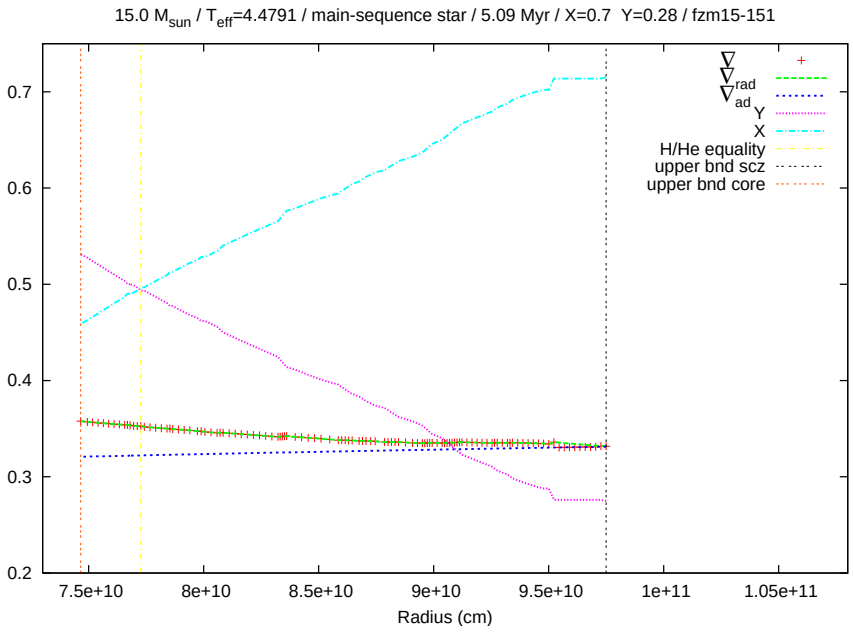

Figure 4.25: Semi-convection zone of a $15_{\odot}$ star.

semi-convective zone depicted in figure 4.25 are, $g \approx 10^6 cm/s^2$, $\kappa_T \approx 3 \times 10^8 cm^2/s$, $H_p \approx 2 \times 10^{10} cm$, $\nabla_{ad} \approx 0.4$ and $\nabla_{rad} - \nabla_{\mathrm{ad}} \approx 0.02$ Using latter values lead to,

$$R \approx 10^{20} \epsilon^4 \tag{4.4.8}$$

Now it is possible to derive the functions $\nabla_{\Theta}(\epsilon)$, $Ra_*(\epsilon)$ and $f^s(\epsilon)$. Unfortunately, all of them are implicit functions, but they can easily solved with eg. Mathematica©. We are using (4.4.7) and the values for $\nabla_{\mathrm{rad}} - \nabla_{\mathrm{ad}}$ and R to derive the following implicit functions: The super adiabatic gradient as function of the layer thickness,$\nabla_{\Theta}(\epsilon)$ is the solution of,

$$\frac{1}{2}(10^{20}\epsilon^4 \nabla_{\Theta})^{1/4} = \frac{0.02}{\nabla_{\Theta}} - 1 \tag{4.4.9}$$

$Ra_*(\epsilon)$ is the solution of,

$$\frac{1}{2} Ra_*^{1/4} = 0.02 \frac{10^{20}\epsilon^4}{Ra_*} - 1 \tag{4.4.10}$$

[3]Data provided by Achim Weiss, Max Planck Institute for Astrophysics, Garching, Germany

The flux $f^s(\epsilon)$ has two forms. The first one ($f^s_{\rm corr}$) is the diffusion corrected version for small values of Ra_*, the second one f^s for large values of Ra_*.

$$f^s_{\rm corr}(\epsilon) : \frac{1}{2}(10^{20}\epsilon^4 0.02\frac{1}{f^s})^{1/4} = f_s - 1 \tag{4.4.11}$$

and

$$f^s(\epsilon) : \frac{1}{2}(10^{20}\epsilon^4 0.02\frac{1}{f^s})^{1/4} = f_s \tag{4.4.12}$$

The radiative Prandtl number $\sigma_{\rm rad}$ dominates in these regimes,

$$\sigma_{\rm rad} = \frac{\nu_{\rm rad}}{\kappa_T} = \frac{1}{5}\frac{T\,c_p}{c^2} \approx 10^{-7} \tag{4.4.13}$$

Assuming that the critical Rayleigh number is about $Ra_{crit} \approx 10^4$ leads to the conclusion that semi-convection is efficient as long as

$$Ra_* > 10^{-3} \tag{4.4.14}$$

$$\epsilon > 5 \times 10^{-6} \tag{4.4.15}$$

Below $\epsilon \approx 4 \times 10^{-5}$ however, ($log(f^s) \approx 0$ in figure 4.26) the flow becomes inefficient at transporting heat and the gradient ∇ approaches the radiative gradient $\nabla_{\rm rad}$. Figure 4.27 depicts the parameter space of Ra_*,as function of the semi-convection layer height. The values of Ra_* numerically reachable are of the same order of magnitude as the stellar relevant values. Because of that the performed simulations are also relevant for astrophysical problems.

Conclusion 1

Equipped with the latter estimates it is possible to derive the maximum number of layers in this semi-convective zone, which still guarantees efficient semi-convective mixing. Using $\epsilon = 4 \times 10^{-5}$ ($Ra_* = 10^{-3}$) as reference, a maximal number of $25000/H_P$ layers is needed such that semi-convection is still efficient. If the zone would have more layers, the semi-convective mixing process would not be able to mix matter efficiently. Hence, conductive or radiative mixing processes would dominate. This particular zone (cf. figure 4.25) with height $H = 10^{10}cm$ has consequently at most 12500 layers with an average height of $\delta = 4 \times 10^5$cm. Numerical results can cover layers with an extent in the range of $4\times10^{-4} < \epsilon < 5\times10^{-3}$, which corresponds to heights between $4 \times 10^6{\rm cm} < \delta < 5 \times 10^7{\rm cm}$. These simulations do not cover the stellar parameter space for σ and τ.

Conclusion 2

Assuming a 'stellar' Prandtl number of $\sigma \approx 10^{-7}$ the modified Rayleigh number, at which semi-convection is important, becomes $Ra^* = 10^0 - 10^4$. Since the Nusselt number for theses values of Ra^* is in the range of $1 \leq Nu_T \leq 3$ the convective contri-

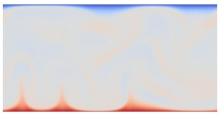

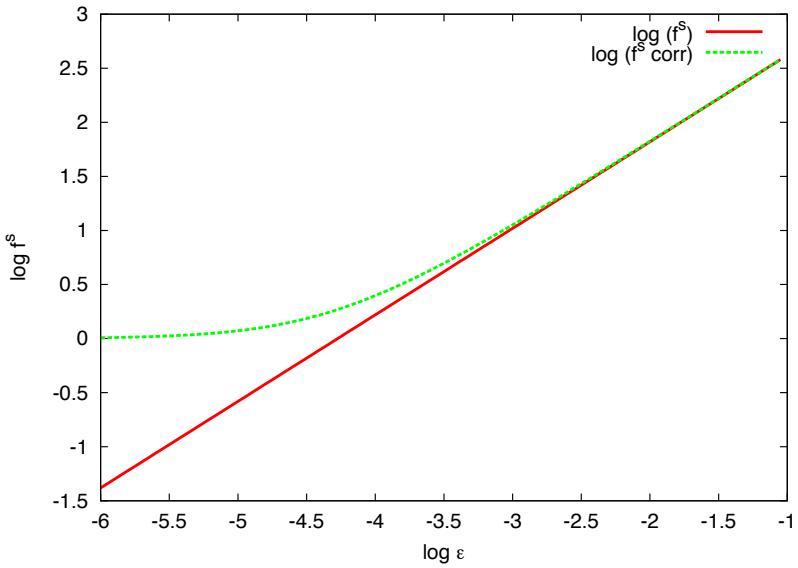

Figure 4.26: Flux as function of ϵ.

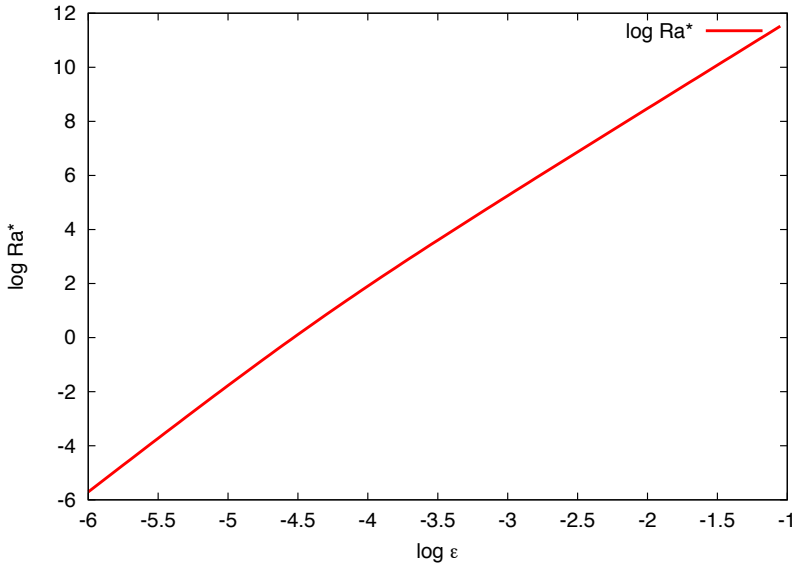

Figure 4.27: Ra_* as function of ϵ.

bution to the mixing process is very low and consequently the layers are temporarily very stable. This assumption is valid as long as the mean flow is zero and no other mixing processes occur.

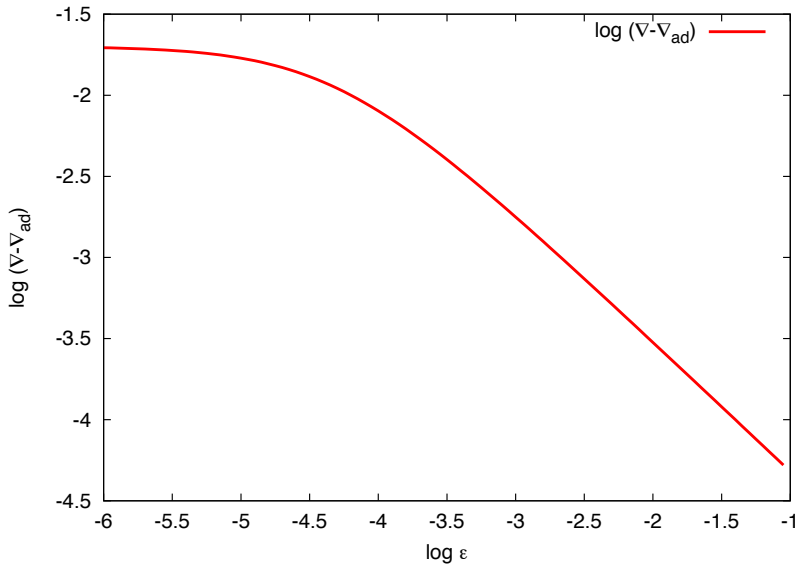

Figure 4.28: $\nabla_\Theta (\hat{=} \nabla - \nabla_{\mathrm{ad}})$ as function of ϵ.

Conclusion 3

The effective diffusion coefficients can now be calculated via (2.5.24) and (2.5.26). We assume a thermal Nusselt number in the order of $Nu_T \approx 300$, which is an upper limit if we take $Ra_* = 10^{12}$. This is only an estimate and can vary. Further more we use the Lewis number $\tau = \kappa_{\mathrm{He}}/\kappa_T \approx 10^{-9}$, the relation (4.2.1) and a realistic value for the thermal diffusion coefficient $\kappa_T \approx 10^8 cm^2/s$.

$$(\kappa_T)_{\mathrm{eff}} = \kappa_T \cdot Nu_T = 10^8 \cdot Nu_T = 3 \times 10^{10} cm^2/s$$

$$(\kappa_{\mathrm{He}})_{\mathrm{eff}} = \kappa_{\mathrm{He}} \cdot Nu_{\mathrm{S}} = \kappa_{\mathrm{He}} Nu_T \tau^{-1/2} = 10^{-1} Nu_T 10^{9/2} \approx 10^7 cm^2/s$$

Since the semiconvective layer has a height of $H = 2 \times 10^{10} cm$ the diffusive timescale can be estimated via,

$$\tau_{\mathrm{He}} = \frac{H^2}{(\kappa_{\mathrm{He}})_{\mathrm{eff}}} = 4 \times 10^{14} s = 10 Myr$$

This is an upper limit and increases rapidly for smaller values of Ra_*. Compared to the life time of a high mass star of our interest which is in the order of $10 Myr$, the semi-convective helium transport is inefficient. In consequence the helium transport due to semi-convective mixing does not influence the stellar evolution much.

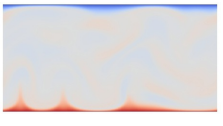

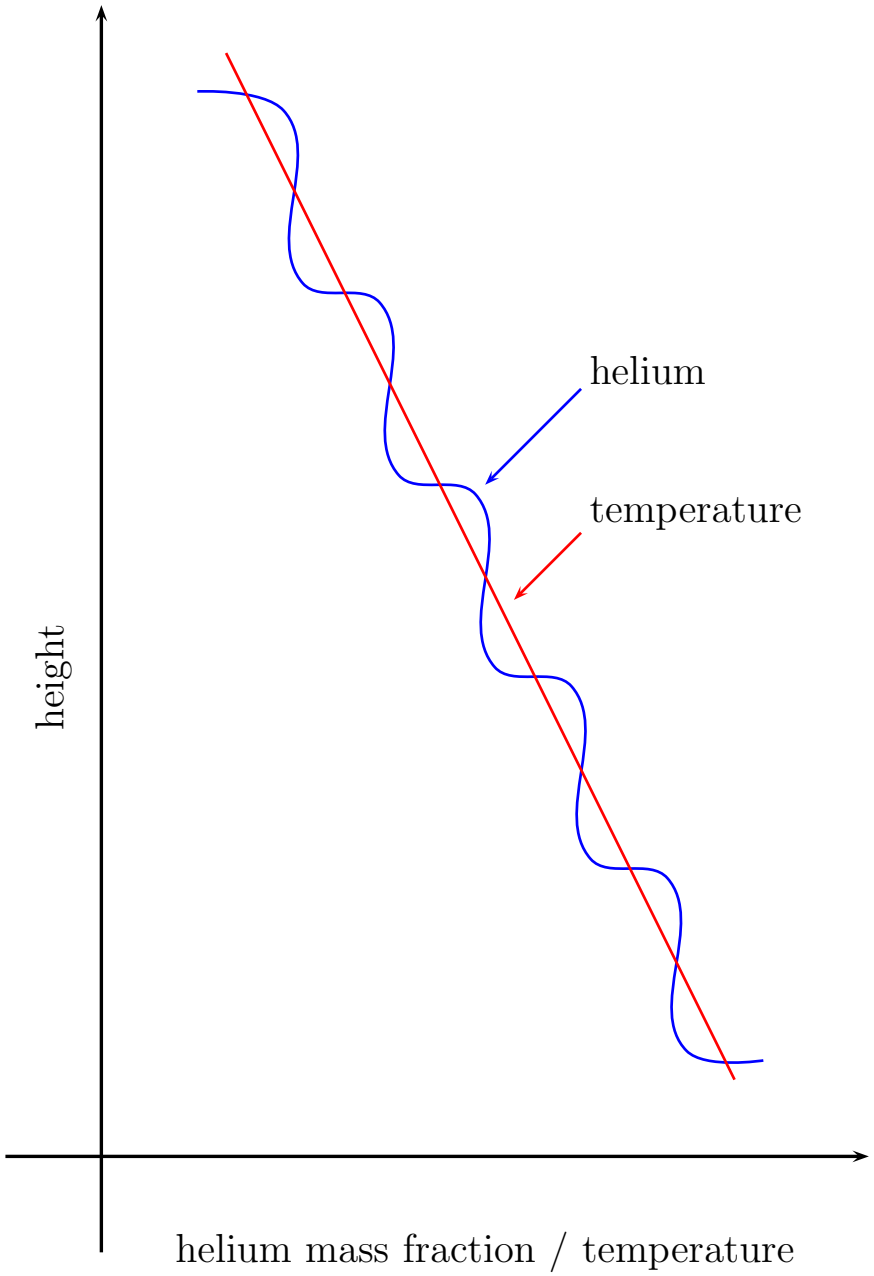

Figure 4.29: New view on semi-convection zones for the low thermal Nusselt number regime. Steep local gradients in the helium mass fraction and nearly linear temperature stratification. This assumption is based on a low thermal Nusselt number ($Nu_T \approx 1$), about 10000 layers and the very high saline Nusselt number ($Nu_S \approx 10^4$).

4.5 Salt-finger simulations

Beside semi-convection there are several other double-diffusive convection instabilities. One of the most important of them is the *salt-finger instability* which can evolve if an unstable salt stratification is stabilised by a temperature gradient. Compare figure 1.4. Similar to the semi-convection instability, the salt-finger regime is split into a stable and an unstable regime, where only the stable salt-fingers are of importance. The gradients have to fulfill the following inequalities,

$$\nabla_\Theta < 0 \tag{4.5.1}$$

$$\nabla_\mu < 0 \tag{4.5.2}$$

$$\nabla_\mu < \nabla_\Theta \tag{4.5.3}$$

Salt-fingers can be observed in oceans, where cold freshwater is layered under warmer salty water eg. in a river mouth. A very nice indoor experiment (cf. figure 4) with warm water and ink was done by M. Cantiello [4]. Numerical experiments have been performed by Thomas Zweigle [priv. comm.], who performed and analysed 2D and 3D simulations. While the stability parameter for semi-convection is defined as the ratio of the saline Rayleigh number to the thermal Rayleigh number, this definition is inverted for salt finger experiments, $R_\rho = Ra_T/Ra_S$. This leads to a comparable parameter for both, semi-convection and salt-fingers. A salt-finger simulation with $R_\rho = 1.11$, $\sigma = 1.0$, $\tau = 0.01$, $Ra_* = 5.0 \times 10^4$ and a resolution of 300×300 has been done. The depicted quantity in the figures 4.30 is salinity, the white contour lines are temperature iso-surfaces. In the figured case the evolution is measured in multiples of the thermal diffusion time scale τ_T. So

4.6 Double layer simulations

A critic could say that single layer simulations are influenced by boundary conditions. While this is true it can be shown nevertheless that multi-layer simulations behave quite similarly to single-layer simulations. Since semi-convective zones tend to develop multi layer structures, numerical simulations have to pass the test of stabilising these separated convective zones. The first extension of a single layer experiment is the double-layer. 'Free' diffusive layers can be observed in triple-layer simulations. They are presented in the next section. It will be shown that two separated layers do not mix by advection as long as the Rayleigh number is small enough and the gradients fulfills 1.3.6. Usually the high thermal diffusion coefficient mixes the layers within the thermal diffusion time scale, which can be observed in the coffee cup too. The following time series (figure 4.31) shows such a stable situation. The parameters represent a water simulation: $\sigma = 6.8$, $\tau = 10^{-2}$, $R_\rho = 1.113$, $Ra_* = 5.8 \times 10^5$,

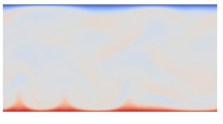

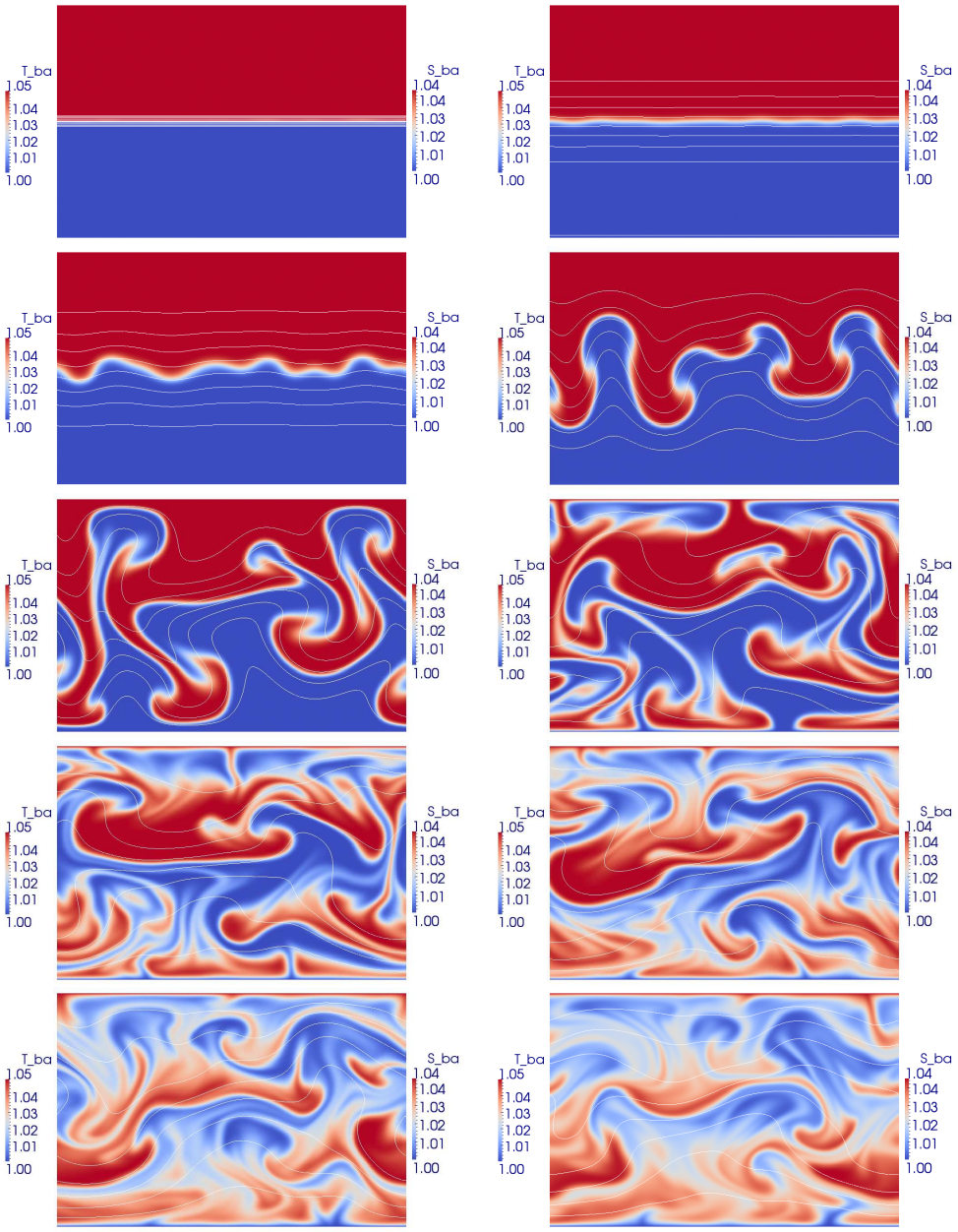

Figure 4.30: Salt-finger simulation: The depicted variables is the salinity. The white lines represent temperature isolines. The so called 'first generation fingers' form between $t = 0$ and $t = 0.08$. From $t = 0.08$ to $t = 0.112$ the fluid gets rapidly mixed by advection. From now on a diffusive regime starts and the 'second generation fingers' begin to form, which are temporarily very stable structures.

$Res = 500 \times 500$. The left fluid column depicts salinity, the right one temperature. The differences in the widths of both plumes goes with the square root of the Lewis number. This explains, why the saline plume is about 10 times smaller than the thermal plume. The figures 4.32-4.33 show the same numerical experiment, but in

Double layer simulation: Temporal evolution
Parameters: $\sigma = 6.8$, $\tau = 10^{-2}$, $R_\rho = 1.113$, $Ra_* = 5.8 \times 10^5$, $Res = 500 \times 500$

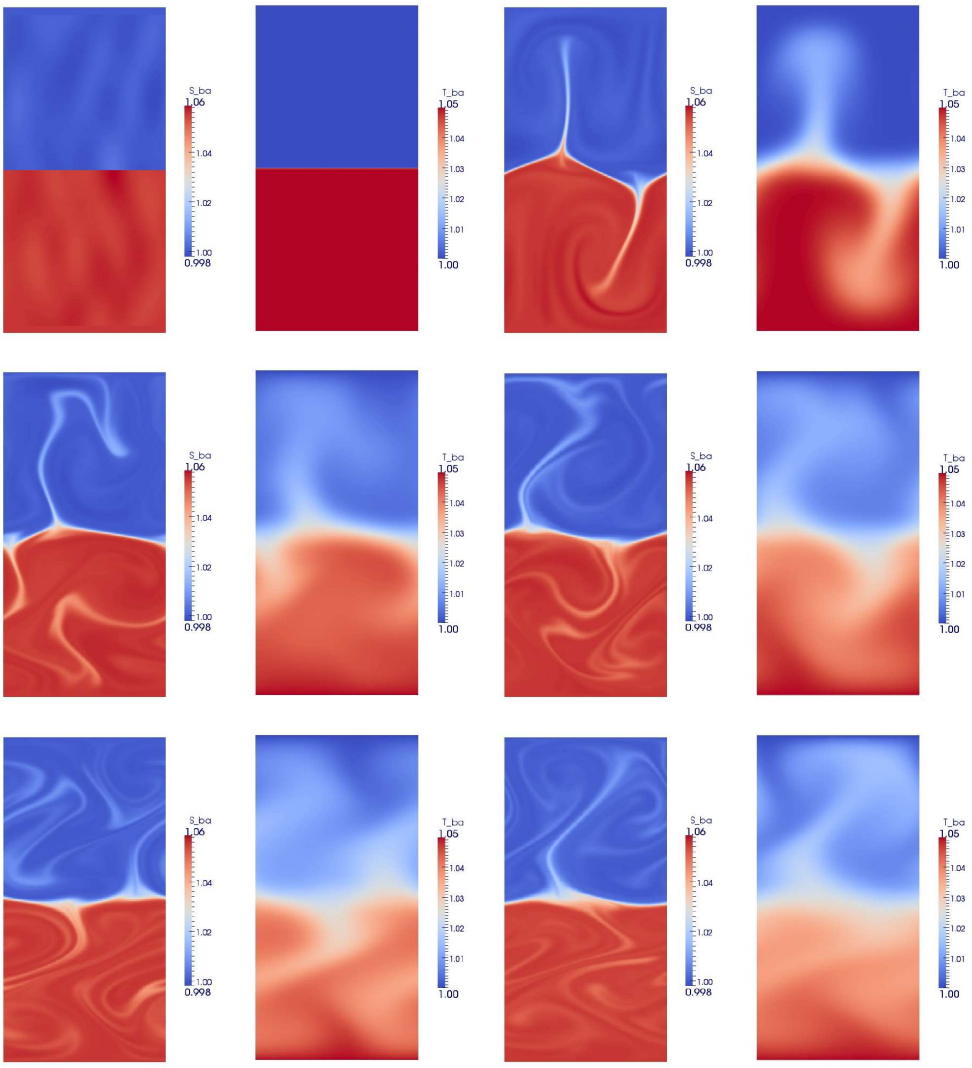

Figure 4.31: Stable double layer simulation from t=0.001 to t=0.4. left: salinity, right: temperature

a lower resolution (200×200). The outcome of different values for τ and R_ρ is presented in salinity and temperature. The simulation time is $t = 0.001$ to $t = 0.08$, where $t = 1 \triangleq 1\tau_T$ (single layer diffusion time scale).

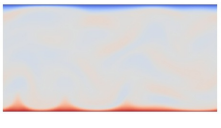

Reference: $\sigma = 6.8$, $\tau = 10^{-2}$, $R_\rho = 1.113$, $Ra_* = 5.8 \times 10^5$, $Res = 200 \times 200$

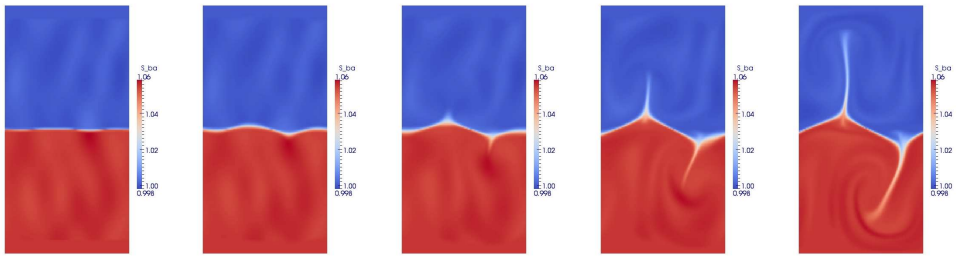

Case 1: $\sigma = 6.8$, $\boldsymbol{\tau = 10^{-1}}$, $R_\rho = 1.113$, $Ra_* = 5.8 \times 10^5$, $Res = 200 \times 200$

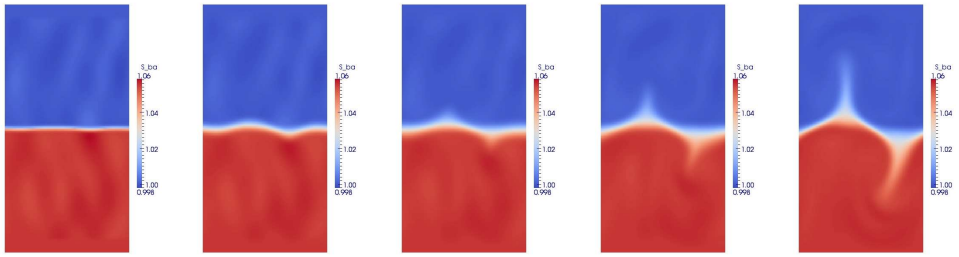

Case 2: $\sigma = 6.8$, $\tau = 10^{-2}$, $\boldsymbol{R_\rho = 0.5}$, $Ra_* = 5.8 \times 10^5$, $Res = 200 \times 200$

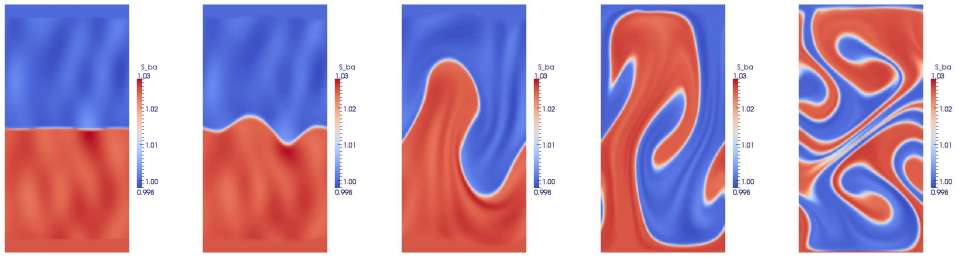

Figure 4.32: Salinity of a double layer experiment for different values of τ and R_ρ. The plumes in case 1 are broadened due to the higher saline diffusion coefficient. Decreasing the stability parameter leads to an unstable, fully convective regime. Time: $t = 0.001$ to $t = 0.08$

4.7 Triple layer simulations

The logical extension of the double-layer experiment is the triple (or multi-layer) simulation. This is the first situation, where the diffusive boundaries are 'free'. Hence the model must pass a test, where the diffusive boundaries are not connected to the numerical domain. A triple layer simulations fulfills the disconnection clause and this is presented here. The computational cost of such a simulation is very high. Typical resolutions are 1000×1000 points, to resolve numerically each layer correctly. Multi-layer simulations are much more susceptible to changes in the parameter space than single layer experiments. But they reproduce the realistic behavior of a 'free' layer. First tests showed that the Rayleigh number has to be chosen carefully. Since Ra_T goes with the fourth power of the height, this fact has to be taken into account. Good results could be achieved with small Rayleigh numbers ($\approx Ra_T = 10^5$ / layer), but due to the third power in height, this value increases rapidly.

Reference: $\sigma = 6.8$, $\tau = 10^{-2}$, $R_\rho = 1.113$, $Ra_* = 5.8 \times 10^5$, $Res = 200 \times 200$

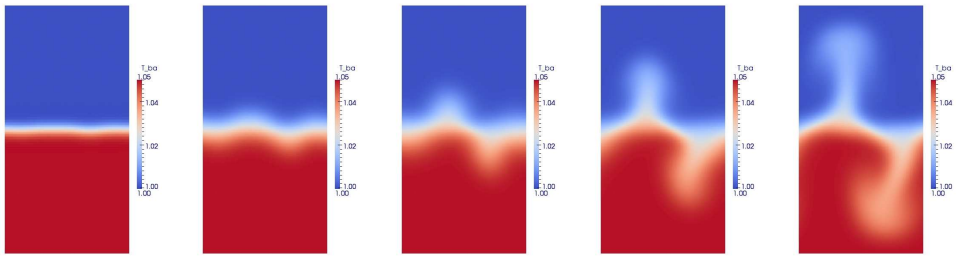

Case 1: $\sigma = 6.8$, $\boldsymbol{\tau = 10^{-1}}$, $R_\rho = 1.113$, $Ra_* = 5.8 \times 10^5$, $Res = 200 \times 200$

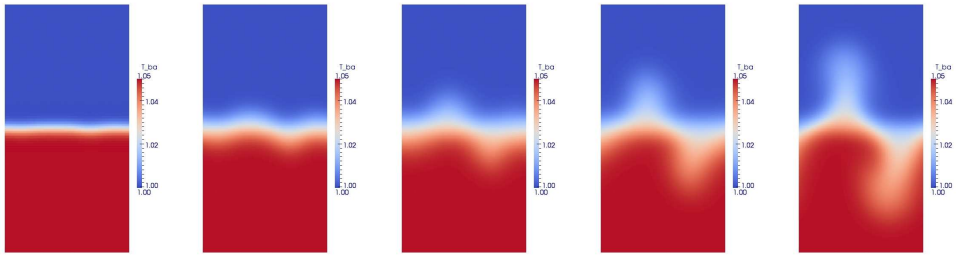

Case 2: $\sigma = 6.8$, $\tau = 10^{-2}$, $\boldsymbol{R_\rho = 0.5}$, $Ra_* = 5.8 \times 10^5$, $Res = 200 \times 200$

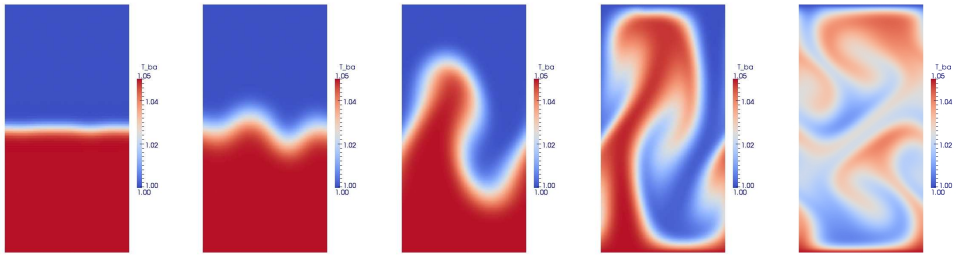

Figure 4.33: Temperature field of a double layer experiment for different values of τ and R_ρ. The plumes in case 1 have the exact same width of the reference solution. They are not affected by the Lewis number. Decreasing the stability parameter leads to an unstable, fully convective regime. Time: $t = 0.001$ to $t = 0.08$

Parameter space for each single layer: $H_{\mathrm{BA}} = 1$, $\sigma = 10^{-1}$, $\tau = 10^{-2}$, $R_\rho = 1.15$, $Ra_T = 6.17 \times 10^4$, $Ra_* = 6.17 \times 10^5$, $Res = 300 \times 600$

Parameter space for the whole stack: $H_{\mathrm{BA}} = 3$, $\sigma = 10^{-1}$, $\tau = 10^{-2}$, $R_\rho = 1.15$, $Ra_T = 5 \times 10^7$, $Ra_* = 5 \times 10^5$, $Res = 900 \times 600$

Since the Rayleigh number for the incompressible case takes the form,

$$Ra = \frac{g \Delta T H_{\mathrm{BA}}^3}{\kappa_T \nu} \tag{4.7.1}$$

the triple layer simulations have new values for $(\Delta T)_{\mathrm{triple}} = 3 \times \Delta T$ and $H_{\mathrm{triple}} = 3 \times H_{\mathrm{BA}}$. Hence, the Rayleigh number for the triple layer simulations is 81 times larger than the comparative single layer experiment.

$$Ra_{\mathrm{triple}} = \frac{g(3 \times \Delta T)(3 \times H_{\mathrm{BA}})^3}{\kappa_T \nu} = 81 \times Ra_{\mathrm{single}} \tag{4.7.2}$$

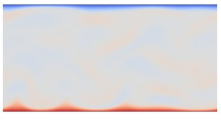

Resolution	CPUs (splitting x:y)	Output time
62^2	1	$<$ 1min
125^2	6 (3:2)	$<$ 2 min
250^2	6 (3:2)	5 min
500^2	6 (3:2)	57 min
1000^2	6 (3:2)	1080 min

Table 4.7: Scaling for of different resolutions for the bubble simulations in Boussinesq approximation.

4.8 Scaling test with interacting bubbles

The interacting bubble experiment is based on two bubbles with different buoyancy behavior. A small high concentration bubble is falling and interacts with a big low concentration and therefore rising bubble. Five experiments have been performed, where the resolution increases by a factor of two in each spatial direction. A scaling test has been done mainly to test the performance of the Poisson solver. The bubbles are not perfect circles at low resolutions, because the numerical approximation fails here. This leads to slightly different solutions. However, the numerical convergence is good to see.

The generic standard parameter set is chosen, which takes the form: $\sigma = 10^{-1}$, $\tau = 10^{-2}$, $Ra_* = 1.6 \times 10^5$, aspect ratio $1:1$

Resolution: 62^2 128^2 250^2 500^2 1000^2

The Schur complement - FISHPACK© solver works satisfactory. Direct solvers like the Gauss elimination method would need[4]

$$\frac{n^3}{3} + n^2 - \frac{n}{3} \tag{4.8.1}$$

operations, where $Ax = b$ and $dim(A) = n \times n$. This is somewhat a worst case scenario. No solver should scale like this. Our method scales (in the 2D case) with

$$\mathcal{O}(n) - \mathcal{O}(n^2). \tag{4.8.2}$$

as estimated based on the log-log plot in figure 4.35.

[4] cf. Meister [32] p43

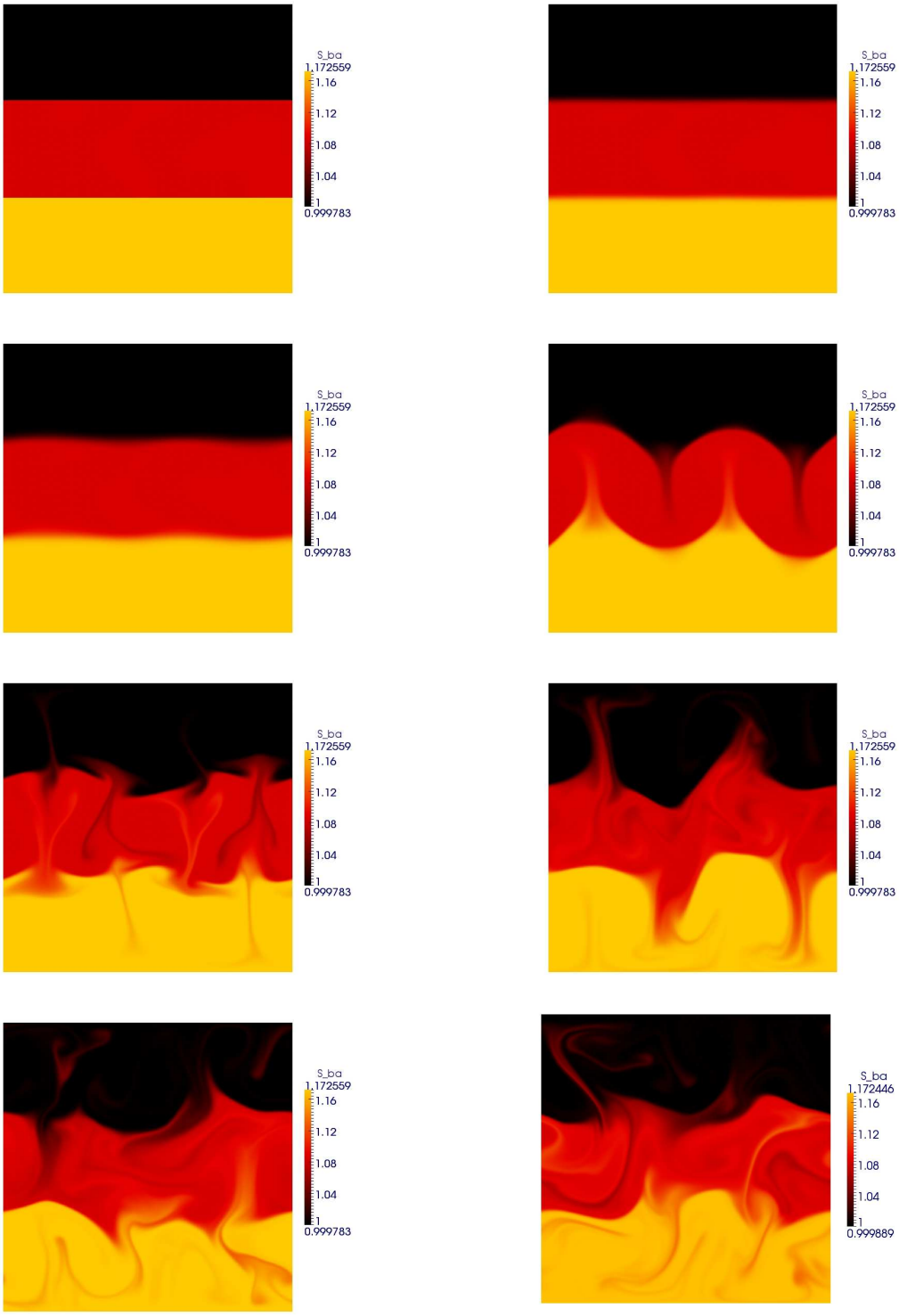

Figure 4.34: Multi layer simulation. Time: $t = 0.001$ to $t = 0.56$

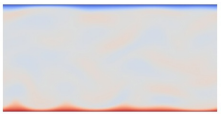

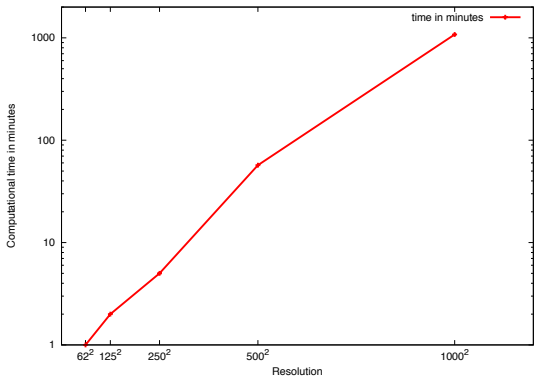

Figure 4.35: Scaling test: Computational time as function of the resolution

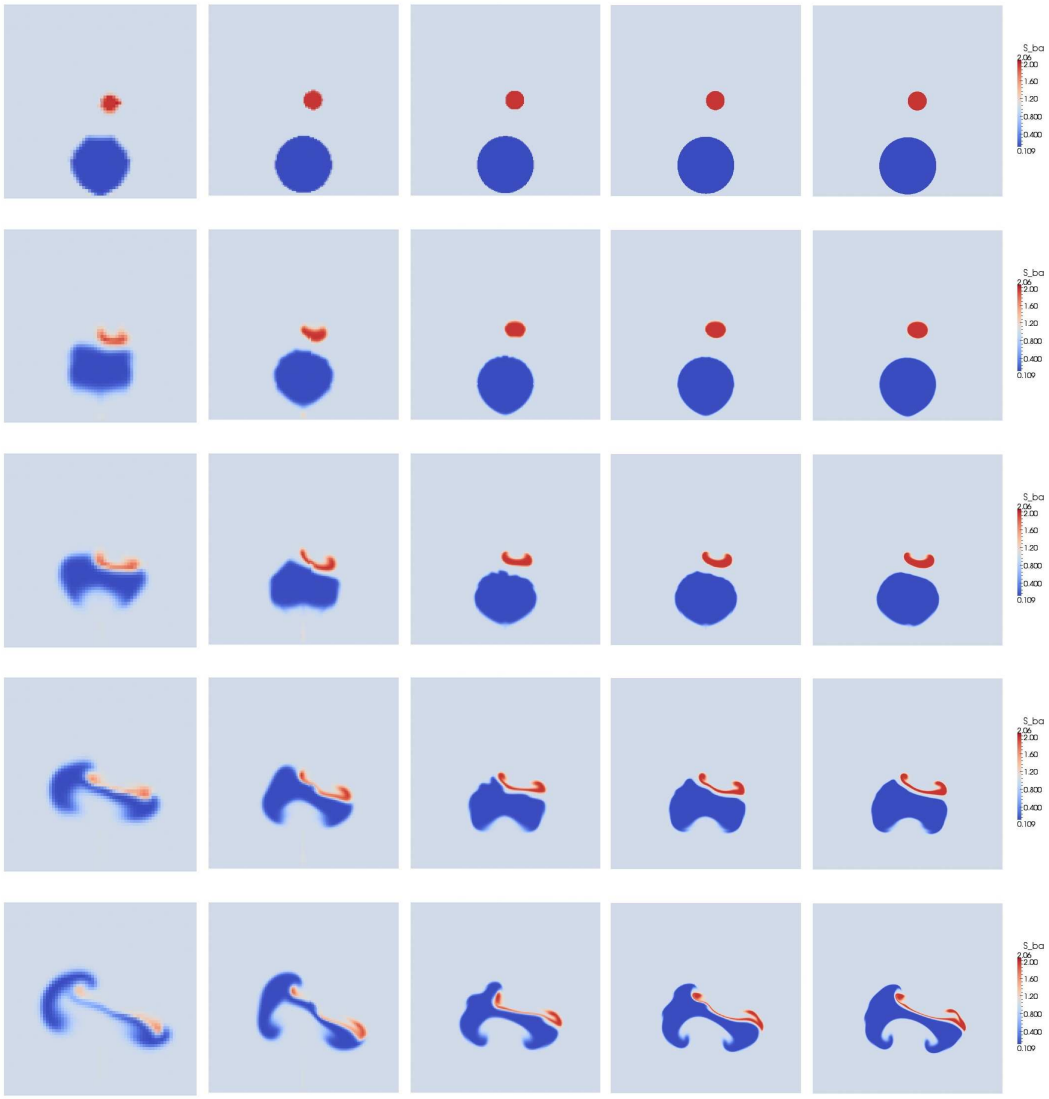

Figure 4.36: Comparison of different resolutions columns for the interacting bubble simulation in Boussinesq approximation. $t = 0$ to $t = 0.02$ in 5 steps

4.9 Previous work

In this section I want to focus on five authors, who have published results based on theoretical work and numerical simulations of double-diffusive convection.

In 1976 Huppert and Moore [23] published the first comprehensive work about double-diffusive convection. All basic relations between the fluxes, Rayleigh numbers, Prandtl and Lewis number were studied. This work is an advanced introduction into the theory of double-diffusive convection and is therefore highly recommended by the presented author.

A pioneer in 2D numerical simulations is W. Merryfield, who published in 1995 the 'Hydrodynamics of Semiconvection' [33]. The numerical treatment of the equations has been done by an anelastic approximation. The parameter space was taken from a 1D model of a $30M_{\odot}$ star that completed on-half of the main sequence evolution. Step-like layering in the helium concentration could not be observed. Unfortunately, no flux information was published which makes comparisons quite difficult. Even double-layer experiments have been performed but the only stable simulation was convectively stable due to the sub-critical Rayleigh number. The single layer simulations could be reproduced in the presented paper in a different setup. The simulations could not be redone with his physical setup, due to a different ansatz in the time integration. These simulations behaved like the 'small box' cases, but increasing the box size or the Rayleigh number lead to similar results. The explicit WENO-solver failed in the parameter space of Merryfield, which leads to the assumption that realistic simulations can only be done with (semi)-implicit solvers. The Mach numbers were too small in our simulations, which covered Merryfield's vertical extent. Here we used the small box approach as comparison, otherwise the pressure scale height would be too high.

In the year 2001 K. Kötter published a thesis with the German title 'Instabilität durch doppel-diffusive Konvektion: Strukturbildung in Experiment und Simulation'[5]. The aim of his work was the comparison of experimental double-diffusive structures and numerical simulations. His results were not be intended to be reproduced with ANTARES, because he focused on salt-finger simulations.

In the same year (2001) J. Biello published his thesis with the title 'Layer formation in semiconvection' (see [3]). Biello's work covers a wide parameter space and produced remarkable simulations. His results could be reproduced.

In 2007 G. Bascoul covered saltfingering and semi-convection in one work with the title 'Double-diffusive convection in stars'[6]. Several high resolution simulations have been performed showing double-diffusive experiments. The Boussinesq equations

[5] see Kötter [25]
[6] see Bascoul[2]

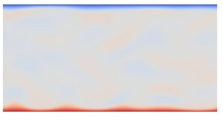

were solved with a 'tailored' pseudo-spectral code. I would like to give a special mention to this work, because G. Bascoul gives a very good overview about double-diffusive convection and their simulation. The interested reader is invited to ask the author for a copy of this thesis, which is unfortunately not available otherwise. The results of G. Bascoul could be reproduced.

4.10 Conclusion and discussion

Double diffusive convection in terms of stable semi-convection was analysed. A wide parameter space in the Prandtl number, Lewis number, a modified Rayleigh number and a stability parameter was covered by numerical simulations in 2D. Existing power laws, which correlate the Rayleigh number and the thermal flux, suggest to be an upper limit as long as the Rayleigh number is big enough. The low Rayleigh number regime needs a correction due to thermal diffusion. It could be shown that even in the near sub-critical regime a modified power law fits perfectly the simulation results. This leads to the assumption that these modified power law can be used to extrapolate into a stellar parameter space. Implicit functions, based on theoretical considerations were derived, which enable to estimate the semi-convective mixing rate in terms of ∇_Θ. These functions are independent from previous stellar evolution models and can be used for arbitrary stars with semi-convective mixing zones.

Semi-convection layers in stars of our interest are temporarily very stable as long as the mean flow is zero. This stability assumption is based on a theoretical estimate and its numerical validations. An upper limit for the thermal Nusselt number $Nu_T < 300$ could be shown. Furthermore, it could be shown that the helium transport due to semi-convective mixing is so inefficient that is does not influence the stellar evolution much, because the mixing time scales are at least in the same order of magnitude as the life time of the star. Hence other mixing processes need to be taken into account.

The base of all these considerations is a parameter study. The numerical experiments are based on a compressible explicit solver and an incompressible semi-implicit solver. The compressible set of equations, which describe a binary mixture, is solved along characteristics with a weighted essentially non-oscillatory scheme in 5th order. This high resolution method ensures shock capturing and hence strong numerical stability. The incompressible equations are solved on a special staggered grid. The combination of the WENO scheme with this staggered grid ensures a numerically very stable behavior. Both numerical solvers are parallelised with MPI© and OpenMP©, which allows calculations on high performance supercomputers.

The comparison between both numerical approaches successful as long as the Mach numbers are high enough, $Ma > 0.01$. Compressible simulations below this limit tend to fail in their validity. Equivalent results could only be reproduced for special

cases. The solver in Boussinesq approximation is much more efficient than any other explicit scheme in this parameter space. Therefore, it is preferred for incompressible low Mach number simulations.

A possible point of criticism lies in the dimension of the simulations. Of course, 3D simulations are more realistic, but due to the enormous computational cost, a parameter study is not feasible yet. However, 3D simulations are planned.

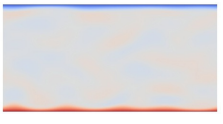

Appendix A

Gradients in the astrophysical context

A.1 Real temperature gradient: ∇

The actual (logarithmic) temperature gradient takes the form,

$$\nabla := \frac{\partial \ln T}{\partial \ln P} = \frac{P}{T}\frac{\partial T}{\partial P} = \frac{P}{T}\frac{\partial T/\partial z}{\partial P/\partial z} \tag{A.1.1}$$

and represents the temperature change in an astrophysical context.

A.2 Adiabatic gradient: ∇_{ad}

The adiabatic temperature gradient is defined as,

$$\nabla_{\mathrm{ad}} = \frac{\Gamma_2 - 1}{\Gamma_2} =: -\left(\frac{d\,ln\,T}{d\,ln\,P}\right)_{\mathrm{ad}} \tag{A.2.1}$$

and represents temperature stratification for a fluid in thermal equilibrium. Here, the values of Γ_2 are set for an monoatomic ideal gas. An ideal gas with low temperature (and neglect-able radiative pressure) has an adiabatic gradient of,

$$\nabla_{\mathrm{ad}} = \frac{5/3 - 1}{5/3} = 0.4 \tag{A.2.2}$$

It is easy to see that the adiabatic lapse rate can be converted into the adiabatic temperature gradient, as long as the fluid is an ideal gas.

$$\left(\frac{\partial T}{\partial z}\right)_{\mathrm{ad}} = \frac{\vec{g}}{cp} \tag{A.2.3}$$

Using the identities,

$$c_P - c_V = \frac{\mathcal{R}}{\mu} \tag{A.2.4}$$

and

$$\frac{c_P}{c_V} = \gamma \tag{A.2.5}$$

the equation becomes,

$$c_P = \frac{\mathcal{R}}{\mu}\left(\frac{\gamma - 1}{\gamma}\right)^{-1} = \frac{\mathcal{R}}{\mu \nabla_{\mathrm{ad}}} \tag{A.2.6}$$

where $\gamma = \Gamma_2 = 5/3$. Extending the latter equation and using the ideal gas law,

$$\left(\frac{\frac{\partial T}{\partial z}}{\frac{\partial P}{\partial z}}\right)_{\mathrm{ad}} = \frac{\frac{\vec{g}}{\mathcal{R}\mu^{-1}\nabla_{\mathrm{ad}}^{-1}}}{\frac{\rho\vec{g}}{1}} = \frac{\mu\nabla_{ad}}{\mathcal{R}\rho} = \frac{T}{P}\nabla_{\mathrm{ad}} \tag{A.2.7}$$

leads to,

$$\left(\frac{\partial ln T}{\partial ln P}\right)_{\mathrm{ad}} = \nabla_{\mathrm{ad}} \tag{A.2.8}$$

The *superadiabatic gradient* is the defined as $\nabla_{\mathrm{sa}}(= \nabla_\Theta) := \nabla - \nabla_{\mathrm{ad}}$. The Schwarzschild criterion for convection takes the form,

$$\nabla_{\mathrm{ad}} < \nabla < \nabla_{\mathrm{rad}} \tag{A.2.9}$$

and predicts if a layer is unstable to convection ($\nabla_{\mathrm{sa}} > 0$) or stable to convection ($\nabla_{\mathrm{sa}} < 0$).

A.3 Mean molecular weight gradient: ∇_μ

The mean molecular weight gradient is defined as follows (see [24]),

$$\nabla_\mu := \frac{\partial \, ln \, \mu}{\partial \, ln \, P} = \frac{P \, \partial \, \mu}{\mu \, \partial \, P} \tag{A.3.1}$$

where $\mu = (2X + \frac{3}{4}Y + \frac{1}{2}Z)^{-1}$ is the mean molecular weight and X, Y, Z are the mass fractions of hydrogen, helium, and other elements.

A.4 Radiative gradient: ∇_{rad}

'The radiative gradient is defined as the thermal gradient which would be necessary to carry the total heat flux (convective flux and radiative flux) by radiation only and

is defined as,'[1]

$$\nabla_{\mathrm{rad}} := \frac{3}{16\pi acG}\frac{\chi LP}{mT^4} \tag{A.4.1}$$

where L is the luminosity, m is the mass, χ is the Rosseland opacity, and G is the gravitational constant.

[1] [29] 5.1.3

Appendix B

Useful derivations

B.1 Derivation of the diffusive boundary layer thickness

In the context of the fluid column height and other quantities, the thermal boundary layer thickness δ_T is an unknown parameter. With the help of the mixing length theory (MLT) a correlation between the Rayleigh number and the diffusion coefficients can be obtained. A balance between advection by the interior flow and the diffusion across the separating interface can be used to estimate the boundary layer thickness. Hence the diffusive boundary layer thickness is different for the temperature and the salinity. We define the thickness of the thermal boundary layer in a semi-convection zone as,

$$\delta_T = \sqrt{\kappa_T \cdot \tau_c} \tag{B.1.1}$$

To calculate δ_T the diffusion coefficient κ_T and the convective time scale τ_c has to be determined. For our purpose we use the MLT, which is commonly used in stellar evolution. The convective cell time scale τ_c has to be

$$\tau_c = \frac{H}{v_c} \tag{B.1.2}$$

where the convective velocity v_c is defined as,

$$v_c^2 = \frac{1}{8} g \delta_{TH} (\nabla - \nabla_e) \frac{H^2}{H_P} \tag{B.1.3}$$

and $\delta_{\mathrm{TH}} := -\frac{\partial ln\rho}{\partial lnT}$. '$\nabla_e$ describes the variation of temperature T in the element during its motion, where the position of the element is measured by the pressure P. In this sense ∇_e and ∇_{ad} are similar.'[1] The modified Rayleigh number Ra_* gives us

[1] [24] p39

the thermal diffusion coefficient κ_T,

$$Ra_* = Ra_T \cdot \sigma = \frac{g}{H_P}(\nabla - \nabla_{\rm ad}) f(\beta) \frac{H^4}{\kappa_T^2} \tag{B.1.4}$$

where $f(\beta)$ is a function due to radiative pressure correction and $\beta = \frac{P_{\rm rad}}{P}$. Hence, using equations (B.1.3) and (B.1.1) the interim boundary layer estimation becomes,

$$\delta_T^4 = \kappa_T^2 \tau_c^2 = (\nabla - \nabla_{\rm ad}) f(\beta) \frac{H^4}{Ra_*} \frac{8}{\delta_{\rm TH}(\nabla - \nabla_e)} \tag{B.1.5}$$

$$\left(\frac{\delta}{H}\right)^4 = f(\beta) \frac{\nabla - \nabla_{\rm ad}}{\nabla - \nabla_{\rm e}} \frac{8}{\delta_{\rm TH}} \frac{1}{Ra_*} \tag{B.1.6}$$

We are now able to estimate the terms,

$$\frac{\delta_T}{H} = \underbrace{\sqrt[4]{f(\beta)}}_{\to 1} \underbrace{\sqrt[4]{\frac{\nabla - \nabla_{\rm ad}}{\nabla - \nabla_{\rm e}}}}_{\to 1} \underbrace{\sqrt[4]{\frac{8}{\delta_{\rm TH}}}}_{\to 1} \sqrt[4]{\frac{1}{Ra_*}} \tag{B.1.7}$$

Finally, thermal boundary layer thickness δ_T becomes,

$$\frac{\delta_T}{H} = \sqrt[4]{\frac{1}{Ra_*}} = Ra_*^{-\frac{1}{4}} \tag{B.1.8}$$

The Helium boundary layer thickness $\delta_{\rm He}$ follows the definition of the Lewis number $\tau = \frac{\kappa_c}{\kappa_T}$. In this case $\kappa_c = \kappa_{\rm He}$. The incompressible (saline) case uses $\kappa_c = \kappa_{\rm S}$

$$\delta_{\rm He} = \sqrt{\kappa_{\rm He} \cdot \tau_c} = \sqrt{\tau}\sqrt{\kappa_T \tau_c} = \sqrt{\tau}\delta_T \tag{B.1.9}$$

The Helium boundary thickness scales with the thermal boundary layer thickness and the square root of the Lewis number.

Example with $\sigma = 1.0$ and $\tau = 10^{-1}$

To perform direct numerical simulations the smallest structures have to be resolved. These structures are the diffusive helium boundaries. If we want to resolve a 5% thick thermal layer (20 points) out of 400 points which is $\frac{\delta_T}{H} = \frac{20}{400}$, a Rayleigh number of $Ra_* = 20^4 = 160000$ has to be chosen. Hence, $\delta_{\rm He} = \sqrt{\tau} \cdot \delta_T \approx \frac{1}{3} \cdot \delta_T \approx 6$ points out of 400. Using a smaller Lewis number leads to a much smaller Helium boundary layer: $\tau = 10^{-2} \rightarrow \delta_{\rm He} = 2$ points out of 400, which is smaller than a numerical stencil, and therefore not resolvable, even with 400 points in each direction. Fortunately, a series of simulations showed that a resolution of 400 vertical points suffices to resolve a boundary layer for a Lewis number of $\tau = 10^{-2}$.

B.2 Damping p-modes

This section follows the thesis of Regner [47].

Initially, simulations of compressible fluid are usually not exactly in vertical pressure balance, which leads to unwanted oscillations. These oscillations could lead to extra mixing and therefore they have to be eliminated. The surplus of energy will go into excitation of so called *p-modes*, which can easily be observed in the vertical momentum or velocity field. These oscillations are typically very stable and do not dissipate or the dissipation takes very long compared to the entire simulation time.

Motivation

Assuming the ODE with some in principle arbitrarily prescribed damping time t,

$$\frac{d\,u_{\mathrm{p-mode}}}{d\,t} = -\frac{u_{\mathrm{p-mode}}}{t_{\mathrm{damping}}} \tag{B.2.1}$$

with the solution,

$$u_{\mathrm{p-mode}} = (u_{\mathrm{p-mode}})_0 e^{-t/t_{\mathrm{damping}}} \tag{B.2.2}$$

where $u_{\mathrm{p-mode}} = \frac{\langle \rho v_{\mathrm{vert}} \rangle}{\langle \rho \rangle}$ is the velocity of the p-mode and $\langle ... \rangle$ is the horizontal average. The solution implies that the velocity is damped exponentially with time t_{damping}.

Efficient damping

The damping term (B.2.1) is now added to the vertical velocity field in following way,

$$\frac{d\,u_{\mathrm{vert}}}{d\,t} = \left(\frac{d\,u_{\mathrm{vert}}}{d\,t}\right)_0 - \frac{u_{\mathrm{p-mode}}}{t_{\mathrm{damping}}} \tag{B.2.3}$$

The damping time t_{damping} can be chosen arbitrarily, but should be short enough that damping is efficient and long enough that the system can adjust to the artificial dissipation. It can be shown that the damping time should be next to the p-mode period, which leads to,

$$t_{\mathrm{damping}} \approx 1.3\,\tau_{\mathrm{p-mode}} \tag{B.2.4}$$

where $\tau_{\mathrm{p-mode}}$ is the period of the p-mode. Typical values for our simulations are $\tau_{\mathrm{p-mode}} = 2-3\,scrt$, where $scrt$ is the sound crossing time through the box. Usually the p-mode disappears if convection sets in. Damping is stopped once the amplitude of the p-mode is 1% of the original one. The p-mode period $\tau_{\mathrm{p-mode}}$ can be determined by analysing the integrated vertical velocity or momentum field. An FFT on this quantity leads to the dominant frequency.

List of symbols

List of greek symbols

All physical quantities underlie the 'cgs' convention, which means that centimeter, gram and second are the metric system of the physical units.

symbol	quantity	explanation
α_S	saline expansion coefficient	ideal gas $\alpha_S = 1/S$
α_T	thermal expansion coefficient	ideal gas $\alpha_T = 1/T$
δ	boundary layer thickness	
ΔT	vertical temperature difference	
η	dynamic viscosity	
ϵ	ratio of height to pressure scale height	
$\Gamma^{(1,2,3)}$	adiabatic exponents	
γ	adiabatic exponent	
κ_T	thermal diffusivity coefficient	
κ_S	saline diffusivity coefficient	
κ	unspecified diffusion coefficient	
∇	real temperature gradient	$\nabla = \frac{\partial lnT}{\partial lnP}$
∇_{ad}	adiabatic temperature gradient	
∇_μ	mean molecular gradient	
∇_Θ	super adiabatic gradient	$\nabla_\Theta \equiv \nabla - \nabla_{\mathrm{ad}}$
∇_{rad}	radiative gradient	
ν_c	thermal conductivity	
ν	kinematic viscosity	
Π	pressure tensor	
π	tensor viscosity	
ρ	density	
τ	Lewis number	$\tau \equiv Le$
τ_{diff}	diffusion time scale	
τ_c	convective cell time scale	
Θ	potential temperature	
σ	Prandtl number	$\sigma \equiv Pr$

List of latin symbols

symbol	quantity	explanation
BA	Boussinesq approximation	
c_i	concentration of species i	
c_P	specific heat capacity (const. P)	
c_V	specific heat capacity (const. V)	
e	internal energy	
e_{tot}	total energy	
F_{rad}	radiative flux	
F_{conv}	convective flux	
F_{chem}	chemical flux	
F_{cond}	conductive flux	
F_{ad}	adiabatic heat flux	
F_{tot}	total (heat) flux	
g_z	gravitational acceleration	
H	height of the box	
H_P	pressure scale height	
H_{BA}	height of box in BA	
Le	Lewis number	
Ma	Mach number	
Nu_S	saline Nusselt number	
Nu_T	thermal Nusselt number	
$\vec{p}$	momentum vector	
P	pressure	
Pr	Prandtl number	
Q_{nuc}	nuclear energy generation rate	
Ra_*	modified Rayleigh number	$Ra_* = \sigma Ra_T$
Ra_T	thermal Rayleigh number	
Ra_S	saline Rayleigh number	
$(Ra_S)_{\mathrm{crit}}$	critical saline Rayleigh number	
Ra_{crit}	critical thermal Rayleigh number	
R_ρ	stability parameter	
S	salinity	
Sc	Schmidt number	
T	temperature	
$\vec{u}$	velocity vector	
X	hydrogen mass fraction	
Y	helium mass fraction	
Z	metallicity mass fraction	

other symbols

symbol	quantity	explanation
$\mathbb{1}$	unity tensor	

Superscripts and subscripts

Superscripts and subscripts are explained with the dummy variable ξ

symbol	explanation
ξ_a	top boundary
ξ_b	lower boundary
ξ^{BA}	in Boussinesq approximation
ξ^{s}	in stellar or compressible approximation
$\bar{\xi}$	mean value
ξ'	variation
ξ_0	reference value
ξ^*	intermediate value

Acknowledgement

In erster Linie möchte ich mich bei meinem Betreuer Univ. Prof. Dr. Herbert Muthsam bedanken. Die zahlreichen Diskussionen haben mich immer motiviert und gezeigt, dass die Lösung eines Problems manchmal direkt vor einem liegen kann, auch wenn man 'den Wald vor lauter Bäumen nicht mehr sieht'. Bei PD Dr. Friedrich Kupka möchte ich mich für seine unermessliche Geduld bedanken. Die intensive Zusammenarbeit mit ihm war massgeblich für den Erfolg dieser Arbeit. PD Dr. Friedrich Kupka initialisierte das DFG Projekt 'Doppel-diffusive Konvektion im Stern und Ozean' (DFG Projekte: KU 1954-3/1 und KU 1954-3/2 innerhalb von SPP 1276/1 und SPP 1276/2 im Zuge des MetStroem Projektes), dem ich 3 Jahre als wissenschaftlicher Mitarbeiter am Max-Planck Institut für Astrophysik (MPA) zugewiesen war. Am MPA betreute mich Univ. Prof. Dr. Hendrik Spruit. Ihm habe ich zu verdanken, dass der Brückenschlag zwischen Mathematik und Physik geklappt hat.

Liebe Stephanie - Du hast alle Phasen der 'Diss' mitgemacht und immer an mich geglaubt, wenn ich es nicht mehr getan habe. Ich danke Dir dafür aus ganzem Herzen.

Obwohl ich meine Familie nur selten sehen konnte, war sie immer an meiner Seite und unterstützte mich wo sie nur konnte.

Die lustigsten Diskussionen hatte ich auf jeden Fall in der 'Coffee-corner' mit den Freuden am MPA, die ich sicher vermissen werde. Ohne gute Freunde können 3 Jahre ganz schön lange werden. Meine Kollegen aus der ACORE Gruppe waren immer mit Rat und Tat zur Stelle, wenn man schnell was gebraucht hat. Dieser Einsatz ist spitze und deshalb gebührt Euch doppelt Dank.

Neben den menschlichen Begleitern möchte ich meinen Dank an zwei weitere 'Individuen' richten. VIP und P5 - Ihr habt mir zwar viele Nerven gekostet, aber ohne euch müsste ich heute noch auf die Ergebnisse warten.

Diese Doktorarbeit widme ich jemandem, der mir die ganzen 3 Jahre immer sehr nahe stand und mit dem ich öfters harte Kämpfe ausgetragen habe - meinem *porcus canis interior* oder zu deutsch *innerer Schweinehund*.

Curriculum Vitae

Name: Florian Zaussinger

Birthdate: 24. March 1978

Citizenship: Austria

July 1997 - March 1998: military service

June 1998: school examination

October 1998 - September 2000: Vienna technical university, Austria: Technical mathematics in computational science

October 2000 - September 2004: Freelancer

October 2004 - January 2007: University of Vienna, Austria: Master Mathematics

January 2007: Master thesis: 'A simple model for *listeria monocytogenes*'

September 2007 - August 2010: Max-Planck-Institute for Astrophysics, Garching, Germany: PhD mathematics

Bibliography

[1] John Adams. Efficient fortran subprograms for the solution of separable elliptic partial differential equations, 2010. http://www.cisl.ucar.edu/css/software/fishpack/.

[2] Guillaume Bascoul. *Double-diffusive convection in stars*. PhD thesis, University of Cambridge, 2007.

[3] Joseph Biello. *Layer formation in semiconvection*. PhD thesis, University of Chicago, 2001.

[4] Matteo Cantiello. Private homepage, 2010. http://www.matteocantiello.com.

[5] V. M. Canuto. Semiconvection and Overshooting: Schwarzschild and Ledoux Criteria Revisited. *The Astrophysical Journal*, 534:L113–L115, May 2000.

[6] B. Castaing, G. Gunaratne, L. Kadanoff, A. Libchaber, and F. Heslot. Scaling of hard thermal turbulence in Rayleigh-Benard convection. *Journal of Fluid Mechanics*, 204:1–30, July 1989.

[7] A.J. Chorin and J.E. Marsden. *A Mathematical Introduction to Fluid Mechanics*. Springer, 1979.

[8] A.J. Chorin and J.E. Marsden. *A mathematical introduction to fluid mechanics*. Springer New York, 2000.

[9] Martin Dietzel. Munich cumulonimbus cloud, September 11 2007. http://epod.usra.edu/blog/2007/09/munich-cumulonimbus-cloud.html.

[10] D. Drikakis and W. Rider. *High-Resolution Methods for incompressible and Low-Speed Flows*. Springer, 2005.

[11] C.P. Dullemond. Lecture on: Numerical fluid dynamics:, 2010. http://www.mpia-hd.mpg.de/ dullemon/lectures/fluiddynamics/index.html.

[12] R. Fedkiw, B. Merriman, and S. Osher. High Accuracy Numerical Methods for Thermally Perfect Gas Flows with Chemistry. *Journal of Computational Physics*, 132:175–190, April 1997.

[13] R. Fedkiw, B. Merriman, and S. Osher. Efficient characteritic projection in upwinding difference schemes of hyperbolic systems. *Journal of Computational Physics*, 141:22–36, 1998.

[14] T. Fliessbach. *Statistische Physik*. Elsevier, 2007.

[15] Hannes Grimm-Strele. Numerical solution of the generalised poisson equation on parallel computers. Master's thesis, Universität Wien, 2010.

[16] S.R. De Groot and P. Mazur. *Grundlagen der thermodynamik irreversibler Prozesse*. B.I. Hochschultaschenbuecher, 1969.

[17] S. A. Grossman, R. Narayan, and D. Arnett. A theory of nonlocal mixing-length convection. I - The moment formalism. *ApJ*, 407:284–315, April 1993.

[18] S. A. Grossman and R. E. Taam. Double-Diffusive Mixing-Length Theory, Semiconvection and Massive Star Evolution. *Monthly Notices of the Royal Astronomical Society*, 283:1165–1178, December 1996.

[19] H. Guillard and C. Viozat. On the behaviour of upwind schemes in the low Mach number limit. *computers & fluids*, 28:63–86, November 1997.

[20] F. H. Harlow and J. E. Welch. Numerical Calculation of Time-Dependent Viscous Incompressible Flow of Fluid with Free Surface. *Physics of Fluids*, 8:2182–2189, December 1965.

[21] A. Harten. On High-Order Accurate Interpolation for Non-Oscillatory Shock Capturing Schemes. *Institute for Mathematics and Its Applications*, 2:71–+, 1986.

[22] W. Hillebrandt and F. Kupka. *Lecture notes in physics 756, Interdisciplinary aspects of turbulance*. Springer, 2009.

[23] H. E. Huppert and D. R. Moore. Nonlinear double-diffusive convection. *Journal of Fluid Mechanics*, 78:821–854, 1976.

[24] R. Kippenhahn and A. Weigert. *Stellar structure and evolution*. A&A Library, 1990.

[25] Karsten Koetter. *Instabilitaet durch doppel-diffusive Konvektion: Strukturbildung in Experiment und Simulation*. PhD thesis, Universitaet Dortmund, 2001.

[26] N. Kwatra, J. Su, J. T. Grétarsson, and R. Fedkiw. A method for avoiding the acoustic time step restriction in compressible flow. *Journal of Computational Physics*, 228:4146–4161, June 2009.

[27] L.D. Landau and E.M. Lifshitz. *Fluid Mechanics (Course of theoretical physics Volume 6 second edition)*. Elsevier, 1987.

[28] M. Lesieur. *Turbulence in fluids*. Kluwer Academic Publisher, 1995.

[29] A. Maeder. *Physics, Formation and Evolution of Rotating Stars*. Springer, 2009.

[30] B. Magnell. Salt Fingers Observed in the Mediterranean Outflow Region (34degN, 11degW) Using a Towed Sensor. *Journal of Physical Oceanography*, 6:511–523, July 1976.

[31] J. M. Massaguer and J.-P. Zahn. Cellular convection in a stratified atmosphere. *A&A*, 87:315–327, July 1980.

[32] A. Meister. *Numerik linearer Gleichungssysteme*. Vieweg, 2008.

[33] W. J. Merryfield. Hydrodynamics of semiconvection. *ApJ*, 444:318–337, May 1995.

[34] M.I.T. M.i.t general circulation model, 2010. `http://mitgcm.org/`.

[35] H. J. Muthsam, W. Gob, F. Kupka, and W. Liebich. Interacting convection zones. *New Astronomy*, 4:405–417, August 1999.

[36] H. J. Muthsam, F. Kupka, B. Löw-Baselli, C. Obertscheider, M. Langer, and P. Lenz. ANTARES - A Numerical Tool for Astrophysical RESearch with applications to solar granulation. *New Astronomy*, 15:460–475, July 2010.

[37] J. J. Niemela, L. Skrbek, K. R. Sreenivasan, and R. J. Donnelly. High Rayleigh Number Turbulent Convection. *APS Meeting Abstracts*, pages J2+, November 2000.

[38] Christof Obertschieder. *Modelling of solar granulation - Implementation and comparison of numerical schemes*. PhD thesis, Universität Wien, 2007.

[39] H. Pearlmann. Excitability in High-Lewis Number Premixed Gas Combustion. *Combustion and flame*, 109:382–398, May 1997.

[40] L. Quartapelle. *Numerical solution of the incompressible Navier-Stokes equations*. Birkhauser Verlag, 1993.

[41] M. Schmid, M. Busbridge, and A. Wüst. Double-diffusive convection in Lake Kivu. *Limnol. Oceanogr.*, 55:225–238, 2010.

[42] C.-W. Shu and S. Osher. Efficient Implementation of Essentially Non-oscillatory Shock-Capturing Schemes. *Journal of Computational Physics*, 77:439–+, August 1988.

[43] E A. Spiegel and G. Veronis. On the Boussinesq approximation for a compressible fluid. *Astrophysical Journal*, 131:442–447, 1959.

[44] H. C. Spruit. The rate of mixing in semiconvective zones. *A&A*, 253:131–138, January 1992.

[45] Matthias Tomczak. An introduction to physical oceanography, April 2002. `www.es.flinders.edu.au/ mattom/IntroOc/notes/figures/images/convection1.gif`.

[46] E. F. Toro. *Riemann Solvers and numerical Methods for Fluid Dynamics*. Springer, 1999.

[47] Regner Trampedach. Convection in stellar atmospheres. Master's thesis, University of Aarhus, 1997.

[48] J. S. Turner. Double-Diffusive Phenomena. *Annual Review of Fluid Mechanics*, 6:37–54, 1974.

[49] A. Weiss, W. Hillebrandt, H.-C. Thomas, and H. Ritter. *Cox & Giulis principles of stellar structure (Extended second edition)*. CSP, 2004.

[50] WolframResearch. Wolframalpha, 2010. `http://www.wolframalpha.com/`.

Erklärung:

'Ich habe mich bemüht, sämtliche Inhaber der Bildrechte ausfindig zu machen und ihre Zustimmung zur Verwendung der Bilder in dieser Arbeit eingeholt. Sollte dennoch eine Urheberrechtsverletzung bekannt werden, ersuche ich um Meldung bei mir.'

Eine hochaufgelöste (farbige) PDF Version dieser Arbeit ist auf Anfrage beim Autor zu bekommen. Hierzu verweise ich auf folgende Emailadresse: office@zaussinger.com

A high resolution (colored) PDF version of this thesis can be obtained from the author. Feel invited to write an email to office@zaussinger.com